Hydrostatic pressure studies of semiconductor heterostructures and Schottky diodes

Othaman, Zulkafli Bin

Award date:
1995

Awarding institution:
University of Bath

Hydrostatic Pressure Studies of Semiconductor Heterostructures and Schottky Diodes

Submitted by Zulkafli Bin Othaman
for the degree of PhD
of the University of Bath
1995

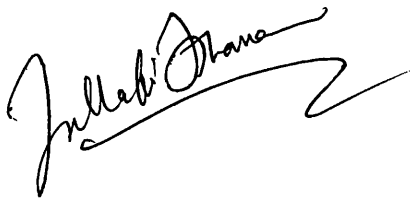

ProQuest LLC
789 East Eisenhower Parkway
P.O. Box 1346
Ann Arbor, MI 48106-1346

Abstract

Investigations of the role of various transport channels have been carried out for single barrier GaAs/AlAs and double barrier AlAs/GaAs/AlAs structures. Current-voltage measurements have been performed in both forward and reverse biases at pressures up to 11 kbar. Measurements at room and liquid nitrogen temperatures were carried out at various pressures while measurements at temperatures between 8 K and 77 K were performed at ambient pressure in a closed cycle cryostat. Variations in amplitude and position of current maxima and minima as well as regions of negative differential resistance with applied pressures help determine the dominant tunnelling channels. In the single barrier structure an observed increase in current with hydrostatic pressure can be attributed to tunnelling involving the X-point minima. The voltage at the peak shifts linearly downwards in voltage with applied pressure. A comparison with self-consistent theoretical calculations indicates that the peak arises due to quasi-resonances between Γ-point confined 2D subbands in the accumulation layer and unoccupied longitudinal X-point confined subbands in the barrier. In the double barrier structure asymmetrical doping of the electrodes helps us identify the origin of resonances in terms of the X-point conduction-band minima. X-X and Γ–X resonances have been observed at high pressure. At ambient pressure and temperature the X-minima appear to play an important role.

An investigation of surface state pinning at metal/semiconductor interfaces has been based on the low temperature I-V characteristics of Schottky diodes. Pd/n^+-GaAs Schottky diodes were exposed to a hydrogen plasma at temperatures between 20 to 200 °C. Current-voltage measurements have been performed at temperatures down to 8 K in a closed cycle cryostat, while measurements under hydrostatic pressures up to 11 kbar were performed in a liquid pressure cell at 77 K

and room temperature. The Schottky barrier height and mean impurity concentration of the samples were then obtained by comparison between experimental data and a self-consistent theoretical model. The Schottky barrier height has been observed to increase from 0.44 eV for unpassivated samples to 0.46 eV for sample hydrogenated at 100 °C. This was accompanied by a general decrease in mean impurity concentration. Possible interpretations are discussed.

Acknowledgement

I would like to thank my supervisor Dr. S.J.Bending for giving me the opportunity to undertake the work described in this thesis, and for being an unfailing source of advice and enthusiasm. He taught me a lot in the art of semiconductor research, especially in the realm of quantum electronic devices. Working with him to setup the cleanroom was a great experience. Without his guidance quantum electronic would be alien to me.

I would also like to thank Prof. G.A. Saunders for his guidance during the initial years I was in Bath, especially in the preparation of high pressure experiments and measurements. His lectures in the classroom, and occasionally in the lab, made me open my eyes in many areas of understanding solid state physics.

Special acknowledgement also goes to Dr.R.T. Syme of Cavendish Laboratory, Cambridge University for supplying the single barrier GaAs/AlAs structures and its self-consistent theoretical calculation. On the other side of the channel my special thanks go to Prof. K. Von Klitzing and his colleagues at the Max-Planck Institut for providing the double barrier structures.

The help of many people in our level 5 laboratory made this work successful and I would like to thank them all: Mr. R.J. (Bob) Draper who taught me the art of using the lathe and milling machines always assisted me in the workshop and whenever necessary; Wendy Lambson who was responsible for supplying the chemicals in the cleanroom and keeping it clean; not forgetting Eddie Lambson who helped set up some of the pressure equipment; and finally the other members in the quantum electronic group - Dr. S. Stoddart, Dr. M. Dellow, the cheerful Virginia Lam, the noisy Geoff Nash, and Ibrahim Mutlu.

My special gratitude is reserved for my wife Shakila Abdul Aziz and my son Muhammed Hazli Zulkafli for their patience and encouragement. My study at the Bath University has also been jointly sponsored by the Public Service Department of Malaysia and the Universiti Teknologi Malaysia.

Contents

Figure Captions

Chapter 2

Chapter 3

Chapter 4

Chapter 5

Chapter 6

Chapter 7

Chapter 8

Chapter 9

Appendix A

Tables

Chapter 3

Chapter 5

Chapter 8

Chapter 9

CHAPTER 1

Introduction

1.1 Motivation

It is well known that silicon (group IV element) is the most widely used semiconductor material for the fabrication of electronic devices, especially in microelectronics eg. large scale integration (LSI) and very large scale integration (VLSI). This is largely due to the existence of an established problem free fabrication technology. Besides microelectronics silicon is also widely used in fabrication of the solar cells, power switching devices and sensors. Silicon is, however, in many respects inferior to GaAs being optically indirect and having a lower electron mobility (Barraclough (1987)). Scientists have described GaAs as the device of the future with increasing technological importance in electronics and optoelectronics. Historically it was first manufactured by Goldschmidt in the 1920s (Blakemore (1987)). Its microfabrication, however, needs a much more advanced technology which was not in existence at that time - thus its development for electronics has been relatively slow.

The technologies of crystal growth, epitaxy, and device processing have now all progressed to a point at which opportunities for GaAs utilisation in integrated circuits (ICs) and in optoelectronics (Blakemore (1987)) have expanded dramatically. Single-barrier GaAs/$Al_xGa_{1-x}As$ and double-barrier GaAs/ $Al_xGa_{1-x}As$/GaAs resonant-tunnelling structures are some examples that benefit from improvements in the quality of material grown by processes such as Molecular Beam Epitaxy (MBE) and Metal Organic Chemical Vapour Deposition (MOCVD).

Resonant tunnelling diodes are finding very important applications in high speed and high frequency systems which will be critical in certain niche applications eg. remote sensing and short range radar. Brown (1989) reported room temprature operation of a resonant tunnelling device which was capable of producing ~0.2 μw at 420 GHz. However, there is still room for improvement for these devices. Better understanding of the considerable role of electron and hole transport in the operation of this kind of structure can lead to further improvements in future devices. The role played by different conduction-band minima in the tunnel process through potential barriers in semiconductor heterostructures is one example. It had been hoped that double barrier resonant tunnelling structures (DBRTS) with AlAs barriers would be significantly better than those with alloy barriers. This is because it was thought that the larger Γ–Γ barrier would improve confinement and lead to a lower non-resonant current component. Thus a higher peak-to-valley current ratio (PVR) might be expected in the I-V characteristic. However, this has not been realised experimentally. There are many factors that can degrade the PVR including thermionic emission, LO phonon emission, and interface roughness.

For a heterostructure in the GaAs/$Al_xGa_{1-x}As$ system, the height of the potential barriers formed by layers of $Al_xGa_{1-x}As$ depend on the aluminium mole fraction (x). The barrier material has a direct band gap for $x < 0.4$ and is indirect when $x > 0.4$. In a direct material, the barrier defined by the Γ minimum at the centre of the Brillouin zone dominates the tunnel process, while in indirect $Al_xGa_{1-x}As$ many experiments indicate that the X-point conduction-band minima near the zone boundary play a major role. A Γ electron from GaAs can tunnel at the Γ, L or X minima depending on (i) which one of them forms the lowest potential barrier, (ii) which has the smallest effective mass, and (iii) whether momentum parallel to the interfaces is conserved. For an AlAs barrier, where Γ(AlAs)-Γ(GaAs) ≅ 1 eV, X(AlAs)-Γ(GaAs) ≅ 0.16 eV, m^*_Γ(AlAs) ≅ $0.1m_o$ and m^*_{Xl}(AlAs) ≅ $1.1m_o$ (Mendez *et al.* (1988)), a simple calculation of the WKB exponent of the tunnelling probability shows it to be comparable for the Γ–Γ–Γ and Γ-X_l-Γ transport channels. There is, however, a third possibility, namely Γ-X_t-Γ with $m_{Xt} \cong 0.2m_o$; which, however, requires a large parallel momentum scattering event sideways towards the Brillouin zone boundary. Such scattering could occur due to interface roughness, ionised donor scattering, phonons or (in AlGaAs) random alloy scattering, but little is known about the relative magnitude of these processes in real diodes. In addition, at high temperatures, the dependence of current density on the effective mass may be unimportant if thermally activated current over the lowest barrier dominates. For AlAs barriers the thermally activated current is almost certain to be dominated by the X-minima.

Attempts to understand this behaviour have been the subject of a number of studies (see Austing *et al.* (1993-95) and Mendez *et al.* (1986-1990)) for example). In this thesis high pressure measurements have been made on single barrier GaAs/AlAs and double barrier AlAl/GaAs/AlAs structures. The X(AlAs)-Γ(GaAs)

conduction band offset decreases by about -12 meV $kbar^{-1}$ while the Γ(AlAs)-Γ(GaAs) discontinuity remains virtually unchanged upon application of pressure (Mendez *et al.* (1988)). The application of high pressure then reduces the X-point minima in the AlAs barrier layers such that quasi-bound states in this layer are available for resonant transmission. Our single barrier structure has a very long undoped region at the emitter which creates a 2D accumulation layer at the emitter/barrier interface under forward bias. Therefore it is possible for electrons to tunnel between this accumulation layer and quasi-bound states in the barrier layer; especially at higher pressures. A comparison with self-consistent calculations helps to verify this. The double barrier structure studied is also asymmetrically doped and under forward bias a 2D accumulation layer is again formed. Resonant tunnelling can then occur between subbands in the accumulation layer and those in the quantum well. The intrinsic asymmetry of the structure aids in the identification of the origins of resonances in terms of the X-point conduction-band minima. An important advantage of applying high pressure is that we do not need to prepare various samples with different Al contents in the barrier layer. In this manner all extrinsic parameters such as interface quality, impurities, and doping profile, remain unchanged while the band structure can be tuned continuously. In our AlAs barrier structures random alloy scattering which can influence the tunnelling current is also avoided.

Another significant recent development in the area of electronic devices has been the progressive miniaturisation of devices; in particular nanostructures. For devices with nanometer dimensions it is important to have very good interfaces which relies on our understanding of crystal growth and surface morphology. Schottky barriers for example are crucial to the operation of metal-semiconductor field-effect transistors (MESFETs), which constitute the heart of GaAs IC

technology. These have been widely studied in the past fifty years yet the nature and origin of the interfacial states at the metal-semiconductor junction remains an open questions (Wang *et al.* (1995)).

Investigations of the interface properties of metal-semiconductor contacts have been widely undertaken for GaAs (Pearton *et al.* (1982), Sharda *et al.* (1991)). The surface pinning effect locks the Schottky barrier height in GaAs to about 0.8 eV for *n*-type GaAs and 0.6 eV for *p*-type GaAs independent of the choice of metal (Costa *et al.* (1991)). Experimentally, the detailed atomic structure at the interface has not yet been sufficiently established, particularly with respect to the presence and nature of defects at the interface. Cross-sectional transmission electron micrographs reveal a deviation from the lattice stoichiometry near the interface (Weber *et al.* (1986)) and cathodoluminescence studies find midgap states near the interface (Chang *et al.* (1991)). A number of groups have correlated the experimentally observed Fermi level pinning position with the energy level of point defects as indirect evidence that defects dominate Fermi level pinning. In particular, the common pinning position for a wide range of metals on III-V compounds has been attributed to the anion antisite. Using the same data, another group has correlated the observed pinning positions with the work function difference between the anion and the host semiconductor to conclude that anion-rich metallic clusters dominate Fermi level pinning (Freeouf (1981)). However, both the point defects and the anion clusters hypothesised to be at the interface have, to date, escaped direct experimental observation.

There are many theories that attribute this pinning effect to a high density of surface states in the gap of the semiconductor. These theories include the unified defect model, the defect-induced gap state theory (DIGS), and metal-induced gap

states (MIGS) (see Mönch (1990)). Another theoretical model due to Tejedor (1985) explains the universal pinning position in terms of the existence of a neutral point in a semiconductor. Strong screening leads in this case to a narrow range of pinning energies. One serious difficulty with this model is that there is no adequate justification for this hypothesis; indeed, detailed electronic structure calculations do not support it (Schilfgaarde *et al.* (1994)).

Experimentally it is widely accepted that dangling bonds which exist on semiconductor surfaces can be passivated by atomic hydrogen (Pearton *et al.* (1987)). Investigations of the effect of hydrogen on the surface states of *n*-GaAs have been performed by (Sharda *et al.* (1991), Pacagnella *et al.* (1989), and *p*-GaAs by Pan *et al.* (1987), Ashok *et al.* (1990). However, in their works exposure to atomic hydrogen took place before metal deposition. This can lead to contamination at the interface. In our work hydrogenation is performed after Pd deposition. This is possible because of the high transparency of Pd to hydrogen atoms (Dembovsky (1984)).

The introduction of atomic hydrogen into semiconductors has many beneficial effects. In amorphous silicon, hydrogenation passivates dangling bonds and strongly influences the electrical and optical properties of the material (Pankove *et al.* (1980)). Hydrogenation of the surface states of *p-n* junctions in crystalline silicon reduces reverse-bias leakage currents (Pankove *et al.* (1978)). Excellent high-frequency characteristic have been observed when the *n*-GaAs for MOS capacitors is treated with a H_2, N_2, and O_2 plasma (Callegari *et al.* (1989)) due to the reduction of the GaAs surface state density. Most of the experimental studies of atomic hydrogen passivation in GaAs have concentrated on *n*-type GaAs, due to its dominant role in MESFET technology.

1.2 Overview of Thesis

This thesis is divided into three different blocks of experimental work i.e. a) experimental preparation of the liquid pressure cell, calibration of pressure gauge and details of the I-V measurement electronics, b) investigation of transport in single and double barrier structures, and c) metal-semiconductor interfaces (theory and experiment). The theory of tunnelling for single barrier and double barrier structures and the concept of resonant tunnelling is presented in Chapter 2. All of the semiconductor structures used in our experiments are based on GaAs/AlAs layers and Chapter 3 discusses the physics of GaAs heterostructures including their basic properties and electron transport through them. The effect of hydrostatic pressure upon GaAs/AlAs structures is also briefly discussed.

It is also important to explain the theory and principle behind the pressure cell which was used to pressurise our samples. This is presented in Chapter 4 along with the manganin pressure gauge calibration. Chapter 5 describes the experimental set-up for I-V and dI/dV measurements, including the electronics and instrumentation. Details of the single barrier and double barrier structures are also included here. Experimental results on single barrier and double barrier structures are presented in Chapter 6 and 7 respectively.

Chapters 8 and 9 are devoted to metal-semiconductor contacts. The theory of metal-semiconductor contacts (with and without surface states) is explained. This is followed by a theoretical description of the current transport mechanism and hydrogen passivation models. Chapter 9 presents our experimental results on Schottky diodes including the effects of hydrogen passivation and hydrostatic pressure.

CHAPTER 2

Tunnelling Theory

2.1 Basic Concepts of Tunnelling

Since the invention of the first p-n tunnel diode by Esaki in 1957 devices based on the tunnelling of electrons or holes through energy barriers have been actively proposed and developed. The advent of new growth techniques such as molecular beam epitaxy (MBE) or metal-organic chemical vapour deposition (MOCVD) further enhanced this development. The GaAs/$Al_xGa_{1-x}As$ system is one example that is actively being investigated.

The devices studied here are mainly based on the behaviour of electrons tunnelling through energy barriers in GaAs/AlAs systems (single and double barrier) and Pd Schottky barriers on n^+-GaAs. The tunnelling phenomena in these three systems can be generalized as tunnelling of electrons in heterostructures. The theory presented here will be based on the theory of Metal-Insulator-Metal (MIM) tunnelling due to Duke (1969) and Kane (1968). A complete review of tunnelling

theory has been given by Kane (1968), Duke (1969), and by Roy (1977). As mentioned by Duke (1969) tunnelling at junctions and interfaces is predominantly a one-electron process, therefore this theory will also be based on the one electron model moving freely among the static ion-core potentials.

Many of the features of tunnelling phenomena in solids are of a one-dimensional nature and if the electric field parallel to the interface is zero we can reduce the tunnelling theory here to a one-dimensional problem perpendicular to the interfaces. A simple one-dimensional single barrier system with barrier height V_0 and barrier width w can be depicted as in Fig.2.1. In this case an electron of effective mass m* and energy E tunnels through in the x-direction. We assume a perfect interface and exclude the possibility of random alloy or phonon scattering into other directions. Therefore momentum is conserved in the yz-plane perpendicular to the tunnelling direction i.e. k_y and k_z are constants of motion. This problem can be solved using the time-independent Schrödinger equation :-

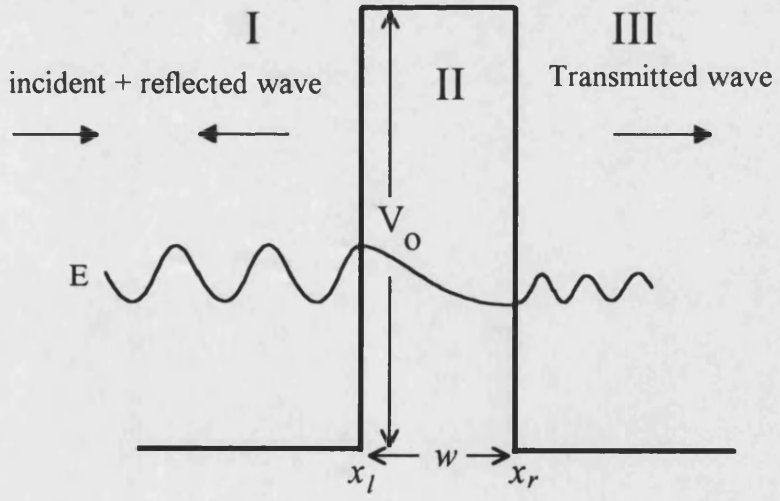

Figure 2.1 : Tunnelling through a single potential barrier

$$\left(-\frac{\hbar^2}{2m^*}\frac{d^2}{dx^2}+V_0\right)\psi(x)=E\,\psi(x) \qquad x_l<x<x_r \qquad (2.1)$$

$$\left(-\frac{\hbar^2}{2m^*}\frac{d^2}{dx^2}\right)\psi(x)=E\,\psi(x) \qquad x<x_l,\ x>x_r \qquad (2.2)$$

where V_0 is a constant electrostatic potential energy in the barrier. The general solution in the three regions are of the form,

In region I :

$$\psi_1(x)=Ae^{ik_1x}+Be^{-ik_1x} \qquad -\infty<x<x_l \qquad (2.3)$$

In the barrier region :

$$\psi_2(x)=Ce^{\kappa_2x}+De^{-\kappa_2x} \qquad -x_l\le x\le x_r \qquad (2.4)$$

and in region III

$$\psi_3(x)=Fe^{ik_3x} \qquad -x_r\le x<\infty \qquad (2.5)$$

where

$$\frac{\hbar^2k_1^2}{2m^*}=E$$

$$\frac{\hbar^2\kappa_2^2}{2m^*}=V_0-E$$

$$\frac{\hbar^2k_3^2}{2m^*}=E$$

and the wavefunctions $\psi_1(x)$and $\psi_3(x)$ are plane waves. However, in the barrier when $E-V_0<0$ the wavefunction $\psi_2(x)$ is a superposition of exponentially decaying and growing solutions characteristic of barrier penetration problems. A more elaborate solution can be found in most quantum mechanics text book (see Liboff (1980) and Cassels (1982) for example).

2.1.1 Transmission Coefficient

From the solution of the above equations the incident current density is given by

$$j_1 = \frac{\hbar k_1}{m^*}|A|^2 \qquad (2.6)$$

and the transmitted current density is

$$j_3 = \frac{\hbar k_3}{m^*}|F|^2 \qquad (2.7)$$

where k_1 and k_3 are the wave vectors of the incident and transmitted waves and A and F are their amplitudes. The transmission coefficient is defined as the ratio of transmitted current density to the incident current density i.e. $D = j_3/j_1$ (see Liboff (1980) for example). Matching boundaries conditions for continuity of ψ and $\frac{1}{m^*}\frac{d\psi}{dx}$ at the interfaces :-

$$D = \frac{j_3}{j_1} = \frac{16k_1k_3\kappa_2^2}{(k_1^2+\kappa_2^2)(k_3^2+\kappa_2^2)}\exp(-2\kappa_2 w) \qquad (2.8)$$

In Eq. (2.8) above the last term $\exp(-2\kappa_2 w)$ dominates the expression. The equation shows that the barrier transmission is symmetric i.e. the transmission coefficient for electrons is equal either from left to right or from right to left. The transmitted current goes continuously to zero if either k_1 or k_3 goes to zero.

The above procedure is easily solved for a barrier with a constant barrier height or when there is no bias applied between the two electrodes. In the presence of an external bias V, the barrier becomes first trapezoidal, and then triangular if $V > V_0$ when one has Fowler-Nordheim tunnelling (Fig. 2.2(a) - (d)). For these kinds of barriers or other barriers of arbitrary shape (defined by $V(x)$) the quantum mechanical solutions would be complicated. In this case the Wentzel-Kramer-

Brillouin (WKB) semiclassical approximation can be used to find the transmission coefficient. This approximation is only applicable in the situation where the slope of the potential energy is gentle enough. The barrier is normally divided into a number of rectangular barriers of infinitesimal widths w_1, w_2,.....,w_n, and of constant κ_1, κ_2,.....,κ_n, respectively. The net transmission coefficient through all barriers is then given by

$$D \sim \exp(-2\int_0^w \kappa(x)\,dx) \tag{2.9}$$

where

$$\kappa(x) = \left(\frac{2m^*}{\hbar^2}\{V(x) - E\}\right)^{1/2} \tag{2.10}$$

This WKB approximation is normally used in the tunnelling current expression for Metal-Insulator-Metal junctions where the large conduction band discontinuity between the metal and insulator forms the basis of a potential step. The method can also be used in semiconductor heterostructures where the potential barrier is formed by the conduction band offset of different semiconductor materials. For example the AlAs layer can form a potential barrier in a GaAs/AlAs/GaAs structure due to the fact that Γ(AlAs) > Γ(GaAs). The WKB approximation is also used by Kotel'nikov *et al.* (1985) in self-consistent calculations used later to describe tunnelling through a Schottky barrier.

Apart from the WKB approximation there are other methods that can be used to find the transmission coefficient. Kane (1968) and Price (1989) used a transfer-matrix method to describe the transmission coefficient through a single and double barrier device. A complete derivation of the transmission coefficient in single and double barrier tunnelling diodes has been presented by Toombs and Sheard (1989) using the WKB approximation, transfer-matrices and the Bardeen

transfer Hamiltonian. The use of the transfer-matrix method is extended to superlattice structures by Tsu and Esaki (1973) and Brennan *et al.* (1988).

2.2 Tunnelling Current in Heterojunctions

Tunnelling through potential barriers such as GaAs/AlAs/GaAs, Metal-Insulator-Metal (MIM), Metal-Insulator-Semiconductor (MIS), and Metal-Semiconductor junctions can be classified as tunnelling through heterojunctions according to Duke (1969). Figure 2.2(a) shows an example of two conductors separated by a potential barrier. The probability that an electron state of energy E and temperature T in the electrodes is occupied is given by Fermi-Dirac statistics i.e. $f(E) = \{1 + \exp[(E-\mu)/kT]\}^{-1}$. Therefore with reference to Fig. 2.2(a) the occupation probability in the right and left electrodes is given by

$$f_R(E_R) = \frac{1}{\left(1+\exp\left(\frac{E_R - E_{FR}}{kT}\right)\right)} \tag{2.11}$$

$$f_L(E_L) = \frac{1}{\left(1+\exp\left(\frac{E_L - E_{FL}}{kT}\right)\right)} \tag{2.12}$$

respectively. From the Fermi golden rule one can show that the current density from right to left is

$$j_{RL} = -e\int \frac{d^3k_R}{(2\pi)^3} 2\, v_{xR} f_R(E_R)[1-f_L(E_R+eV)]D_{RL}(E_R) \tag{2.13}$$

The integral runs over all k_{yR} and k_{zR} but only over $k_{xR}(v_{xR}) < 0$, the $f_R(E_R)$ factor is the probability that the initial state is occupied and the $(1 - f_L)$ factor is the probability that the final state is unoccupied. $2(d^3k_R)/(2\pi)^3$ is the density of states on the right hand side with the factor of 2 arising due to spin degeneracy. As

before $D_{RL}(E_R)$ is the transmission coefficient from right to left. Similarly the current density from left to right is then given by

$$j_{LR} = -e\int \frac{d^3k_L}{(2\pi)^3} 2v_{xL} f_L(E_R + eV)[1 - f_R(E_R)]D_{LR}(E_R) \qquad (2.14)$$

and therefore the total current is the difference of the two taking into account the direction.

$$j_{net} = j_{RL} - j_{LR} \qquad (2.15)$$

This only leads to a simple result if we relate D_{RL} to D_{LR} and $v_{xL}d^3k_L$ to $v_{xR}d^3k_R$. To do this we need to make two assumptions :-

a) Invoking the effective mass model, the effect of the periodic ionic potential in the electrodes is adequately described by using an effective mass for the electron in the dispersion relation :-

$$E(k) = \frac{\hbar^2 k^2}{2m^*} \qquad (2.16)$$

Free electron wave functions are used to solve the problem, but the boundary conditions are actually imposed on approximate eigenfunctions and not the exact eigenfunctions of the junction potential.

b) Using the Average Potential Barrier Model, the exact potential of the barrier is often not known, but is approximated by taking the local average, which varies rather slowly across the barrier due to the macroscopic electric fields arising from the applied bias and the difference in work functions of the electrodes.

For the transition to three dimensions two conservations laws are used:-

1. If the barrier is a perfect infinite plane then the component of k parallel to the interface must be conserved :-

$$k_{||,L} = k_{||,R} = k_{||,barrier} \tag{2.17}$$

2. In the absence of inelastic processes the total energy must also be conserved :-

$$E_L = E_R = E \tag{2.18}$$

As discussed above the barrier transparency is symmetric such that $D_{RL} = D_{LR}$ and only a function of v_{xL} and v_{xR} where

$$v_{xL} = \frac{1}{\hbar}\frac{\partial E(k_L)}{\partial k_{xL}} \tag{2.19}$$

As a consequence D depends only on a notional x component of the energy (E_x) such that

$$D_{LR}(E) = D_{LR}(E_x) = D_{RL}(E_x) \tag{2.20}$$

From the effective mass approximation the total energy can be separated into two notional components namely energy parallel to the plane and perpendicular to it. Note that this assumes an isotropic effective mass.

$$E = \frac{\hbar^2}{2m^*}\{k_x^2 + k_y^2 + k_z^2\} = E_x + E_{||} \tag{2.21}$$

$$V_x = \frac{1}{\hbar}\frac{\partial E(k)}{\partial k_x} = \frac{\hbar k_x}{m^*} \tag{2.22}$$

From the effective mass dispersion relation we deduce that

$$d^2k_{||L} = d^2k_{||R} = d^2k_{||} \tag{2.23}$$

$$dE_L = dE_R \tag{2.24}$$

$$v_{xL}.dk_{xL} = \frac{dE_L}{\hbar} \tag{2.25}$$

Therefore the net current is given by

$$j = \frac{2e}{\hbar(2\pi)^3}\int dE\{f_R(E) - f_L(E+eV)\}d^2k_{\|}D_{APB}(E,k_{\|}) \tag{2.26}$$

making the identities

$$d^2k_{\|} = \frac{2\pi m^*}{\hbar^2}dE_{\|} \tag{2.27}$$

$$D(E,k_{\|}) = D(E - \frac{\hbar^2k_{\|}^2}{2m^*}) = D(E_x) \tag{2.28}$$

$$j = \frac{2m^*e}{\hbar^3(2\pi)^2}\int dE_x\, dE_{\|}\, D(E_x)\{f_R(E_x+E_{\|}) - f_L(E_x+E_{\|}+eV)\} \tag{2.29}$$

$$= \int S(E_x)D_{APB}(E_x)dE_x \tag{2.30}$$

where

$$S(E_x) = \frac{m^*e}{2\pi^2\hbar^3}\int\{f_R(E_x+E_{\|}) - f_L(E_x+E_{\|}+eV)\}dE_{\|} \tag{2.31(a)}$$

$$= \frac{m^*ekT}{2\pi^2\hbar^3}\ln\left(\frac{1+\exp[(E_F - E_x)/kT]}{1+\exp[(E_F - E_x - eV)/kT]}\right) \tag{2.31(b)}$$

is called the supply function. D_{APB} is given by the semiclassical WKB approximation as explained before.

$$D_{APB}(E_x) = \exp\left(-2\int_{x_1(E_x)}^{x_2(E_x)} \kappa_x(x, E_x)\, dx\right) \tag{2.32}$$

where

$$\kappa_x(x, E_x) = \left(\frac{2m^*}{\hbar^2}\{V(x) - E\}\right)^{1/2} \tag{2.33}$$

The current can be calculated for any form of $V(x)$ at any temperature provided that $D(E_x)$ can be calculated for all values of E_x.

2.3 Single Barrier Tunnelling Diodes

An abrupt discontinuity in the conduction band edges of different types of semiconductor materials is the principle behind the construction of a single or double barrier tunnel diode. Unlike Esaki's *p-n* tunnel diode, the barrier in this tunnel diode is formed due to the conduction band offset between the semiconductor materials of the barrier, emitter and the collector. For example a material A with a conduction band edge higher than the conduction band edge of material B will form a barrier if embedded between two layers of material B (Figure 2.2(a)). The band gap of material A is usually greater than the band gap of material B.

2.3.1 Transmission Coefficient for a Single Barrier

Let us consider a symmetrical junction where the electrodes have identical material parameters (i.e. the same semicondutor material and doping density). An undoped barrier layer is sandwiched between two heavily *n*-doped electrodes whose conduction band edge is at a lower energy than the barrier material. At zero bias (V = 0) the Fermi level in the left and right electrodes are in equilibrium. The

number of electrons tunnelling from left to right is the same as that from right to the left and therefore no net current flows. When the lefthand electrode ('emitter') is biased negatively with respect to the righthand electrode ('collector') the Fermi level of the collector falls by an amount of eV. This brings empty states of the collector to the same level as full states of the emitter. There is a net electron tunnel current from the emitter to the empty states of the collector.

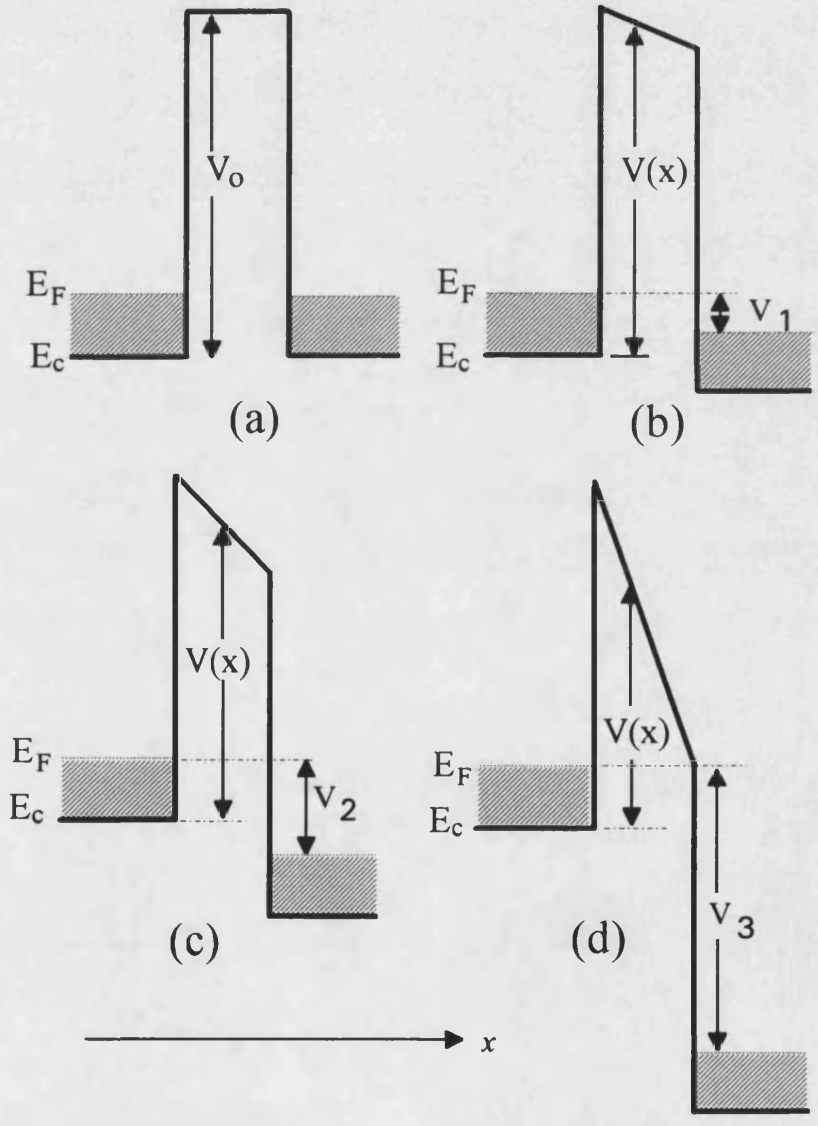

Figure 2.2 : Single barrier tunnelling at different applied bias.

However, due to the applied bias the barrier potential is no longer rectangular and the transmission coefficient ($D(E_x)$) is very sensitive to the actual shape of the barrier (Bonnefoi (1987)). The WKB approximation is used by Duke (1968,1969) and Mendez (1987) to describe the transmission coefficient. As the bias voltage,V is increased the barrier height at the emitter side is a constant V_0. At a bias V less than the barrier height V_0 the barrier is trapezoidal (Fig. 2.2(b) - (c)) and the transmission coefficient is given by (Mendez (1987))

$$D(E_x) \sim \exp\left(-\frac{4}{3}\frac{w}{eV}\left(\frac{2m^*}{\hbar^2}\right)^{1/2}\left((V_0 - V - E)^{3/2} - (V_0 - E)^{3/2}\right)\right) \quad (2.34)$$

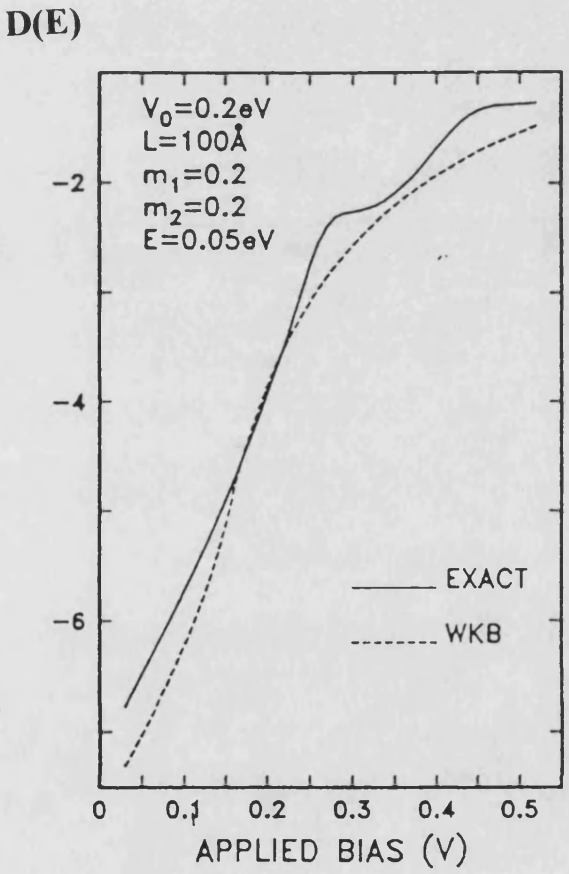

Figure 2.3 : The transmission coefficient of an electron of mass $0.2m_o$ and energy 0.05 eV through a barrier of 0.2eV high and width 100Å. (After Mendez (1987)).

When the applied bias V is greater than V_0 the barrier is reduced to a triangular shape and for this situation of Fowler-Nordheim tunnelling the transmission coefficient is given by

$$D(E_x) \sim \exp\left(-\frac{4}{3}\frac{w}{eV}\left(\frac{2m^*}{\hbar^2}\right)^{1/2}\left((V_0 - E)^{3/2}\right)\right) \qquad (2.35)$$

In all cases the total energy E and the momentum parallel to the interfaces are conserved. We see that in both Eqs. (2.34) and (2.35) the transmission coefficient is also a strong function of barrier width w. Figure 2.3 shows a typical transmission coefficient for a single barrier tunnel diode.

2.3.2 Current Density for a Single Barrier Structure

The tunnelling current at zero temperature can be divided into two bias regions. For the low-bias region where $eV \leq E_F$ the Fermi level of the collector falls between the Fermi level and conduction band edge of the emitter (Fig. 2.2(b)). The range of $E_{||}$ is restricted for tunnelling into unoccupied states. Mendez (1988) and Toombs *et al.* (1989) used the equation for current density which is given by Duke(1969) i.e.

$$J = \frac{em^*}{2\pi^2\hbar^3}\left(eV\int_0^{E_F-eV} D(E_x)\,dE_x + \int_{E_F-eV}^{E_F}(E_F - E_x)D(E_x)\,dE_x\right) \qquad (2.36)$$

In the high bias region when $eV \geq E_F$ (Fig. 2.2(c)) the Fermi energy of the collector falls below the conduction band edge of the emitter. Electrons in all occupied states of the emitter may tunnel into unoccupied states of the collector

where the range of $E_{||}$ for the tunnel current is from 0 to E_F - E_x . The current density is given by :-

$$J = \frac{em^*}{2\pi^2\hbar^3}\int_0^{E_F}(E_F - E_x)\,D(E_x)dE_x \qquad (2.37)$$

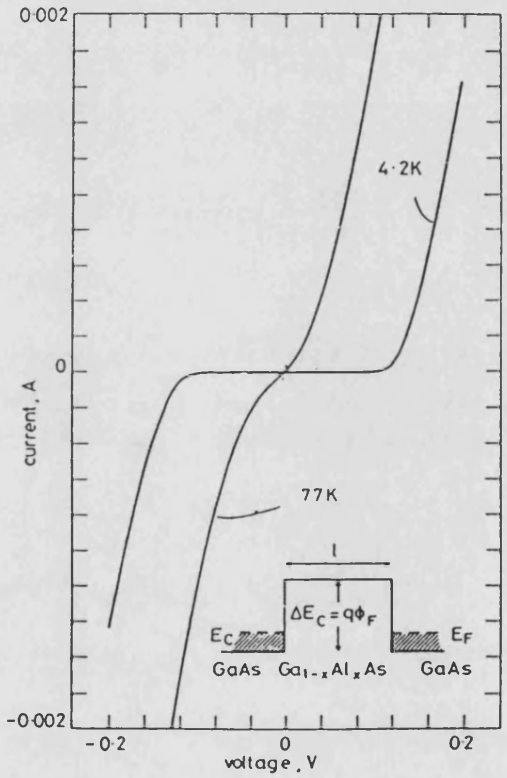

Figure 2.4: Current-voltage characteristics of a single barrier structure with barrier height 86.3meV and barrier width 300Å measured at 4.2 K and 77 K. (After Guéret *et al* (1985)).

Figure 2.4 shows typical current-voltage characteristics for a single barrier tunnel diode at temperatures 77 K and 4 K. At low bias and temperature 4 K when eV << E_F the transmission coefficient in the Eq. (2.36) above is approximately

constant and the current is approximately ohmic (Duke(1969)). At these voltages the Fermi level of the collector falls just slightly below the Fermi level of the emitter. However, at higher bias when the transmission coefficient begins to increase rapidly and there are a lot of empty states in the collector for the electron to tunnel into, the current rises fast. This is also seen in Eq. (2.34) where the exponential dependence of D(E) upon $(eV)^{-1}$ causes a rapid rise in current with increasing bias.

The discussion so far has not take into account the existence of band bending at the interfaces. In many cases undoped buffer layers are included at the emitter-barrier and collector-barrier interfaces. When a bias V is applied across the barrier band bending occur at these interfaces. The band bending creates regions of accumulation (and possibly a quasi-two dimensional electron gas (2DEG)) at the emitter side and depletion at the collector side (Fig. 2.5).

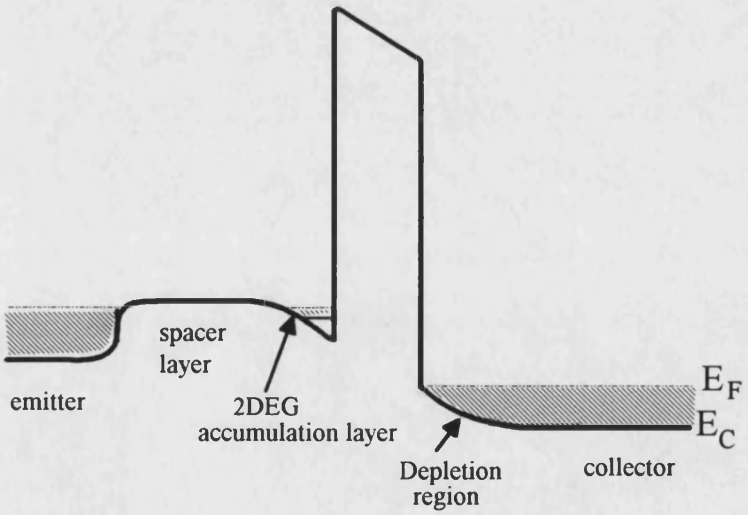

Figure 2.5 : A sketch of a single barrier structure including band bending and a 2DEG at the interface.

Duke (1969) also mentions the presence of a partially reflecting boundary for electrons at the interfaces at higher biases. Resonances appear in the transmission coefficient at energies near those of the pseudo-bound states in the triangular potential defined by the top of the potential barrier and an infinitely high potential wall. The resonances cause oscilations in the zero-temperature current if the exact form of $D(E_x)$ is used in Eq. (2.29). These oscillations are not predicted by the WKB analysis because the effect of the partially reflecting interface is neglected. They are also difficult to observe experimentally because of fluctuations in the height and thickness of the barrier.

The effective mass of an electron is related to the curvature of the energy dispersion curve by

$$m^* = \hbar^2 \left(\frac{\partial^2 E_k}{\partial k^2} \right)^{-1}$$

If the curvature of the conduction band minima is large, the effective mass is expected to be very small and if the curvature is small then the effective mass of the electron is expected to be large. The transmission coefficient decreases with increasing effective mass. Therefore an electron with smaller effective mass has a greater tunnelling coefficient through the barrier. Figure 2.6 shows current-voltage characteristics for a barrier 0.2 eV high and 10 nm wide at T = 0 K. Curves with different electrode effective electron masses are plotted. Pronounced oscillations are observable at voltages larger than the barrier height i.e. at ~0.3 V and ~0.5 V. These features reflect an enhanced tunnelling coefficient for certain voltages and are a consequence of the constructive interference of the incident and reflected waves in the barrier. The oscillations are most pronounced when the difference between the effective mass of the electron in the barrier and in the electrode is the

largest. This interference phenomenon is called resonant Fowler-Nordheim tunnelling.

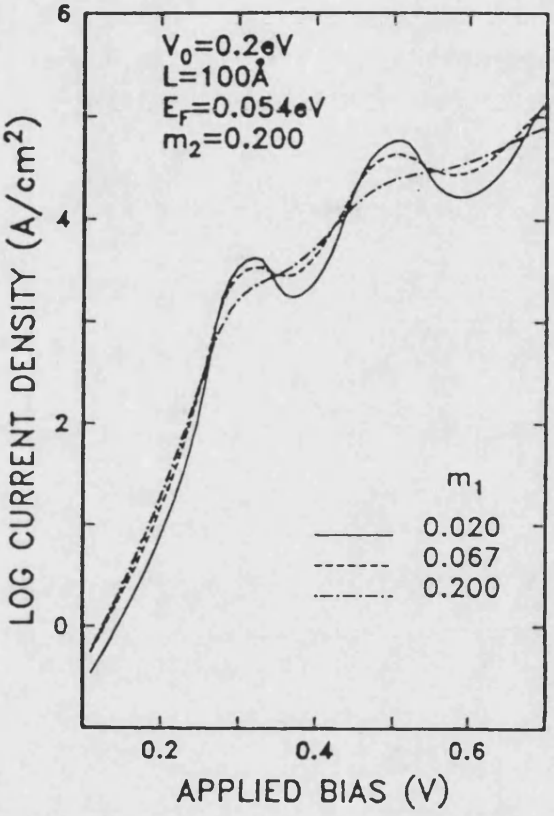

Figure 2.6 : Log current density versus applied bias for a barrier 0.2 eV high and 10 nm wide at 0 K. (After Mendez (1988)).

2.4 Double Barrier Resonant Tunnelling Diodes

In addition to single barrier diodes, double barrier structures are also commonly studied due to the existence of resonant tunnelling. This in turn has opened up studies of other quantum transport phenomena such as tunnelling via Landau-levels. We have seen that the transmission coefficient ($D(E_x)$) of an

electron incident on a single barrier with energy (E_x) less than the barrier height (V_0) is a lot less than unity. Consequently the transmission coefficient is expected to be further reduced if a second identical barrier is added to the system. However, it has been shown experimentally and theoretically by Chang, Esaki and Tsu (1974) that for certain incident energies corresponding to bound states in the quantum well between the barriers, the structure can become transparent to electrons. This quantum size effect is known as resonant tunnelling. Its existence was first predicted by Duke (1969) when he noted that :- "A new type of quantum size effect can occur in metal-insulator-metal-insulator-metal junctions when the intermediate metal becomes atomically thin". He then proposed that the same effect would be observed if the metal is replaced with a semiconductor.

2.4.1 Resonant Tunnelling

Tsu and Esaki (1973) have analysed resonant tunnelling in double barrier structures in terms of a coherent process. In this theory the transmission of electrons through double barriers is similar to the Fabry-Pérot étalon in optics where light waves are transmitted through partially reflecting mirrors. The incident electrons that have tunnelled through the first barrier will be reflected back and forth in the well with some of them being transmitted. When the wavelength (or a multiple half-integral) matches the width of the well, the amplitude of the resonant mode builds up and the electron waves, leaking out in both directions, cancel the reflected wave and enhance the transmitted ones.

Figure 2.7 shows a typical structure for a double barrier resonant tunnelling diode with a quantum well embedded between two barriers. The best examples of such kinds of structure are in III-V semiconductors heterostructures where large

band offsets and matching lattice constants are available. These include systems such as GaAs/(AlGa)As, (InGa)As/InP, (InGa)As/(AlIn)As, GaSb/AlSb, etc. (Leadbeater(1990), Weisbuch & Vinter (1991)). Electrons in the well are confined by the barriers such that their motion perpendicular to the interface is quantised, producing a series of quasi-two-dimensional subbands. It is only possible to have quasi-bound states in the well because the barriers are of finite thickness and electrons can always tunnel out again. If the electrons tunnel elastically through the structure we know that the total energy E and parallel momentum $k_{||}$ of the tunnelling electron is conserved and therefore :-

$$k_{||}(\text{emitter}) = k_{||}(\text{well}) = k_{||}(\text{collector}).$$

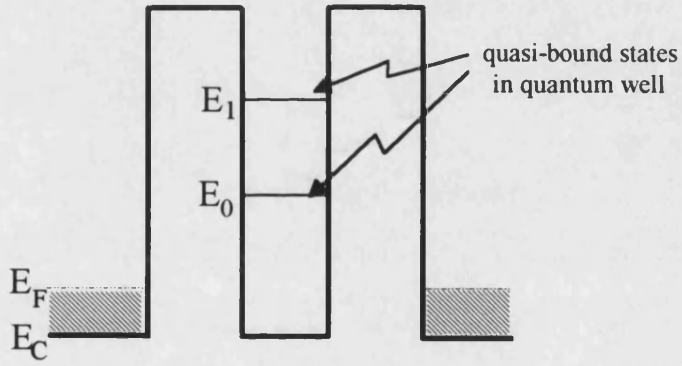

Figure 2.7 : A double barrier structure with quantum well in the middle. Quasi-bound states are shown in the well.

For perfectly parabolic bands, the total energy (even though it is a scalar) can be notionally separated into longitudinal and parallel components :-

$$E = \frac{\hbar^2}{2m^*}\left(k_{\|}^2 + k_x^2\right) = E_x + E_{\|}$$

The energy parallel to the interface, $E_{\|} = \frac{\hbar^2}{2m^*} k_{\|}^2$ is then also conserved which leads in turn to the conservation of energy in the transport direction, E_x. Consequently only electrons with the correct value of E_x ($\cong E_0$) can access the quasi-bound state. Therefore the tunnelling electrons describe horizontal lines across the energy band diagram. If the energy of the incident electron coincides with that of a quasi-bound state in the well, it tunnels through both barriers without attenuation even though its kinetic energy may be considerably less than the height of the potential barriers.

2.4.2 Transmission Coefficient in Double Barrier

In contrast to a single barrier structure the transmission coefficient in a double barrier diode can reach unity even though the electron energy is less than the potential barrier height. Using a transfer-matrix method Toombs *et al.* (1989) showed that the transmission coefficient close to resonance for an asymmetric double barrier is given by :-

$$T_{resonance} = \frac{4T_L T_R}{(T_L + T_R)^2} \left(1 + \frac{(E_x - E_0)^2}{\Delta E^2}\right)^{-1} \qquad (2.38)$$

where

$$\Delta E = \frac{\hbar v_r (T_L + T_R)}{4(w + 2/\kappa)}$$

and

T_L = transmission coefficient of the left barrier.

T_R = transmission coefficient of the right barrier.

w = barrier width.

$$v_r = \sqrt{\frac{2E_r}{m^*}} = \text{electron velocity}$$

$$\kappa = \left(\frac{2m^*(V_0 - E_x)}{\hbar^2}\right)^{1/2}$$

Eq. (2.38) gives a peak transmission of

$$T_{peak} = \frac{4T_L T_R}{(T_L + T_R)^2} \tag{2.39}$$

which is reached when $E_x = E_0$. For a symmetric double barrier i.e. when $T_L = T_R$ Eq. (2.38) reduces to

$$T_{resonance} = \left(1 + \frac{(E_x - E_0)^2}{\Delta E^2}\right)^{-1} \tag{2.40}$$

However, the symmetry of the barriers is soon destroyed upon application of a bias across the structure and the transmission at resonance becomes less than unity. Well away from resonance the transmission coefficient is given by the product of the probabilities of tunnelling through each barrier i.e.

$$T = T_L(E_x)T_R(E_x) \tag{2.41}$$

Figure 2.8 shows a plot of transmission coefficient versus electron energy for a double barrier system with two quasi-confined states. Sharp peaks correspond to resonant tunnelling via the first (E_0) and second (E_1) states in the quantum well. The bound states energies E_0 and E_1 are conventionally measured from the conduction band edge of the well.

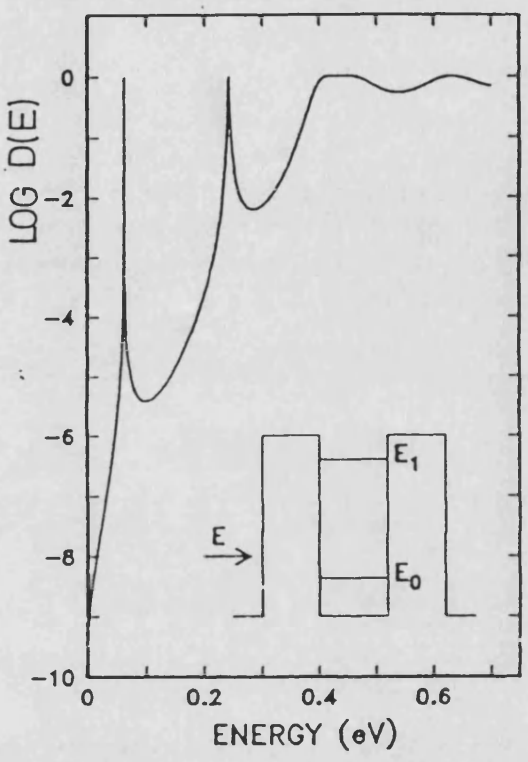

Figure 2.8 : Log tunnelling Probability for a double barrier structure. (After Mendez (1987)).

2.4.3 Current Density

Using Eq. 2.37 for $eV > E_F$ and replacing the transmission coefficient, $D(E_x)$ with that for the double barrier case, Toombs *et. al* (1989) showed that the resonant current at $T = 0$ K is given by

$$J_r = \frac{em^* v_r}{2\pi\hbar^2 w}\left(E_F - E_0 + eV_0\right)\frac{T_L T_R}{(T_L + T_R)} \qquad (2.42)$$

where V_0 is the voltage drop between the emitter and the well. The resonant current reaches a peak value J_p when the bound state energy passes the bottom of the Fermi sea in the emitter and is given by

$$J_p = \frac{em^* v_r E_F}{2\pi\hbar^2 w} \frac{T_L T_R}{(T_L + T_R)} \tag{2.43}$$

The current then drops rapidly with increasing voltage to the valley current

$$J_v = \frac{em^*}{4\pi\hbar^3} E_F^2 T_L T_R \tag{2.44}$$

which yields a current peak-to-valley ratio of

$$\frac{J_p}{J_v} = \frac{h v_r}{w E_F (T_L + T_R)} \tag{2.45}$$

As noted by Leadbeater (1990), the peak current is not very sensitive to the symmetry of the device and increases monotonically with the increasing transmission coefficient of the second barrier. Typically at low temperatures the peak-to-valley ratio can reach values ≥ 10 (Leadbeater(1990)).

2.4.4 Current-Voltage Characteristics

Ideally the current-voltage characteristic assumes a triangular shape but scattering processes normally give rise to a smaller broader peak, and an increase in the valley current as shown in Fig. 2.9. The characteristic in Fig. 2.9 can be explained with the help of Figs. 2.10(a)-(c) which show a double barrier resonant tunnelling diode under different bias conditions.

When the applied bias is low (Fig. 2.10(a)), the Fermi level of the collector falls slightly below the the Fermi level of the emitter and the transmission coefficient is small. At this point a small current flows due to electron tunnelling non-resonantly through the potential barriers. The current increases rapidly when the first bound state, E_0, falls below the emitter Fermi level (Fig. 2.10(b)) and thus resonant tunnelling of electron starts to take place. The peak current is reached

when quasi-bound state level E_0 is in alignment with the conduction band edge of the emitter (Fig. 2.10(c)). This corresponds to the maximum fraction of incident electrons having the same energy as the well state. Beyond this point at still higher biases resonant tunnelling is no longer possible since total energy E and parallel momentum $k_{||}$ cannot simultaneously be conserved causing the current to drop rapidly. When the bias is sufficiently high such that one of the barriers effectively disappears, electrons can pass through the single remaining barrier by Fowler-Nordheim tunnelling (Fig. 2.10(d)). The high transmission coefficient then causes the current to increase almost exponentially with bias.

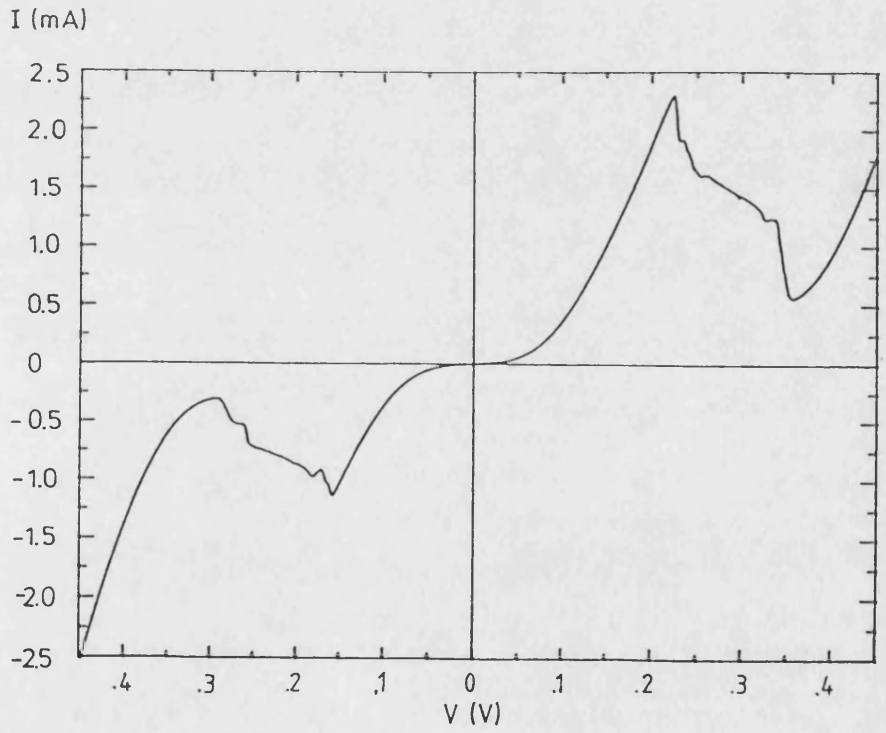

Figure 2.9 : Typical I-V charateristic of a double barrier diode structure.

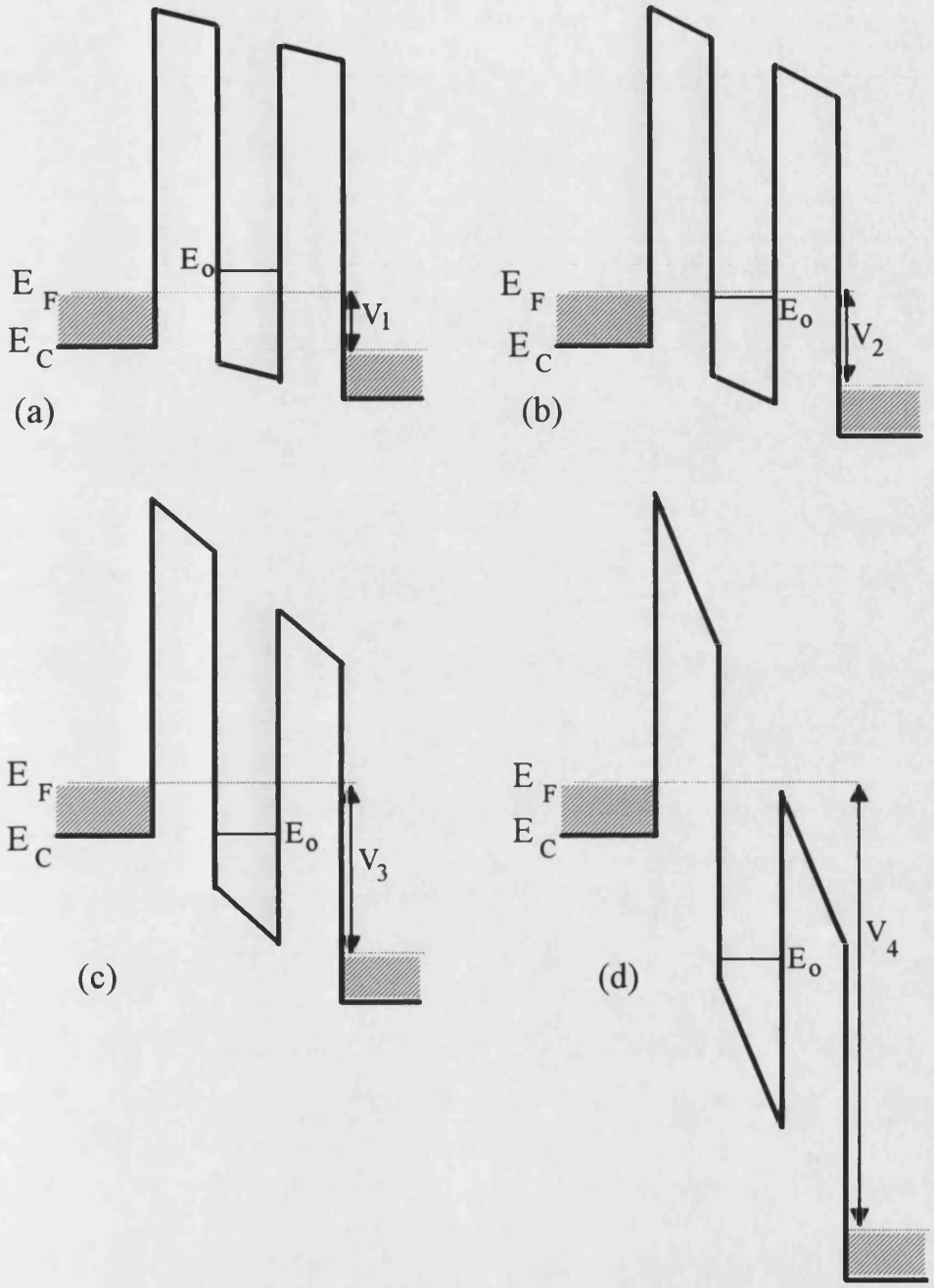

Figure 2.10 : Double barrier structure under different bias conditions; (a) non-resonant; (b) resonant; (c) peak resonant (d) Beyond resonance in the Fowler-Nordheim regime.

The region where the current falls with increasing bias is known as one of *negative differential conductance* (NDC) or *negative differential resistance* (NDR) due to dI/dV being negative. Further resonances are attainable at higher biases if there is more than one quasi-bound state in the well. The number of

resonances also increases when the width of the well increases. Leadbeater (1990) found that the peak-to-valley ratio is reduced with increasing well-width which indicates that the well states are becoming increasingly broadened and begin to overlap.

2.4.5 Tunnelling from a 2DEG

As in the single barrier case spacer layers which are usually lightly doped are included at the electrode-barrier interfaces. The low doping results in the band bending obtained at these interfaces. An accumulation layer with one or more *quasi-two-dimensional bound states* (2DEGs) is formed at the emitter side and a depletion layer at the collector side (Fig. 2.11).

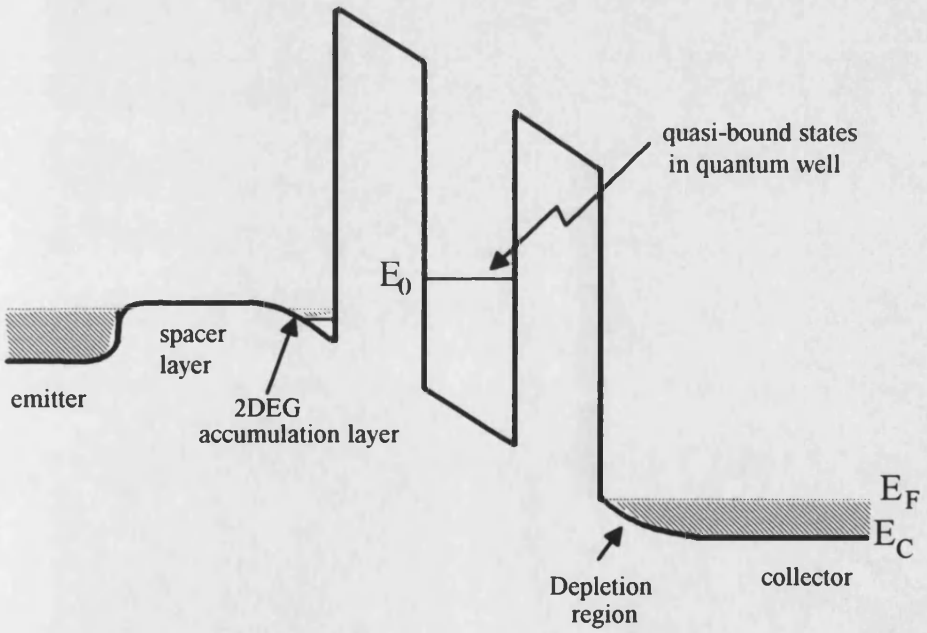

Fig. 2.11 : Conduction band edge of a double barrier structure with spacer layers included creating accumulation and depletion regions.

Under forward bias electrons from the highly doped emitter "hop" across the spacer layer and can either tunnel directly through the barrier, be reflected back

into the emitter or scatter into an unoccupied state of the 2DEG. These 2DEG electrons can then either tunnel into the well or scatter back into a continuum state. Electrons leaving the 2DEG state are continually replaced by electrons from the bulk 3D emitter contact. The difference in the probability of the 'hopping' and tunnelling events will result in a steady state density of electrons in the 2DEG. The introduction of a 2DEG as a source for tunnel electrons changes the tunnelling characteristics dramatically.

For a two-dimensional emitter, the occupied states lie on a Fermi disc in k-space. Theoretically there is only a single applied bias at which the energy level in the 2DEG coincides with the quasi-bound state in the well. Resonant tunnelling occurs when the quasi-bound state energy of the 2DEG matches that of a standing wave state of the well (Eaves (1989)). Therefore the resonance from a 2DEG is much narrower than from a three-dimensional emitter (Fig. 2.12). Spacer layers are also often included to improve the resonant tunnelling characteristics by reducing ionised impurity scattering near the electrodes.

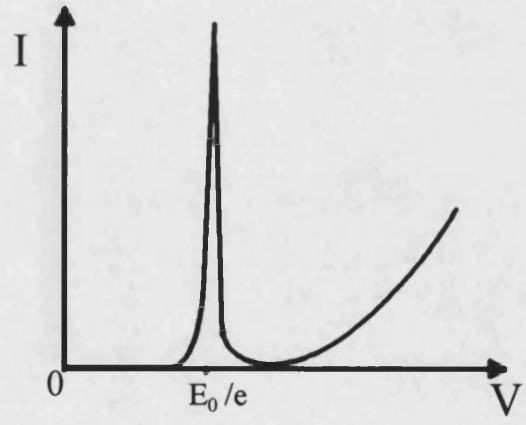

Fig. 2.12 : An ideal current-voltage charateristics of a structure as in Fig. 2.11.

2.4.6 Scattering Processes in Resonant Tunnelling Diodes

In our tunnelling theory we made the assumption that the total energy and parallel momentum are conserved in the tunnel process. This situation has never truly been observed in real samples which normally contain ionized impurities, fluctuations in layer thickness and composition, phonon excitations, and electron-electron interactions (Leadbeater (1990)). Scattering processes break the conservation rules that we laid out before. In the absence of scattering the current should go almost to zero beyond the resonance condition. However, when biased beyond resonance electrons can always be scattered into a resonant state of the well producing a much higher valley current then one would calculate. Due to scattering the peak-to-valley ratio is normally greatly reduced as compared to the theoretical one. Leadbeater (1990) observed peak-to-valley ratios of 3.0 at room temperature and 20.0 at 77 K and Pritchard *et al* (1989) observed peak-to-valley ratios up to 14.9 at 4.2K and up to 8.4 at 77K in reverse bias in a GaAs device.

2.5 Summary

Technological advances in MBE growth have resulted in greatly improved resonant tunnelling characteristics. The aim is to increase the current peak-to-valley ratio and consequently the negative differential conductance. At high temperatures thermionic emission over the barrier causes broadening of the peak and an increase in valley current. This effect is small enough at 77 and 4K to be neglected (Leadbeater(1990)).

The discussion so far has ignored space charge build-up in the quantum well. In certain cases the build-up of electronic charge in the well at resonance

modifies the current-voltage characteristics and give rise to an intrinsic bistability effect (Leadbeater *et al* (1988), Eaves (1989)). This effect is not observable in our work due to the symmetric nature of our structures and will not be discussed further here. Based on a proposal by Esaki and Tsu (1970) it has also been possible to observe resonant tunneling in superlattice structures (Chang *et. al* (1974), Esaki (1990)).

High quality interfaces and band gap engineering yield almost limitless possibilities for creating new structures for physics investigations as well for electronic and optical applications. The effect of different conduction band minima such as (X- or L-minima), hydrostatic pressure and effective mass will be discussed in Chapter 3.

CHAPTER 3

The Physics of Gallium Arsenide Heterostructures

3.1 Basic Properties of $Al_xGa_{1-x}As$ Alloys

3.1.1 The Lattice

Most of the III – V compound semiconductors including gallium arsenide (GaAs) and aluminium arsenide (AlAs) crystalise in the zinc–blende structure. In the case of GaAs(AlAs) the crystal is made up of two interpenetrating face centred cubic sub–lattices of gallium (aluminium) and arsenic atoms displaced by (1/4,1/4,1/4) as shown in Fig. 3.1. Each gallium (aluminium) atom is bonded to four arsenic atoms in a tetrahedral arrangement, and vice versa. The bonds are predominantly covalent but with about 30% ionic character and each bond is 2.45 Å long. In the ternary alloy $Al_xGa_{1-x}As$, the aluminium atoms are usually assumed to be randomly distributed throughout the gallium sites.

The lattice constants (a_o) are 5.6533 Å for GaAs and 5.6611 Å for AlAs. For the $Al_xGa_{1-x}As$ alloy, the lattice constant changes linearly with x and is given

by $5.6533+0.0078x$ Å (Adachi (1985)). Therefore GaAs can form a good heterostructure with $Al_xGa_{1-x}As$ due to almost perfectly matched lattice constants (Jaros (1989), Adachi (1985)) allowing high quality interfaces. The degree of lattice matching between compounds is important in determining the band structure of a heterostructure. An interface between non-lattice-matched materials will be slightly strained distorting the local band structure and modifying its electronic properties.

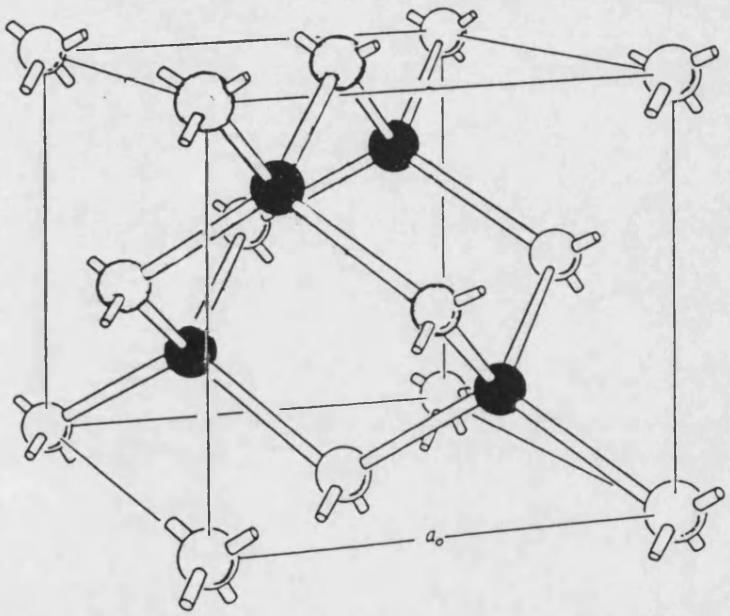

Figure 3.1 : Zinc–blende structure of GaAs

Like other face centred cubic crystals, the first Brillouin zone in reciprocal space is a truncated octahedron (Fig. 3.2). The positions of high symmetry points X (square face centre), L (octahedral face centre) and the zone centre Γ are indicated. The Γ–L direction lies along the line connecting nearest neighbours (<111> direction) in the real lattice. There are four such directions in this octahedron. The Γ–X direction lies along the cubic axis (<100> direction) and there are six such directions in this zone scheme.

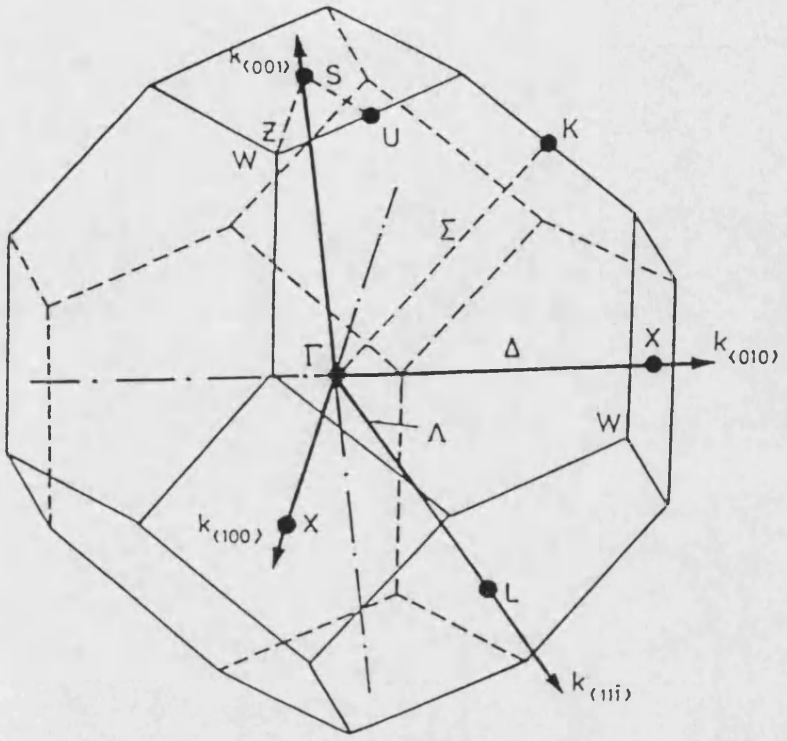

Figure 3.2 : First–Brillouin zone of GaAs showing that it is an octahedron

3.1.2 Band Structure

Figure 3.3 shows the band structures of GaAs and AlAs. For GaAs, the conduction band edge is at the Γ–point which is at the same position as the valence band maximum and therefore it is a direct gap semiconductor. However, for AlAs, the conduction band edge occurs at the X–point and the gap is indirect. The conduction band minima for GaAs and AlAs at 4 K are shown in Table 3.1. These energies are taken relative to the valence band maximum at the zone centre (Jaros (1989)). The discussion here is only concerned with the conduction band properties because we only deal with transport in *n*–type materials.

The positions of the conduction band minima for the ternary alloy $Al_xGa_{1-x}As$ depend on the aluminium concentration. It has a direct gap for $0 \leq x \leq 0.45$ and an indirect gap for $0.45 \leq x \leq 1$ (Mendez(1987)). Casey and Panish (1978) have proposed that the positions of the conduction band minima for $Al_xGa_{1-x}As$ at 300 K are given by these equations (in eV):–

$$E_\Gamma = 1.424 + 1.247x \qquad (0 \leq x \leq 0.45) \qquad (3.1a)$$

$$= 1.424 + 1.247x + 1.147(x - 0.45)^2 \qquad (0.45 \leq x \leq 1) \qquad (3.1b)$$

$$E_X = 1.900 + 0.125x + 0.143x^2 \qquad (3.2)$$

$$E_L = 1.708 + 0.642x \qquad (3.3)$$

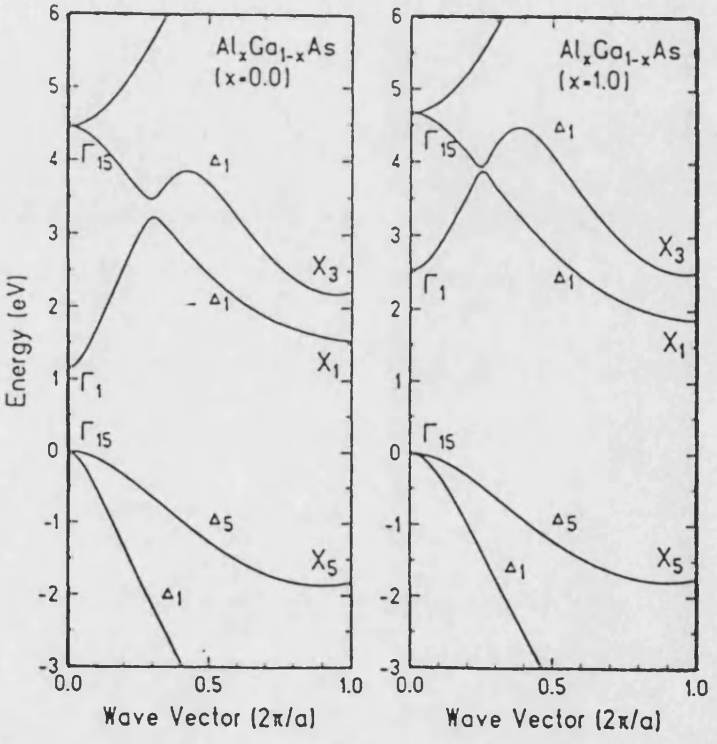

(a) **(b)**

Figure 3.3: Theoretical band structures of (a) GaAs and (b) AlAs

	GaAs	AlAs
E_Γ(eV)	1.52	4.05
E_X(eV)	1.98	2.36
E_L(eV)	1.81	2.90

Table 3.1 : Conduction band edge at Γ, X and L points of GaAs and AlAs at 4 K. (After Jaros (1989)).

Figure 3.4 shows the experimental values of the energy gaps as a function of aluminium mole fraction *x* at room temperature. The aluminium concentration where the Γ and X bands cross is not known with certainty at the present time but it is reported to be between 35% – 45 % of aluminium (Jaros(1985)).

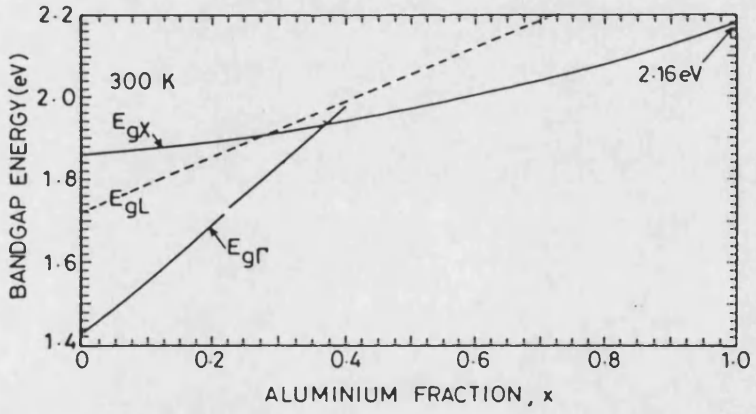

Figure 3.4 : Experimental values of E_Γ, E_X, and E_L at 300 K for $Al_xGa_{1-x}As$ shows near-linear variation with Al concentration. (After Jaros (1989)).

3.1.3 Band Offsets

If GaAs and AlAs are arranged in a heterostructure, the alignment of the bulk band structures causes the Γ–point of AlAs to lie about 1 eV higher in energy than the Γ–point of GaAs. The X–point in AlAs is then about 0.35 eV lower than that in GaAs and about 0.16 eV above the GaAs Γ–point (Mendez *et al.* (1986 & 1990)). These values are obtained assuming that the ratio conduction:valence band offset is 60:40 (Austing *et al.*) which we used in this work.

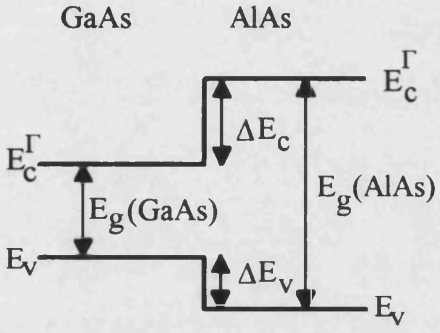

Figure 3.5: Band alignment between GaAs and AlAs with band offsets ΔE_V and ΔE_C.

The conduction (valence) band offset (Fig. 3.5) is the measure of discontinuity between the conduction (valence) band edges of the two materials in a heterostructure. Batey *et al.* (1985) measured the ratio ΔE_c:$\Delta E_v \cong 60{:}40$ for $x \leq 0.45$. Some other values that have been used by other workers are $\Delta E_v \cong 0.55x$ (Bonnefoi *et al.* (1988)) and ΔE_c:$\Delta E_v \cong 63{:}37$ (Pritchard *et al.* (1990)). While Mendez *et al.* (1986) used the following band discontinuities (in eV) in their calculation :–

$$\Gamma(Al_xGa_{1-x}As) - \Gamma(GaAs) \cong 0.70x \qquad 0 \leq x \leq 0.45 \qquad (4.4a)$$

$$\cong 0.70x + 1.15(x - 0.45)^2 \qquad 0.45 \leq x \leq 1 \qquad (4.4b)$$

$$X(Al_xGa_{1-x}As) - \Gamma(GaAs) \cong 0.44 - 0.42x + 0.14x^2 \qquad 0 \leq x \leq 1 \qquad (4.5)$$

$$L(Al_xGa_{1-x}As) - \Gamma(GaAs) \cong 0.30 - 0.092x \qquad 0 \leq x \leq 1 \qquad (4.6)$$

which then gives the band crossover at $x \cong 0.41$. In this work we used the values given by equations (4.4) - (4.6).

3.1.3 Effective Mass

As noted by Adachi (1985), the effective mass of an electron at the conduction band edge is one of the most important device parameters in the transport mobility. The effective mass of an electron is related to the curvature of the energy dispersion curve by $m^* = \hbar^2(d^2E/dk^2)^{-1}$. The greater the curvature the smaller the electron effective mass. At the Γ–point, the conduction band curvature is large and consequently the effective mass is expected to be small. For example in GaAs the effective longitudinal mass at the X–point ($1.3m_0$) is about 20 times higher than that at the Γ–point ($m^* = 0.067m_0$). The effective masses of electrons at Γ, X and L valleys are shown in Table 3.2 in terms of the electron rest mass, m_0. For an $Al_xGa_{1-x}As$ alloy, the effective masses depend on the Al composition.

	GaAs	**AlAs**	**$Al_xGa_{1-x}As$**
m^*_{Γ}	$0.067m_0$	$0.150m_0$	$0.067 + 0.083x$
m^*_{Xl}	$1.300m_0$	$1.100m_0$	–
m^*_{Xt}	$0.230m_0$	$0.190m_0$	–
m^*_{Ll}	$1.900m_0$	$1.900m_0$	–
m^*_{Lt}	$0.075m_0$	$0.096m_0$	–

Table 3.2 : Effective masses at Γ , X and L band edges of GaAs, AlAs, and $Al_xGa_{1-x}As$. (After Adachi (1985)).

3.1.4 Impurity Levels

When a semiconductor such as GaAs (from the III–V group) is lightly doped with an n–type dopant from group IV (Si for example) the energy level of the created impurity lies just below the conduction band edge of the bulk GaAs (Fig. 3.6(a)). As the density of the dopant is increased these energy levels become broader and form an impurity band (Fig. 3.6(b)). As the crystal is increasingly heavily doped the impurity band eventually overlaps the conduction band (Fig. 3.6(c)). At this point the bulk crystal begins to exhibit metallic behaviour. The transition to this metallic behaviour is called the Mott–transition or the Metal–Insulator Transitions (MIT) (Leadbeater (1990)). The critical concentration (n_{cr}) at which this transition occurs is given by (Harris (1991)) :–

$$a_0(n_{cr})^{1/3} = 0.25 \qquad (4.7)$$

where a_0 is the Bohr radius for the impurity. The GaAs electrodes used in this work are all heavily doped and the Fermi level lies above the conduction band edge so that low temperature measurements are possible.

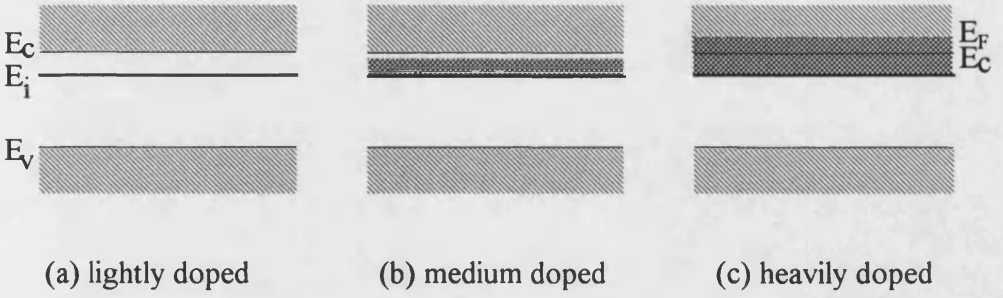

Figure 3.6 : Impurity level in a semiconductor energy bands with different doping concentration.

3.2 Electron Transport

Electron transport through a potential barrier depends strongly on the band structure and band edge discontinuities of the host materials. The tunnelling electron can be either Γ–, L– or X–like depending on its effective mass and the band structure of the host semiconductor. Therefore an understanding of the energy bands of the material is essential in order to describe the transport phenomena in a semiconductor structure. The discussion here is only concerned with conduction electrons in the Γ, X or L valleys. We will see that under certain circumstances the existence of secondary valleys open up alternative transport channels for electron transport.

The samples that we have investigated in this work are based on either single or double barrier diodes of GaAs/$Al_xGa_{1-x}As$. We can classify the transport phenomena according to whether the barrier is direct or indirect. The lowest conduction band edge of $Al_xGa_{1-x}As$ depends on the Al concentration. Its band gap is direct if $x \leq 0.45$ or indirect if $x \geq 0.45$ (Mendez *et al.* (1986)). In all tunnelling processes it is still possible for the total energy, and the momentum parallel to the interface ($k_{\|}$) to be conserved except for tunnelling via the transverse X minima (X_t) direction where scattering must occur (Mendez (1987)).

3.2.1 Direct Barrier

A single layer of $Al_xGa_{1-x}As$ with $x \leq 0.45$ sandwiched between doped layers of GaAs is the simplest direct single barrier device. The fundamental gaps of GaAs and $Al_xGa_{1-x}As$ are at the same point of the Brillouin zone and the energy difference Γ(AlAs)–Γ(GaAs) forms the lowest potential barrier in this structure. This is illustrated in Fig. 3.7 where the electrodes are heavily doped n^+–GaAs.

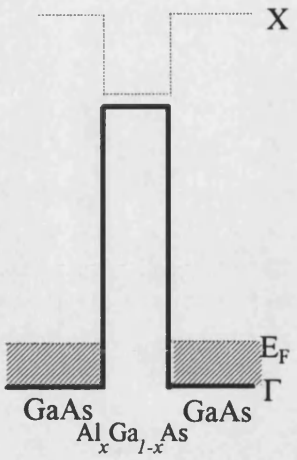

Figure 3.7: X and Γ profile of a single barrier GaAs/$Al_xGa_{1-x}As$/GaAs diode ($x \leq 0.45$).

Assuming momentum conservation in the direction parallel to the interface, the transmission coefficient of an electron tunnelling via the lower Γ–Γ barrier is much higher than via the larger Γ–X barrier. Therefore, in a direct barrier structure, tunnelling of a Γ electron from the GaAs electrode is dominated by the Γ–point potential barriers. In a single barrier case we refer to this as Γ–Γ–Γ tunnelling (Mendez *et al.* (1986), Mendez (1987)).

In a double barrier structure (Fig. 3.8), a GaAs quantum well confined by two direct barriers forms quasi–bound states in the well. A Γ electron can tunnel resonantly via these states when its energy equals the energy of the quasi–bound state or tunnels non–resonantly otherwise (see Chapter 1). This pure Γ–Γ tunnelling in direct barriers has been confirmed by Bonnefoi *et al.* (1988) in an MOCVD grown double barrier structure of $Al_{0.35}Ga_{0.65}As$/GaAs/ $Al_{0.35}Ga_{0.65}As$ (experimentally and theoretically) and also by Austing *et al.* (1990) in an MBE grown double barrier structure of $Al_{0.33}Ga_{0.67}As$/GaAs/ $Al_{0.35}Ga_{0.65}As$.

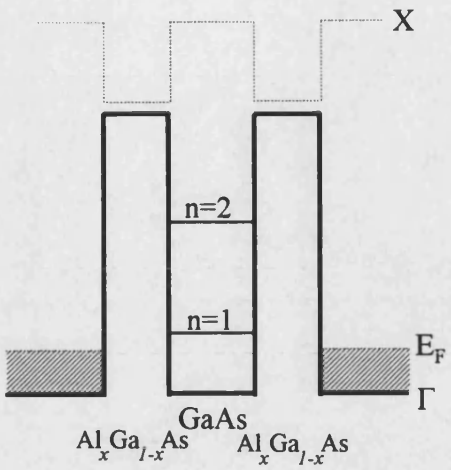

Figure 3.8: X and Γ profile of a double barrier $Al_xGa_{1-x}As$/ GaAs/$Al_xGa_{1-x}As$ diode ($x \leq 0.45$).

3.2.2 Indirect Barrier

In the example above increasing the aluminium concentration will raise the Γ–point energy while at the same time lowering the X–point energy. Beyond the crossover value at $x \geq 0.45$, the X–point lies at lower energy than the Γ–point creating an indirect barrier structure. The most extreme case corresponds to $x = 1$ when the band discontinuities in the GaAs/AlAs structure Γ(AlAs)–Γ(GaAs) ≅ 1.0 eV, X(AlAs)–Γ(GaAs) ≅ 0.16 eV and X(GaAs) – X(AlAs) = 0.35 eV (Mendez *et al.* (1986)). Therefore when AlAs is sandwiched between GaAs layers, there are two extreme barrier profiles formed by the Γ– and X–conduction band minima. Mendez *et al.* (1986) have shown that the potential barrier seen by tunnelling electrons is determined by the X–minima in the AlAs which is at much lower energy than the Γ–minimum. Figure 3.9 shows conduction band edges of a GaAs/AlAs single barrier diode. The Γ–profile of this structure represents a resonant tunnelling diode in a similar way to the case of tunnelling in a direct energy gap barrier.

The role of potential barriers and wells are reversed in the X–profile. In this case quantum wells are formed in the AlAs layers confined by the X(GaAs). There are two distinct types of X–minima in AlAs. One is in the transport direction <100> (X_l) with high effective mass ($1.1m_0$) while the others are in the direction perpendicular to this (<010>) (X_t) with lower effective mass ($0.19m_0$). This is illustrated by the constant energy surfaces in Fig. 3.10 showing the Fermi sphere of GaAs and 3 of the 6 ellipsoids of AlAs.

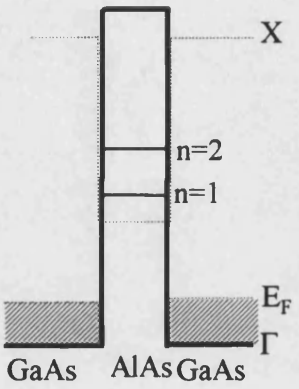

Figure 3.9: X and Γ profile of a GaAs/AlAs barrier structure.

In this case a Γ electron can transfer to the X–minimum at the first interface, propagate through the barrier layer and then transfer back to the Γ–minimum at the other interface (Γ–X–Γ tunnelling). There is also the possibility that a Γ electron transfers to the X–minimum and remains there through the rest of the structure (Γ–X–X tunnelling)(Landheer *et al.* 1989). The parallel component of momentum $k_{\|}$ can only be conserved if the X–minimum in the transport direction (X_l) is involved (Landheer *et al.* (1989), Mendez (1987)). However, due to its higher effective mass (more than 10 times compared to the effective mass at the Γ–minimum), the X_l–related component of the tunnel current is strongly

suppressed. This is because the tunnelling probability decreases exponentially with increasing effective mass.

Tunnelling via the X_l minimum has been observed by Landheer *et al.* (1989) in a single barrier GaAs/AlAs diode with barrier thickness greater than 4nm, while the Γ-minimum dominates in thin barriers (<3nm). The heavy effective mass in the tunnelling via the X_l–minimum is confirmed by their calculations.

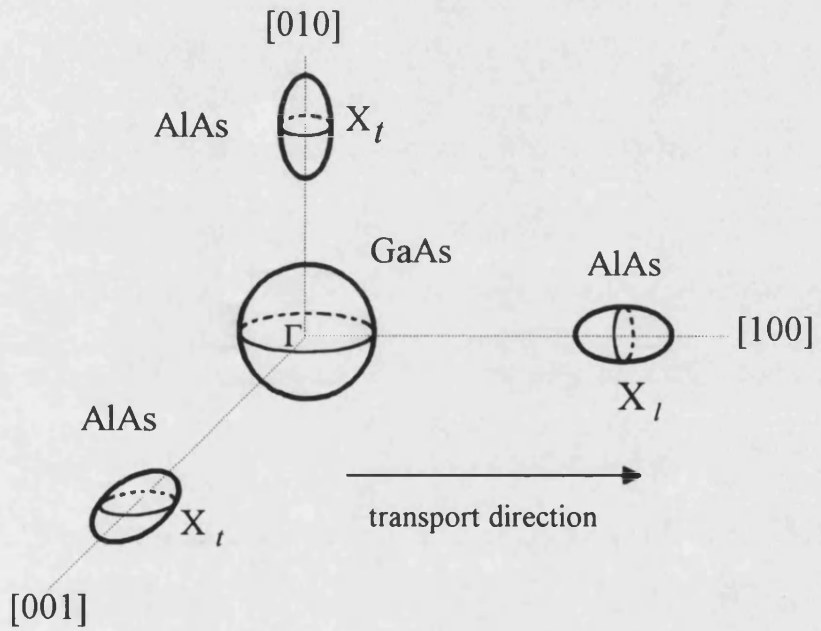

Figure 3.9 : Constant energy surfaces for GaAs and AlAs.

There is also the possibility that the Γ electron transfers to the transverse X–minima (X_l) in which case $k_{\|} > k_F$ and can not be conserved during tunnelling. This requires a large parallel momentum scattering event sideways towards the Brillouin zone boundary. Such an event may occur due to phonon, interface roughness or random alloy scattering (in AlGaAs) (Mendez (1987)). Note that phonon absorption is negligible at low temperatures and random alloy scattering does not exist in binary heterostructures (Landheer *et al.* (1989)).

When the role of the potential well and barrier is reversed in the X–profile, new quasi–bound states exist in the AlAs layer due to confinement by X(GaAs) barriers. Electrons can tunnel resonantly via confined states in AlAs and produce other NDR regions in addition to those due to the Γ–confined states. The NDR from these confined states is normally weaker and is often hidden in the non–resonant current. Resonant tunnelling via X states has been observed by Mendez et al. (1986, 1987) and by Austing *et al.* (1989) in a single AlAs barrier structures.

In addition Bonnefoi *et al.* (1987,1988) have observed resonant tunnelling via quasi–bound states in the GaAs well confined not only by the AlAs Γ–point potential barriers but also by AlAs X–point potential barriers. The quasi–bound X states are related to the longitudinal X–minima with large effective mass and at lower energy than the quasi–bound Γ states and give rise to an extra current peak at a lower voltages.

3.2.3 The Effect of Application of Hydrostatic Pressure

It is known that the band gaps of GaAs and its alloys are modified by the application of hydrostatic pressure. The pressure coefficients of the E_Γ, E_X, and E_L respectively are shown in Table 3.3 below for GaAs, AlAs and $Al_xGa_{1-x}As$ alloys (Adachi (1985)). We see that only dE_Γ/dP depends on the concentration of Al in the alloy while dE_X/dP and dE_L/dP remain the same for all values of x.

From the data given we infer that the Γ–X and Γ–L barriers reduce at 12.3 and 8.7 meV/kbar respectively under hydrostatic pressure while the Γ–Γ barrier remains almost unchanged. For the case of direct AlGaAs barriers, the effect of pressure should be to cause a direct/indirect transition as the X–point energy falls below the Γ–point energy at a critical pressure p. For indirect AlGaAs barriers, the

effect of pressure should be to reduce the X barrier height even more and hence increase the tunnelling current density. Thus the importance of the X–minima increases with increasing pressure.

There are therefore two methods that can be used to investigate transport phenomena in $Al_xGa_{1-x}As$/GaAs devices. One can either make different samples with different Al concentrations or one can place a single sample under hydrostatic pressure thus avoiding the need to prepare many different samples. The latter has the advantage that we can exclude other factors such as different degrees of interface roughness or different impurity concentrations.

	GaAs	**AlAs**	**$Al_xGa_{1-x}As$**
dE_Γ/dP (meV/kbar)	11.5	10.2	$11.5 - 1.3x$
dE_X/dP (meV/kbar)	–0.8	–0.8	–0.8
dE_L/dP (meV/kbar)	2.8	2.8	2.8

Table 3.3 : Pressure coefficient of Γ, X and L band edges of GaAs, AlAs, and $Al_xGa_{1-x}As$. (After Adachi (1985)).

Hydrostatic pressure measurements of single or double barrier GaAs/AlAs structures have been performed by many groups e.g. Austing *et al.* (1990,93), Mendez *et al.* (1986,87,88,89), Cury *et al.* (1990), Alexander *et al.* (1989) and Pritchard *et al.* (1989,90). The pressure dependence of the peak to valley ratio shows that the Γ(GaAs)–X(AlAs) barrier is strongly involved in the electron tunnelling. The lowering of this barrier with pressure is expected to increase the non–resonant tunnelling component and lead to rapidly increasing valley currents.

CHAPTER 4

Introduction to Hydrostatic Pressure System

4.1 Introduction

The LC10 high pressure cell (also known as a self-clamping cell) is supplied by UNIPRESS, High Pressure Research Center, Poland. It is made up of a cylindrical shaped cell body, a screwed in sample stage with seals, a piston and anvil with seals at the other end, and a safety jacket for protection (Fig. 4.1). The high pressure bore is only 10 mm in diameter and can accommodate a sample about 6 x 10 mm^2. A number of electrical leads connect the samples to the outside measurement system. The cell body, sample stage, and piston were made from a beryllium-copper alloy and could withstand pressures up to 1.1 GPa (11 kbar) at room temperature.

A large hydrostatic pressure is achieved by compressing a transmitting liquid with a hydraulic press via a plunger while the pressure inside the cell is constantly monitored with a manganin pressure gauge. The transmitting media that we normally used were either a mixture of petroleum-ether or a 1:1 mixture of

petrol and transformer oil. Upon cooling to liquid nitrogen temperature the pressure drops by 3 - 4 kbar which is mostly due to liquid contraction. The brass seals are very effective at retaining the high pressure in the cell.

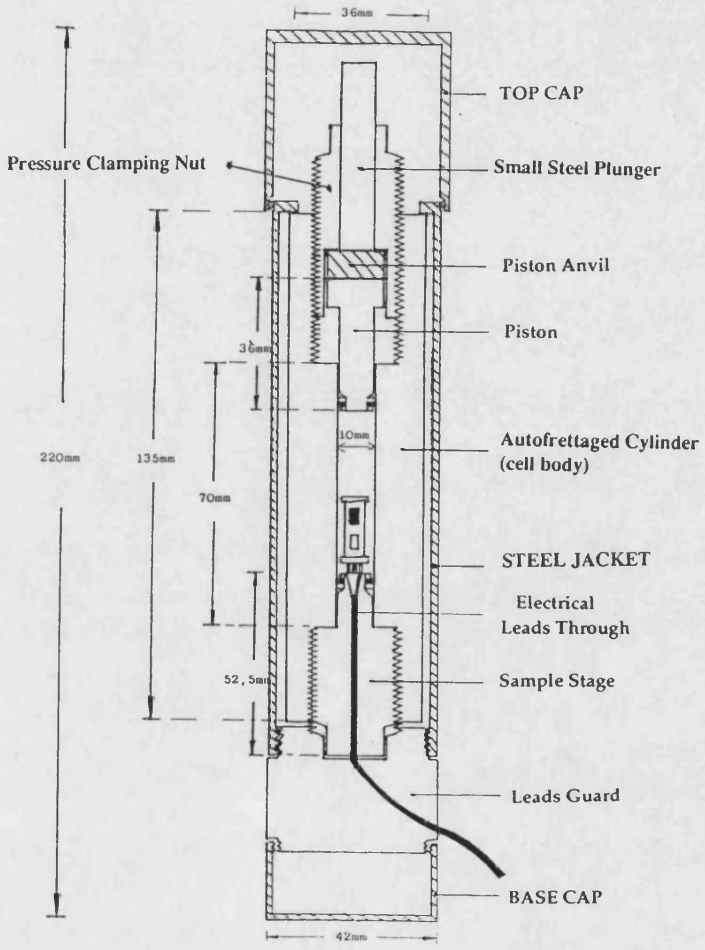

Figure 4.1 : A complete assembly of a self-clamping pressure cell.

For the measurements at liquid nitrogen temperature the pressure cell was lowered slowly into a bath of liquid nitrogen until it was fully immersed and the temperature in the cell was monitored using a copper-constantan thermocouple. Pressure measurement in a self-clamping pressure cell is performed *in situ* inside

the pressure cell itself normally with a small pressure gauge which is fitted onto the sample holder. A number of pressure gauges exist which are suitable for this purpose. These include manganin wire, Zeranin wire, gold-chromium wire or an indium antimonide semiconductor pressure gauge. The resistance of all these materials changes with pressure and temperature and provided these changes are approximately linear they will be suitable as pressure gauges. Among these manganin is most widely used as a pressure gauge. The gold-chromium gauge was not used because of its inferior pressure coefficient and larger temperature dependence as compared with manganin (Peggs (1983)). Au-Cr wire also cannot be soft soldered, has lower resistivity, and larger thermal e.m.f. (Boren *et al.* (1965)). Electrical resistance pressure gauges are usually preferred because they are rather sensitive to pressure and very reliable.

Manganin wire is an alloy made of 84% copper, 12% manganese and 4% nickel (Peggs (1983)), Samara *et al.* (1964)). It is a face-centred cubic solid solution of manganese and nickel in copper. The isotropic compressibility of the cubic lattice causes non-permanent changes in the properties of the material upon applying hydrostatic pressure. The wire is supplied by Isabellenhütte, Heusler, of Germany. Its diameter is 0.08 mm and it has a resistance of 86.3 ohms per meter. Bridgman was the first person to use manganin extensively as a pressure gauge. This followed a recommendation from Lisell in his Ph.D. work in 1903 (Bridgman (1958), Pegs (1983)). Subsequently manganin has gained great popularity among those who work with high pressure equipment as well as in industry. Lisell found that the resistance of the manganin varies almost linearly with pressure up to about 4 kbar (Peggs (1983)). In fact the pressure dependence of resistance, R, of manganin is very nearly linear from $0 < p < 30$ kbar (Jayaraman *et al.* (1967), Thompson (1984)). It is interesting to note that manganin is developed for

optimum use at room temperature. Its resistance goes through a maximum at room temperature; i.e. dR/dT = 0 (Samara *et al.* (1964)). Therefore at around room temperature the temperature coefficient of the resistance of manganin is negligible.

The manganin wire is also known to have a very small temperature coefficient well away from 300 K making it suitable for use at either low or high temperatures (Peggs (1983)). In addition manganin gauges are easy to prepare and occupy little space.

4.2 Pressure Gauge Preparation

In a good pressure gauge the resistance should be free from hysteresis effects (or such effects should be very small and negligible), should not depend on the surface or microstructure, have a very small temperature coefficient, and small thermoelectric potential with respect to copper (Peggs (1983)). In order to achieve these characteristics the wires must undergo an aging or seasoning process. This process normally includes heating and cooling at certain temperatures for a specific length of time depending on which kind of metal is being used. However, after all this processing the wire may still show some small nonlinearity.

The pressure p(T) at temperature T is determined for wire gauges by the following equation (Bundy (1961)) :-

$$p(T) = \frac{R(p,T) - R(0,T)}{R(0,300).k_0(T)} \qquad (4.1)$$

where

R(p,T) is the resistance at temperature T and pressure P,

R(0,T) is the resistance at temperature T and atmospheric pressure,

R(0,300) is the resistance at room temperature and atmospheric pressure,

$k_0(T)$ is the pressure coefficient at temperature T.

In contrast, for the indium antimonide gauge, which was sometimes used here pressure, p(T) at temperature T is determined by the equation :-

$$p(T) = 30.9 \ln\left[\frac{R_{(p,T)}}{R_{(0,T)}}\right] \qquad (4.2)$$

4.2.1 Heat Treatment

To make a reliable pressure gauge, about 1 meter of manganin wire is cut and seasoned (i.e. temperature and pressure cycled) (Bridgman (1958), Peggs (1983), Samara *et al.* (1964)). The wire is heated at 140 °C in an oil bath or oven for a period of time given by

$$t = \frac{(2.929 - \log\theta)}{0.0165} \qquad (4.3)$$

where t is in hours and θ is in °C (Peggs (1983)). Immediately after the heating cycle the hot manganin wire is quenched in liquid nitrogen and left for two hours.

4.2.2 Pressure Cycling

After heat treatment the wire gauges must undergo a few pressure cycles. The gauge is normally put under a very high pressure which is greater than the maximum working pressure for a couple of hours. The pressurisation is subsequently repeated a few times (Peggs (1983)). This process is intended to reduce hysteresis effect and improves the reliability of the gauge.

The accuracy of the manganin gauge that has undergone this process is known to be about ± 0.01 kbar up to 10 kbar, and ± 0.2 kbar up to 25 kbar (Samara *at al.* (1964)). The sensitivity of a pressure gauge to a given temperature change is evaluated from the ratio of the temperature coefficient of resistance, B, and the pressure coefficient, k_0 (Peggs (1983)) :-

$$\left[\frac{dP}{dT}\right]_R = \frac{B}{k_0} \qquad (4.4)$$

4.2.3 Gauge Construction

The performance and reliability of a pressure gauge also depends on the way it is built into the pressure system. There are three different methods of achieving this as described by Peggs (1983) :-

a) The wire is loosely wound on a bobbin.

b) A coil is wound onto a former having an accurately machined helical groove.

c) The wire is bent into the form of a hairpin.

Yamamoto discovered that the performance of all these methods was about the same if the gauge was properly constructed (Peggs (1983)). During the construction process, it is important that the wire is not permanently strained. The gauge also should be wound non-inductively in order to minimise the electrical pick-up in the measurements (Peggs (1983), Wang (1967)). This is easily achieved by bending the wire in the middle into a hairpin shape before winding onto a former.

For an accurate pressure measurement, the resistance of the gauge is measured by a four-terminal technique i.e. with separate voltage- and current-sensing leads. The joint between electrical leadthrough wires and the gauge is best formed by brazing with gold or silver (Peggs (1983)). The next best method is to use a spot-welder. Another alternative is to use normal tin-lead solder but this produces large hysteresis effects as reported by Rostocki and Wisniewski (Peggs (1983)).

4.3 Pressure Gauge Calibration

To determine the pressure in the pressure cell we use any physical property of a gauge which changes with pressure. The best gauge is one in which this property changes linearly or almost linearly with pressure. For example there are electrical resistance pressure gauges, voltage pressure gauges and volume pressure gauges. These all have to be calibrated against a standard pressure reference. The accuracy of these calibrated gauges then depends on their pressure and temperature dependencies, and the standard reference that has been chosen.

Some commonly used standard references are the dead-weight (free piston) gauge and mercury manometer (Bradley (1969), Bridgman (1958), Sherman *et al.* (1987)). These are also called primary gauges because pressures are measured directly interms of force/area. Pressures are determined from measurements of the effective area 'A', gravity 'g' and the masses of a piston plus weights 'm'. Therefore the accuracy of this gauge depends on the accuracy of these three measurements. Even though we can measure the quantities of force and area with high accuracy the ratio F/A will nevertheless incur some uncertainties.

The mercury manometer is, however, not very practical to use for very high pressure gauge calibration. Pressure is determined from the expression $p = \rho gh$. Therefore the accuracy depends on the measurement of the density of the mercury 'ρ', gravity 'g' and the mercury height 'h'. At 1 bar the mercury column is already 76 cm high. Thus for a pressure of 10 kbar the column becomes ridiculously high. A technique has been devised to lower the height of the mercury column. This was achieved by using a series of mercury columns connected by a less dense fluid. However, the system was still too bulky to use when compared with the other alternatives.

Since a primary gauge is normally too bulky, a secondary pressure gauge can be calibrated against another known secondary gauge or some known fixed points. Some of these are accurate to within ±0.1 bar (Sherman *et al.* (1987)).

4.4 Calibrating Manganin against an InSb Pressure Gauge

4.4.1 Experimental Procedures

In this experiment we used the InSb pressure gauge as a standard reference. We did not use fixed points or primary gauges due to a lack of suitable facilities for that purpose. Nevertheless the InSb pressure gauge was accurate enough for our purposes. It had been calibrated by the supplier and was guaranteed to have an accuracy of about 0.001 kbar.

The manganin gauge was seasoned at 140 °C for 6 hours before being quenched and left in liquid nitrogen for 2 hours. The wire was then loosely wound non-inductively around the sample holder. It was cycled between room and liquid-

nitrogen temperature, and between ambient pressure and > 10 kbar more than 5 times following a recommendation by Thompson (1984).

As mentioned above, the pressure in the cell was monitored with an InSb gauge while the temperature was monitored using a copper-constantan thermocouple. All the temperatures, pressures and manganin resistance measurements were performed using standard four-probe dc techniques and data were captured with a BBC computer. In this way the resistance of the InSb gauge could be automatically converted into a corresponding pressure value.

A 1:1 mixture of petrol and transformer oil was used as the pressure transmitting medium. The manganin gauge was calibrated at different temperatures from 290 to 77 K as the pressure cell was lowered slowly into a bath of liquid nitrogen. This method has been proven reliable by Thompson (1984) and Becker *et al.* (1976). All measurements were repeated again upon warming.

The first experiment was performed at atmospheric pressure to determine the temperature coefficient of the manganin. The next experiment was performed at a pressure of about 10 kbar and the pressure cell was again cooled from room temperature down to 77 K. This procedure was repeated in 0.5 kbar steps, down to about 4 kbar at which point we believe that the low temperature pressure becomes ≈ 1 bar. The data at room temperature and 77 K were then used to calculate the pressure coefficient at these two points respectively.

4.5 Results and Discussion

4.5.1 Temperature Coefficient of Manganin

Figure 4.2 shows the temperature dependence of manganin during a thermal cycle and is described by

$$R(T,0) = r + 0.111T - 2.696\times10^{-4}T^2 - 2.075\times10^{-8}T^3 + 5.502\times10^{-10}T^4 \text{ ohm} \qquad (4.6)$$

where r is the resistance at 0 K and atmospheric pressure. r depends obviously on the length of the wire and can be derived from the value of the resistance at other temperatures. R(T,0) is the resistance of the manganin wire at atmospheric pressure and a temperature T. The third and fourth order terms in the polynomial are significant at high temperatures such as 300 K and were included in the calculations.

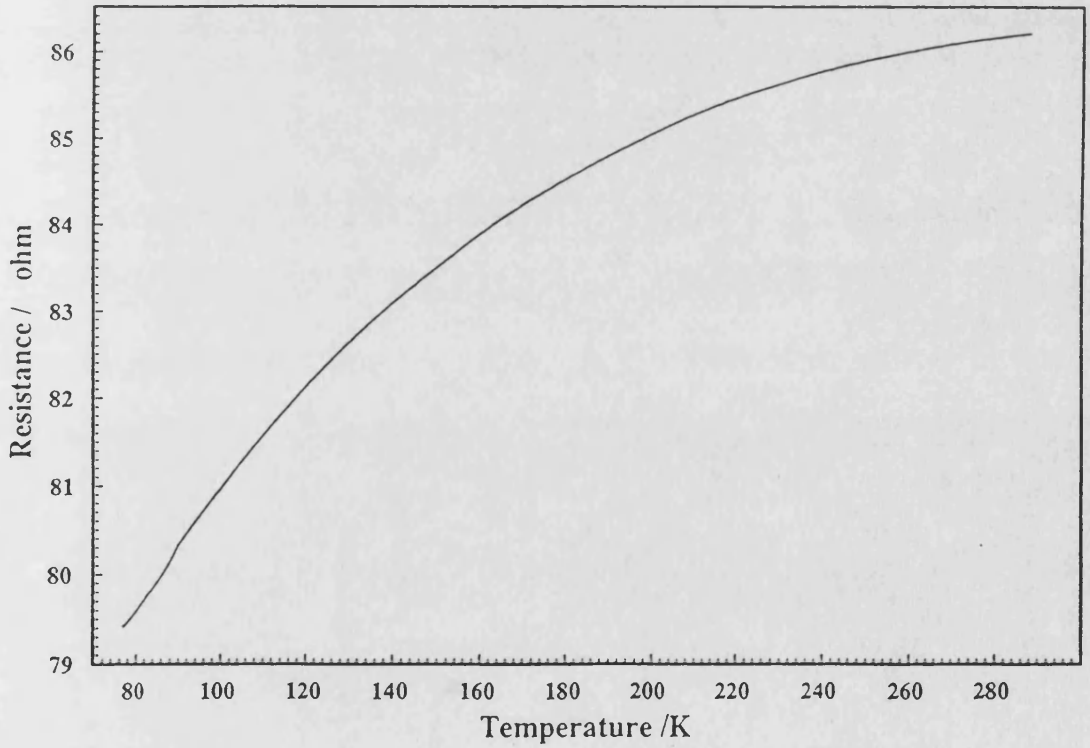

Figure 4.2 : Resistance of a piece of manganin wire as a function of temperature at 1 bar.

4.5.2 Pressure Coefficient of Manganin at Room Temperature

The standard expression for pressure coefficient of manganin gauge (Eq. 4.1) can also be written as

$$k_0 = \frac{\Delta R}{R_0} \cdot \frac{1}{p}$$

where $\Delta R/R_0$ is the normalised resistance change with pressure of manganin at room temperature.

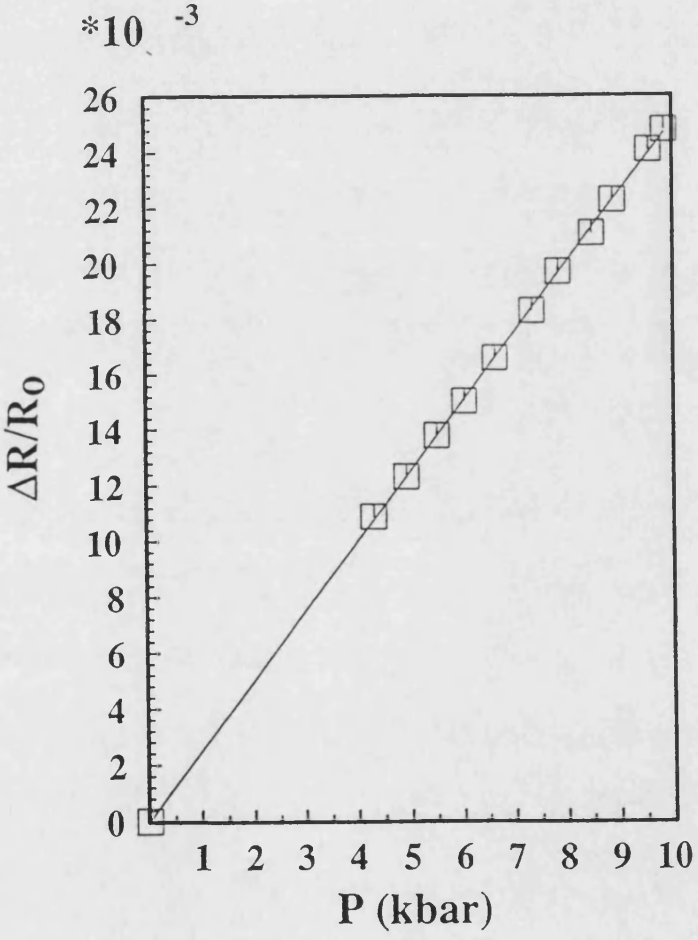

Figure 4.3 : Normalised manganin resistance change as a function of pressure at room temperature.

Since most workers have used 300 K as room temperature, we also use r = r(300,0) which we calculated from Eq. 4.6. Figure 4.3 shows the normalised manganin resistance change as a function of pressure at 300 K. It is very linear up to the maximum pressure of about 10 kbar. This result is in good agreement with the findings of other workers (Fujiwara *et al.* (1980), Jayaraman *et al.* (1967), Nomura *et al.* (1981), Thompson *et al.* (1984)). The pressure coefficient at room temperature was calculated to be $(2.45 \pm 0.02)\times10^{-3}$/kbar. This values is slightly higher than the value given by Peggs *et al.* (1983) ($k_0 = 2.38\times10^{-3}$/kbar), 2.385×10^{-3}/kbar by Becker *et al.* (1976), yet slightly lower than 2.51×10^{-3}/kbar due to Thompson (1984). However this only represents a scatter of about 3%. It is important to note that the pressure coefficient does not depend on the pressure transmitting medium as long as the pressure remains hydrostatic.

4.5.3 Pressure Coefficient at 77 K

The normalised resistance change of manganin as a function of pressure at 77 K is plotted in Fig. 4.4. It can be seen that at 77 K, the plot is not very linear compared to the room temperature data. This is because manganin was prepared to be used at around room temperature. The pressure coefficient was found to be $(1.98 \pm 0.02)\times10^{-3}$/kbar. This is only 1% smaller than the value given by Peggs (1983) which is 2.00×10^{-3}/kbar.

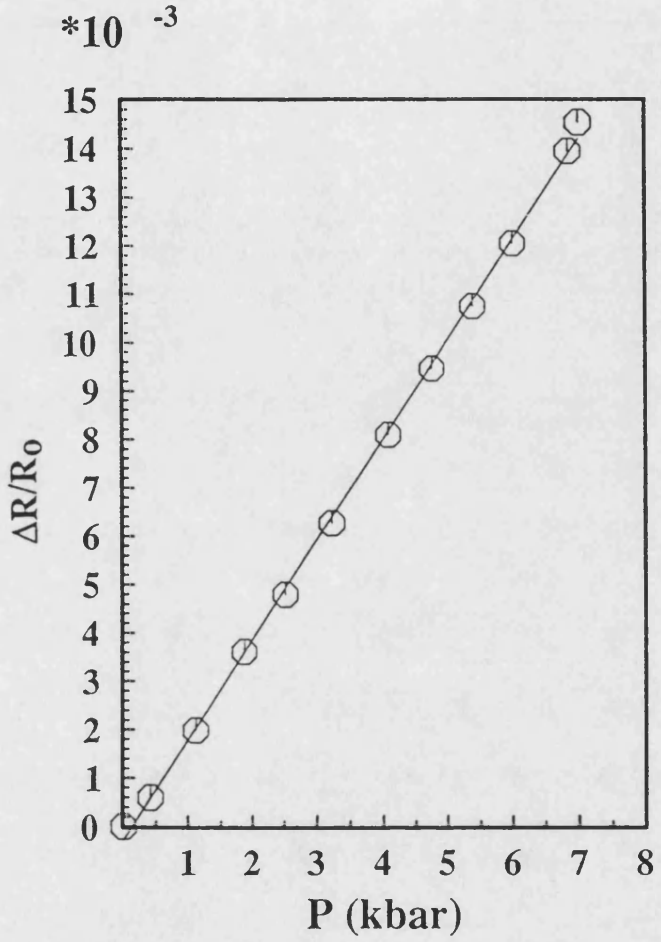

Figure 4.4 : Normalised manganin resistance change as a function of pressure at 77 K.

4.5.4 Temperature Dependence of the Pressure Coefficient

Figure 4.5 shows a plot of the pressure coefficient of manganin as a function of temperature. This can be described by

$$k_0 = (1.3005 + 1.0666\times10^{-2}T - 2.277\times10^{-5}T^2)\times10^{-3}\ /\text{kbar}$$

To our knowledge this is the first measurement of the temperature dependence of the pressure coefficient of a manganin wire gauge. This equation is useful for measurements at different temperatures such as the resistance of superconducting materials under pressure.

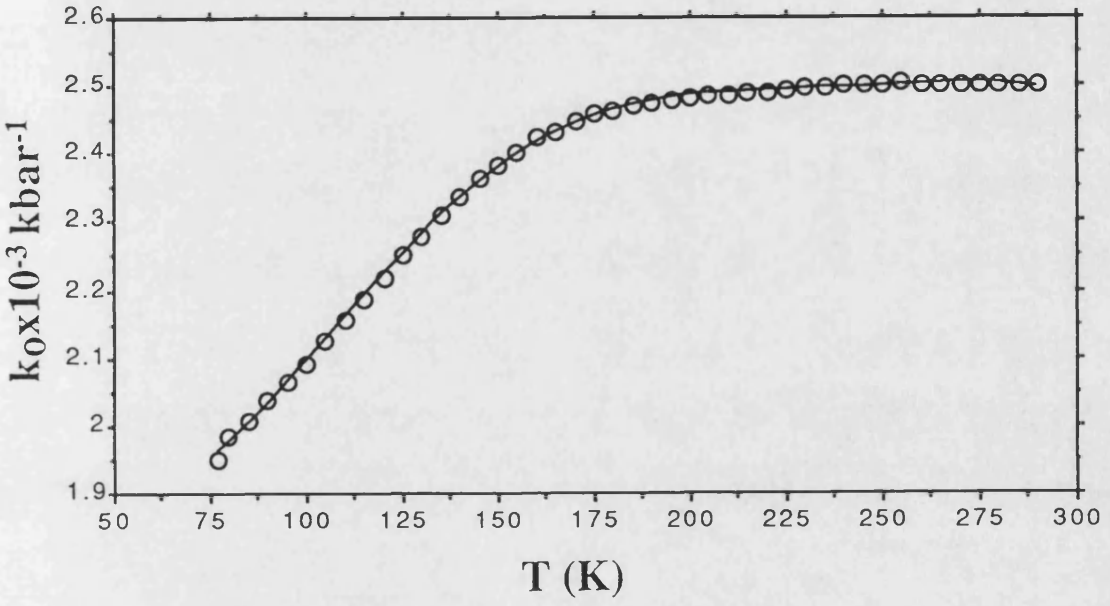

Figure 4.5 : Pressure coefficient of manganin as a function of temperature.

4.6 Conclusion

In the series of experiments described here we have calibrated manganin wire gauges. The wire is suitable and reliable as a secondary pressure gauge provided it has been seasoned and aged properly. In our experiments we found that the temperature coefficient of manganin is described by

$$R(T,0) = R_0 + 0.111T - 2.696\times10^{-4}T^2 - 2.075\times10^{-8}T^3 + 5.502\times10^{-10}T^4 \text{ ohm}$$

This temperature coefficient proved to be stable after the wire had been seasoned and pressure cycled beyond its maximum limit.

We calculated the pressure coefficients of manganin at 300 K and 77 K to be $(2.45 \pm 0.02)\times10^{-3}$/kbar and $(1.98 \pm 0.02)\times10^{-3}$/kbar respectively. These pressure coefficients are slightly different from those reported by other workers (Becker *et al.* (1976), Peggs (1983), Thompson (1984)). The temperature dependence of the pressure coefficient is described by :-

$$k_0 = (1.3005 + 1.0666\times10^{-2}T - 2.277\times10^{-5}T^2)\times10^{-3} \text{ /kbar}$$

With a 1:1 mixture of petrol and transformer oil as the pressure transmitting medium, we find that the pressure in the cell decreases by 3.98 kbar as it cools from 300 K to 77 K. This effect is primarily due to the contraction of the pressure transmitting medium. We believe that this is the first time that the temperature dependence of the pressure coefficient of manganin has been completely measured.

CHAPTER 5

Samples Details and Experimental Techniques

5.1 Samples Structures

5.1.1 Single Barrier GaAs/AlAs Diodes

Two single barrier samples (labelled DB1220 and EPI20291/5B) have been investigated. Sample DB1220 was grown by MBE on an n^+-substrate at the Cavendish Laboratory, University of Cambridge. The epitaxial layers were deposited in the following order: (i) 500nm n^+–GaAs; (ii) 40nm n–GaAs; (iii) 200nm nominally undoped GaAs; (iv) 4.0nm AlAs (undoped); (v) 5–10nm GaAs; (vi)+(vii) reverse of (i) and (ii) (see Fig. 5.1). Table 5.1 below gives details of the doping density of each layer. The AlAs thickness was accurately determined from TEM measurements and the doping profile established using SIMS.

The specifications of sample EPI20291/5B which was grown by MOCVD are similar to sample DB1220 except for the barrier thickness which lies between

1.25 – 1.75nm. Square mesas with sides of length 50 – 160μm were defined with AuGe/Ni ohmic contacts on 3 x 5mm^2 chips. The data reported in this work relate to the 80μm mesa contacts.

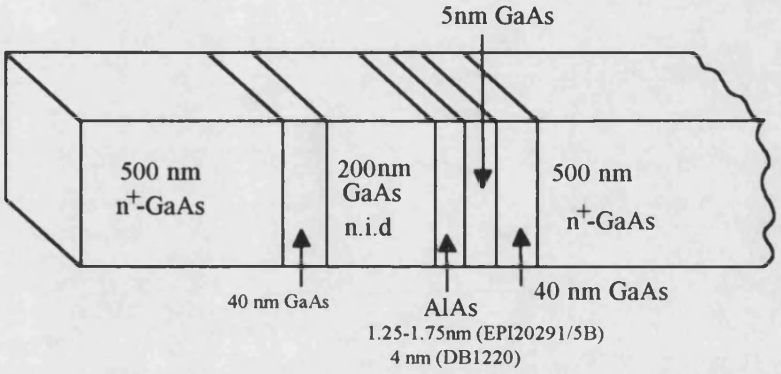

Figure 5.1: Details of samples DB1220 and EPI20291/5B – single barrier GaAs/AlAs diodes.

Layer	Thickness (nm)	Material	Doping(cm^{-3})
i	500	GaAs	3 x 10^{18}
ii	40	GaAs	1 x 10^{17}
iii	200	GaAs	n.i.d
iv	4.0(MBE)/1.25–1.75(MOCVD)	AlAs	n.i.d
v	5	GaAs	n.i.d
vi	40	GaAs	1 x 10^{17}
vii	500	GaAs	3 x 10^{18}

Table 5.1 Layer thickness and doping density for samples DB1220 & EPI20291/5B

5.1.2 Sample B1 (Double Barrier Resonant TunnellingDiode)

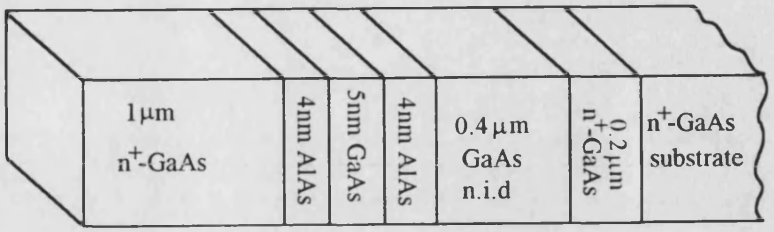

Figure 5.2 : Details of sample B1 – Double barrier resonant tunnelling diode.

Figure 5.2 shows a schematic diagram of the sample B1. It was grown by MBE at the Max-Planck Institut FKF, Stuttgart, Germany. A 0.2μm highly doped GaAs buffer was grown first on an n^+–GaAs substrate. This was then followed by a 0.4μm *n*-GaAs (nominally undoped) layer and an AlAs(4nm)/GaAs(5nm)/ AlAs(4nm) double barrier structure. Subsequently a 0.75μm n^+–GaAs electrode layer ($2x10^{18}cm^{-3}$ doped) was grown and the sequence terminated with a very highly doped region of n^+–GaAs to facilitate ohmic contact formation. Layer thicknesses were accurately established by measuring RHEED oscillations during growth and from X-ray diffraction measurements on reference superlattice structures. Samples with dimensions of 5 x 5 mm^2 were cleaved from the wafer, AuGe/Ni ohmic contacts were formed and 50μm diameter round mesas defined using conventional wet–etch technology.

5.1.3 Sample Contacting

The completed chips were cleaned for 5 minutes with acetone in an ultrasonic bath and in boiling iso-propanol for 5 minutes before they were fixed to Al_2O_3 chip carriers with conducting silver epoxy resin. Mesas were contacted to

gold pads on the chip carriers with 12.5μm diameter gold wires using an ultrasonic wire bonder. Large diameter Cu wires were then soldered to the gold pads in order to perform measurements.

5.2 Experimental Techniques

5.2.1 Constant–Voltage Measurement System

A schematic diagram of the constant–voltage measurement system is shown in Fig. 5.3. It is designed to measure both current (I) and conductivity (dI/dV) for a given voltage across a two terminal diode.

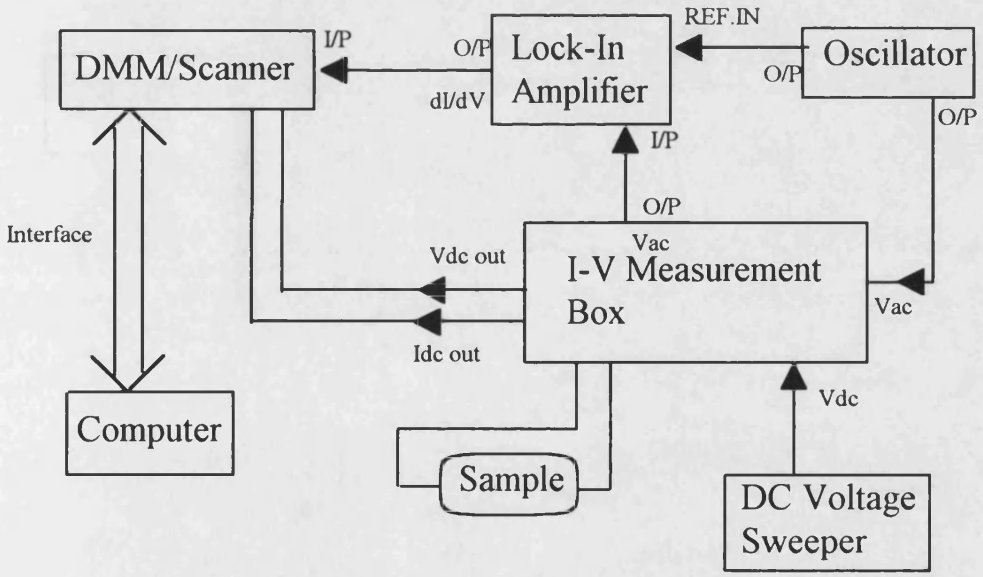

Figure 5.3: Block diagram of current–voltage measurement set–up.

Current-voltage characteristics are recorded by measuring the current flowing through the structure over a preset bias range using a Keithley 199 DMM/Scanner. The voltage sweep is supplied by a DC voltage ramp which feeds one of the inputs of a voltage adder. The constant voltage source is necessary to prevent the sweeper voltage falling when the finite resistance sample is connected due to its non zero output impedance. The source is essentially a voltage follower with a very high input impedance operational amplifier. The circuit reproduces the sweeper voltage across the sample while presenting a high input impedance to the sweeper (see Fig. 5.4).

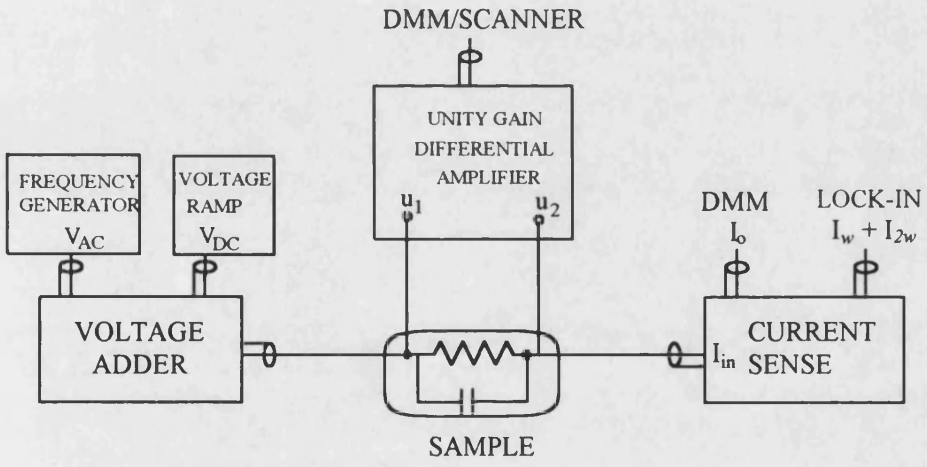

Figure 5.4: Block diagram of sample connections.

Conductivity (dI/dV) measurements may also be made using an EG&G Model 5210 lock–in amplifier. The sample voltage signal is modulated with a 1mV RMS AC signal from a high stability Krohn–Hite model 4400A oscillator at 370 Hz. The lock–in yields the analogue derivative proportional to dI/dV which then forms another input to the DMM and is recorded by a computer.

The AC modulation voltage and the DC sweeper voltage are fed to two separate voltage followers (Part A of Fig. 5.5) and their sum is reproduced at the output of the noninverting adder (Part B of Fig. 5.5). The true DC voltage across the sample is then measured by the unity gain differential amplifier (Fig. 5.6) which outputs the voltage to the DMM.

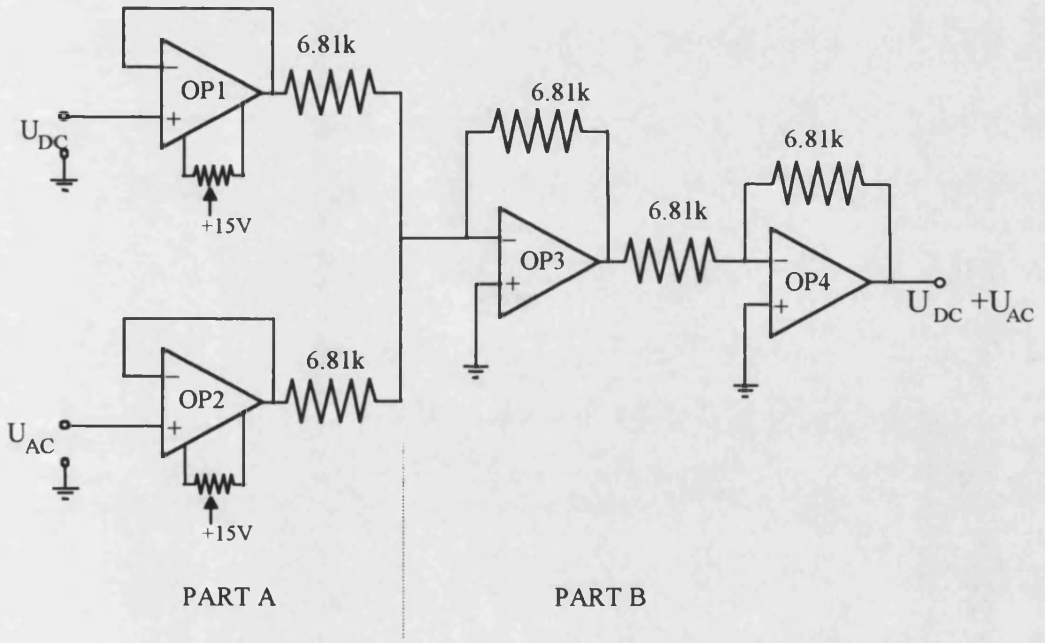

Figure 5.5: Voltage Adder circuit diagram

The current flowing in the sample is measured by a current sense circuit connected in series with one of the leads as shown in Fig. 5.7. The first part of the current sense circuit (Part A of Fig. 5.7) amplifies the AC current with gain which is controlled by resistance R_1. The DC current amplification is controlled by resistance R_0 (Part B of Fig. 5.7). The variable capacitor C_0 blocks a DC feedback current at OP3. The sweeper voltage, current and conductance are measured on the multichannel DMM and recorded by a controlling personal computer.

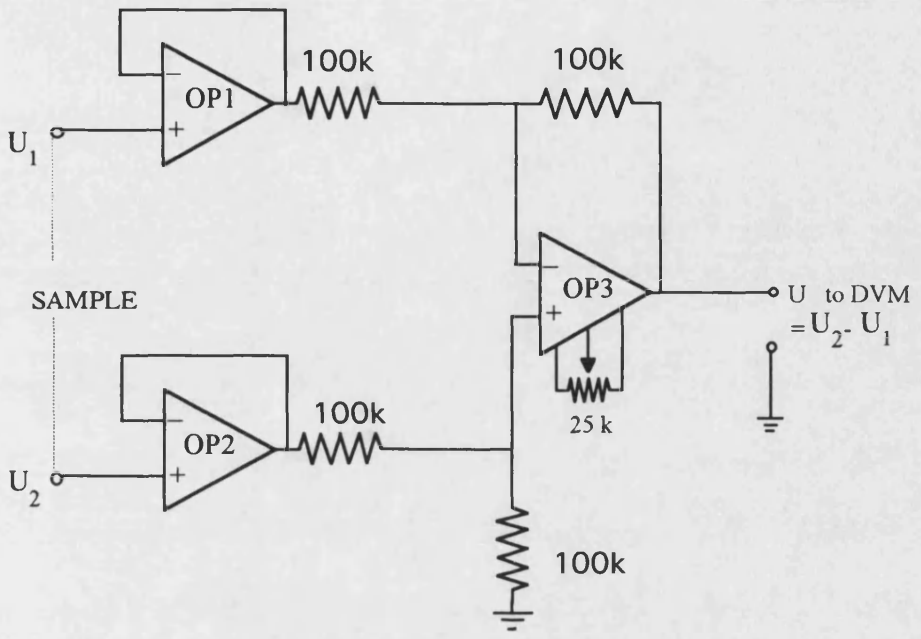

Figure 5.6: Circuit diagram of a unity gain differential amplifier

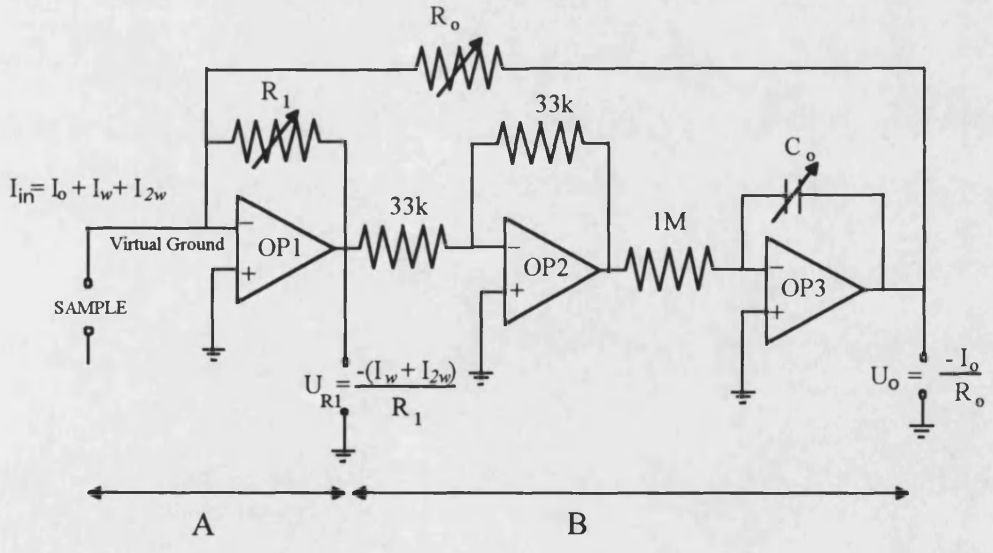

Figure 5.7: Current sense circuit diagram

5.2.2 Closed Cycle Cryostat

Measurements are made at atmospheric pressure in a Cryophysics closed cycle cryostat at room temperature, 77K and ~8K. To achieve thermal isolation the cryostat is pumped down to a pressure ~ $4x10^{-4}$ mbar before cool down. Temperature measurement was achieved using a Silicon diode which had been calibrated between 3.2 – 330 K and was controlled by a Lakeshore DRC–91CA temperature controller.

5.2.3 Hydrostatic Pressure Experimental Techniques

Hydrostatic pressure was applied at room temperature in a Unipress liquid pressure cell using either a mixture of 1:1 petroleum:transformer oil or petroleum ether as transmitting medium. Pressure in the cell was determined with a calibrated manganin pressure gauge. The resistance of the manganin gauge was measured using a four probe technique with 1mA DC. In order to cool down to 77 K the entire pressure cell was slowly immersed in a liquid nitrogen bath. A full description of the pressure system is given in Chapter 4. The temperature is measured *in situ* using either a copper–constantan thermocouple or a platinum resistance thermometer.

In our calculations of the various subband energies we have used the conduction band offsets and effective masses as given in Chapter 4. We neglect a small pressure dependence of the effective mass as well as the compression of the tunnel barriers and well which we estimate to be less than 2%. In practise our observations could be described solely in terms of the longitudinal X–minima in the transport direction and X–point subband energies were calculated using the heavy longitudinal mass m^*_{Xl}. These subbands lie at lower energies than corresponding

ones confined at the transverse X–minima and, as the pressure is increased, are always the first to fall below the Fermi energy (E_F) of the adjacent electrode and become occupied. We do not, however, rule out the possibility that the transverse X–minima could be playing an important role in view of the much higher density of states of the associated subbands.

CHAPTER 6

Single Barrier GaAs/AlAs/GaAs Structures

6.1 Experimental Results

Two different single barrier structures have been studied at hydrostatic pressures up to ~8 kbar. The specifications of both MBE (DB1220) and MOCVD (EPI20291/5B) structures are explained in detail in Chapter 5. Figure 6.1 shows the structure of these samples at zero bias where the long nominally undoped region is the emitter contact and the short one is the collector contact. Due to the asymmetrical doping, a 2D accumulation layer is formed at the emitter/barrier interface under forward bias (emitter negative) while in reverse bias most of the applied voltage falls across the long undoped region. In the sample DB1220 resonances due to X–point subbands in the barrier layer have been observed in forward bias under high pressure while in the sample EPI20291/5B no resonances were observed either in the current or conductance measurements.

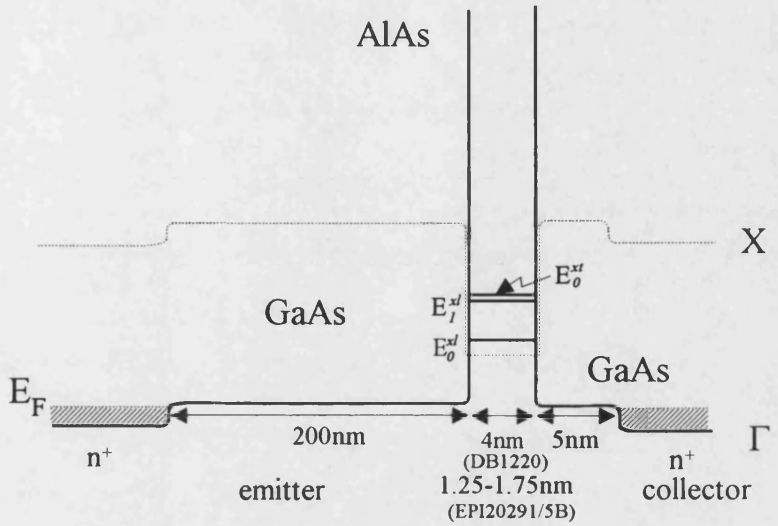

Figure 6.1 : A sketch of sample DB1220 or EPI20291/5B at zero bias

6.1.1 MBE Sample DB1220

Figure 6.2 depicts the potential profile of this device under forward bias where part of the voltage drops across the accumulation and depletion layers. The asymmetry of the current–voltage (I–V) characteristic under forward and reverse bias can be seen in the measurement at 8 K (p = 1bar) as shown in Fig. 6.3. In forward bias the current increases rapidly with increasing bias while in reverse bias the current remains small over the entire measurement range. For example at ±1 V, the reverse bias current is about one order of magnitude smaller than the forward bias current. There is no sign of resonances either in reverse or forward bias at this temperature and pressure and it can be concluded that currents are dominated by the Γ barrier profile.

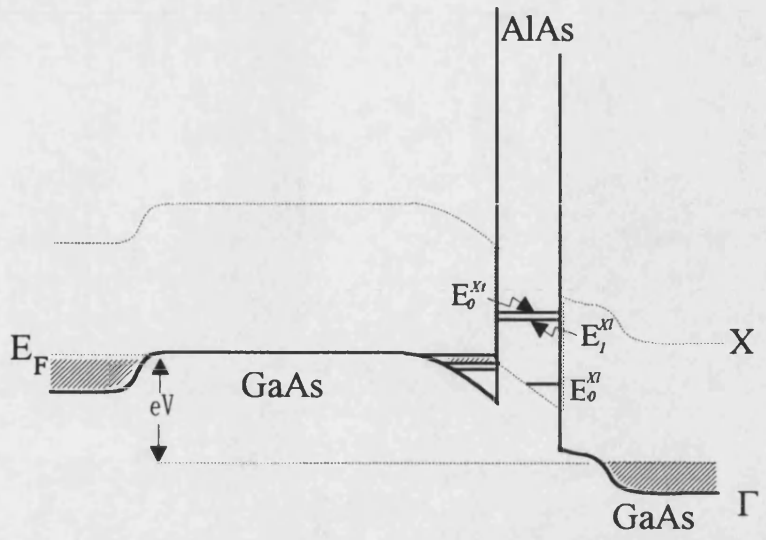

Figure 6.2 : Potential profile of sample DB1220 under forward bias.

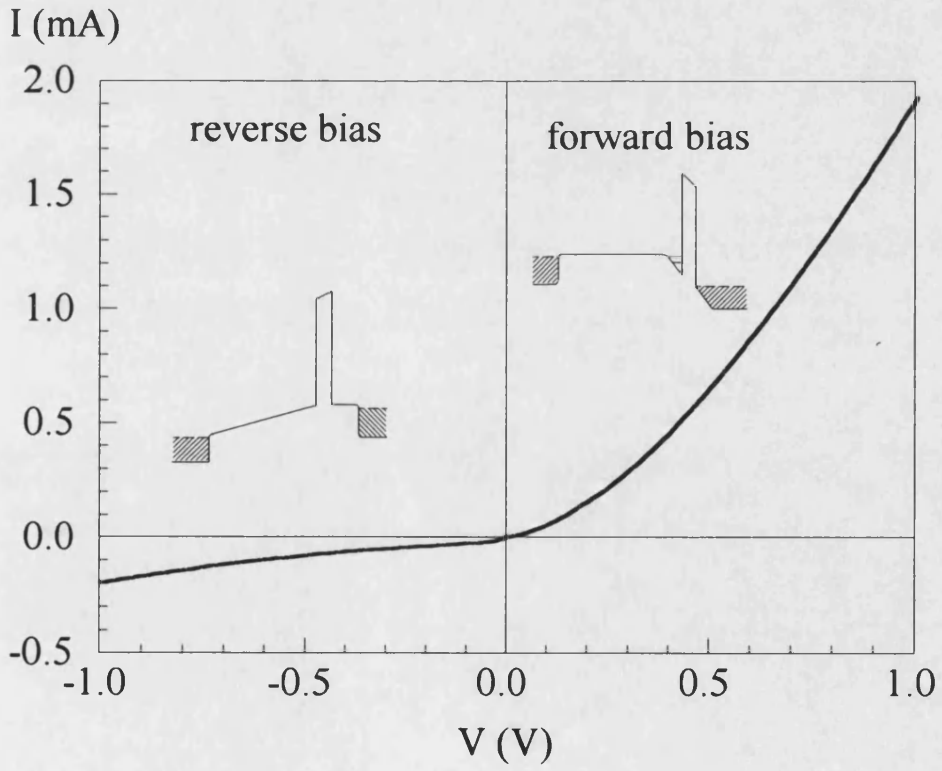

Figure 6.3 : I–V characteristic of sample DB1220 at 8 K and 1 bar.

Asymmetric I–V curves are also observed at 300 K under a range of different hydrostatic pressures as shown in Fig. 6.4. For a given bias voltage the current increases steadily as the hydrostatic pressure increases. The contribution due to a thermionic emission current is quite large at 300 K and the reverse bias current at 1 V and 300 K is about ten times higher than that at 8 K. As a consequence tunnelling current due to either Γ or X electrons is buried in this thermionic one and peaks (if any) in the tunnel current are not observable. However, a plot of dI/dV in Fig. 6.5 reveals a shoulder structure near +0.1V in forward bias emerging at the highest pressure. If we assume the Γ(GaAs)-X(AlAs) conduction band offset at 300 K is about 0.16 eV and under hydrostatic pressure it is reduced by about 12meV $kbar^{-1}$, at p ≅ 10.7 kbar we should expect $E_0^{X\prime}$ to fall below the Fermi level of the emitter near V ≅ +0.1 V.

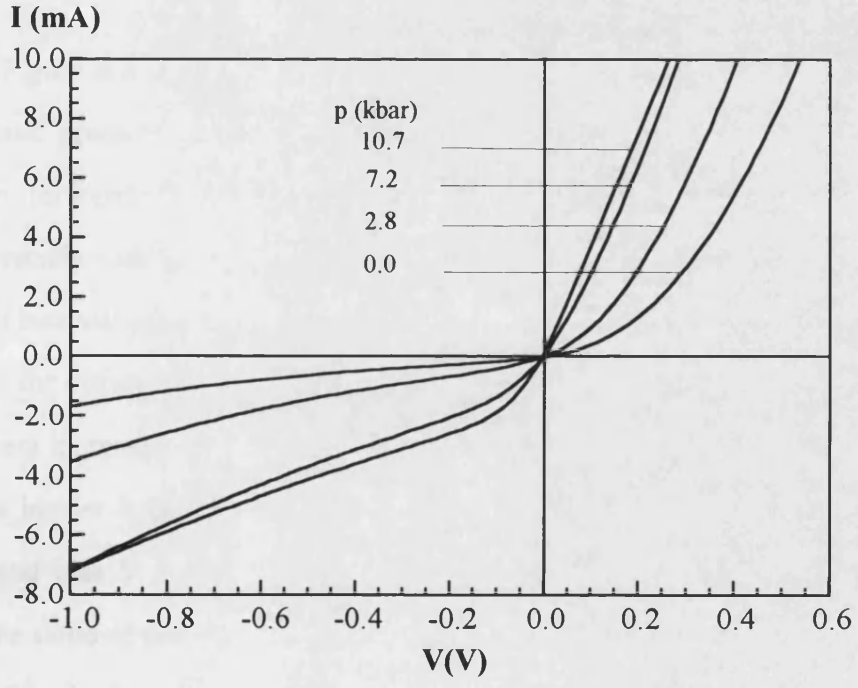

Figure 6.4 : I–V characteristic of sample DB1220 at 300 K and pressure up to 10.7 kbar.

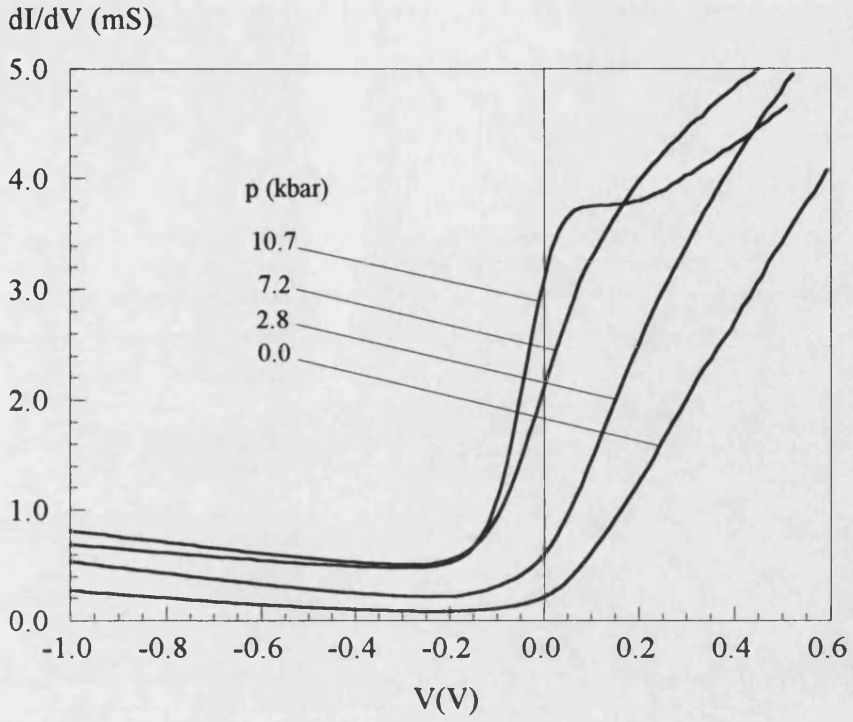

Figure 6.5 : dI/dV of sample DB1220 at 300 K and pressure up to 10.7 kbar.

Figure 6.6 shows a set of current–voltage characteristics under increasing hydrostatic pressure at 77 K. No obvious resonance effects are visible in this I–V plot. In forward bias, the current at a given voltage increases rapidly and monotonically with pressure while the reverse bias current remains small for a wide range of bias voltages and pressures. A plot of the logarithm of the current against pressure for different values of forward bias in Fig. 6.7 shows that at low voltages, the current increases exponentially with increasing pressure due to a decrease in the X–point barrier height. The current is almost constant at pressures greater than 7 kbar and bias V > 0.5 V indicating that the X–point barrier almost disappears here. The slope of the plot at +0.4 V and $0 < p < 5$ kbar is about 0.5 $kbar^{-1}$. This is smaller than in data due to Mendez *et al.* (1986) and Rossmanith *et al.* (1993) in different structures where they measure 2.09 and 2.0 $kbar^{-1}$ respectively.

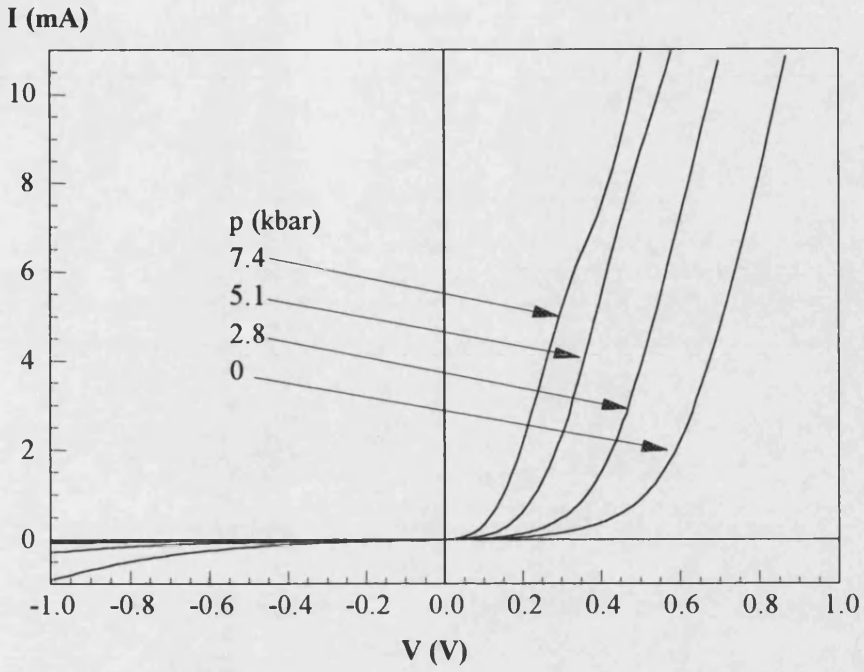

Figure 6.6 : I–V characteristics of sample DB1220 at 77 K and various pressures.

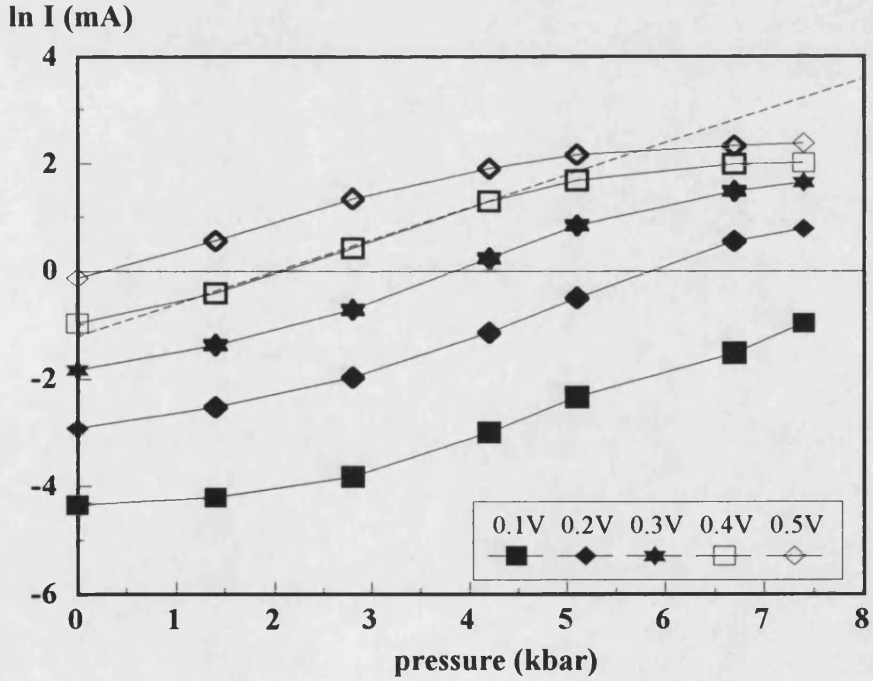

Figure 6.7 : Plot of log I versus applied pressure at 77 K for a range of bias voltage

However, putting this slope and bias values into the equation below (Mendez *et al.* (1986))

$$\frac{d\,lnI}{dp} = -0.685\frac{m^{*1/2}\,V_B^{3/2}}{V}w\left[\frac{1}{2}\frac{d(\ln m^*)}{dp}+\frac{3}{2}\frac{d(\ln V_B)}{dp}\right]$$

where V_B is the effective barrier height (in eV), V is the voltage drop across the barrier (in V) and w is the barrier width in Å. With a barrier width w = 40 Å, and using parameters from Table 3.3 in Chapter 3 where for the longitudinal X–minimum, the barrier height $V_B \cong 0.16$ eV, $dV_B/dp \cong -0.012$eV/kbar, yields the value of $d(ln m^*)/dp \cong 0.75\%$ /kbar. On the other hand for the transverse X–minima $d(ln m^*)/dp$ is calculated to be ~ –29.8% /kbar which is unphysically large. The same equation with $V_B \cong 1$ eV, $dV_B/dp \cong 1.3$ meV/kbar would imply $d(ln m^*)/dp \cong -3.8\%$ /kbar for tunnelling via the Γ barrier. From simple considerations we would expect an increase in effective mass with pressure indicating that X_l tunnelling is probably dominating.

Measurement of the second derivative of the current (d^2I/dV^2) reveals a series of oscillations at small forward bias voltages (< 0.2 V) at 77 K (Fig. 6.8) which are more pronounced at 8 K. These oscillations do not shift with applied pressure and can be attributed to the successive occupation of subbands in the accumulation layer, confirming its existence at the emitter/barrier interface. Figure 6.2 shows the position of these subbands in the accumulation layer along with the quasi–bound states in the barrier associated with the X–point profile. Since the 2D states in the accumulation layer are determined by the Γ–Γ conduction band offset, an increase in pressure does not alter their energies relative to the conduction band edge. These low bias oscillations begin to disappear into the increasingly non–linear background at pressures greater than 3 kbar.

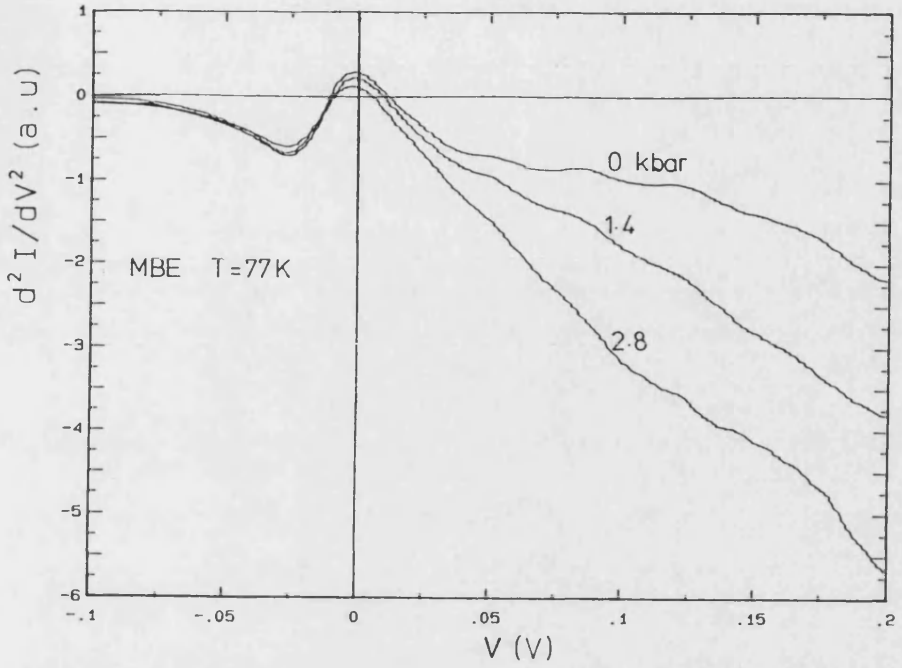

Figure 6.8 : Low bias second derivative at 77 K and various pressures.

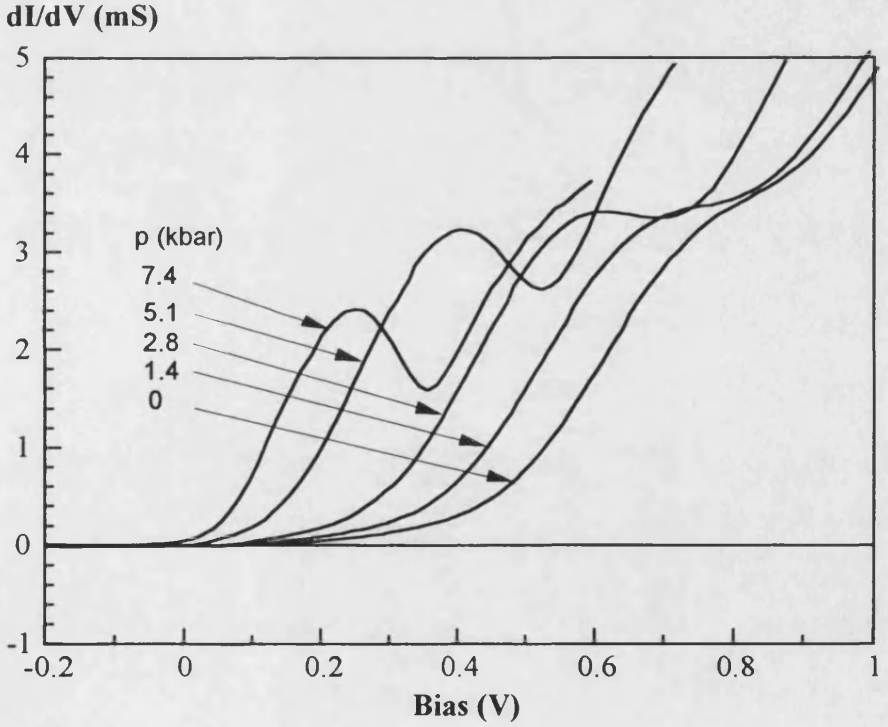

Figure 6.9 : The conductance of sample DB1220 at 77 K and various applied pressures.

The conductance (dI/dV) for this structure is plotted in Fig. 6.9 at various applied pressures showing that a pronounced peak structure appears in forward bias at pressures above 2 kbar. A shoulder structure also appears in the log plot of current density versus voltage at p ~ 6.7 kbar (scaled by a factor of 10^4) detailed in Fig. 6.10 along with the calculated trace.

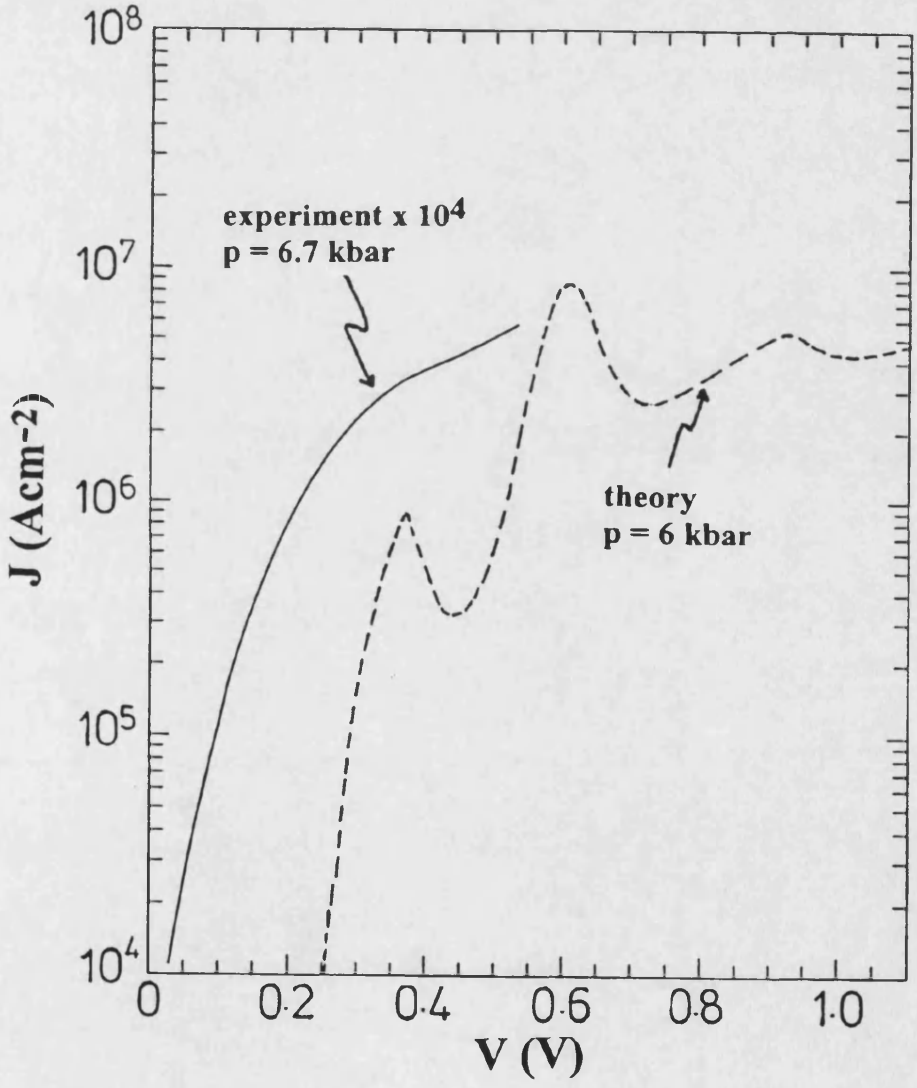

Figure 6.10 : Experimental and theoretical I–V characteristics of sample DB1220 at 77 K and a pressure near 6 kbar.

Figure 6.11 shows a plot of the voltages at the peaks and valleys of dI/dV plotted against applied pressure. Note that these voltages depend almost linearly on pressure. A linear extrapolation of the peak voltage to zero yields an intercept of 10.6 kbar on the x–axis. At this pressure the Γ(GaAs)–X(AlAs) offset has been reduced to $0.160-0.012\times10.6 \cong 0.03$ eV i.e. almost to zero. Hence we can confidently attribute the peaks to quasi–resonances between occupied Γ–point subbands in the accumulation layer and unoccupied X–point subbands in the barrier (Fig. 6.2).

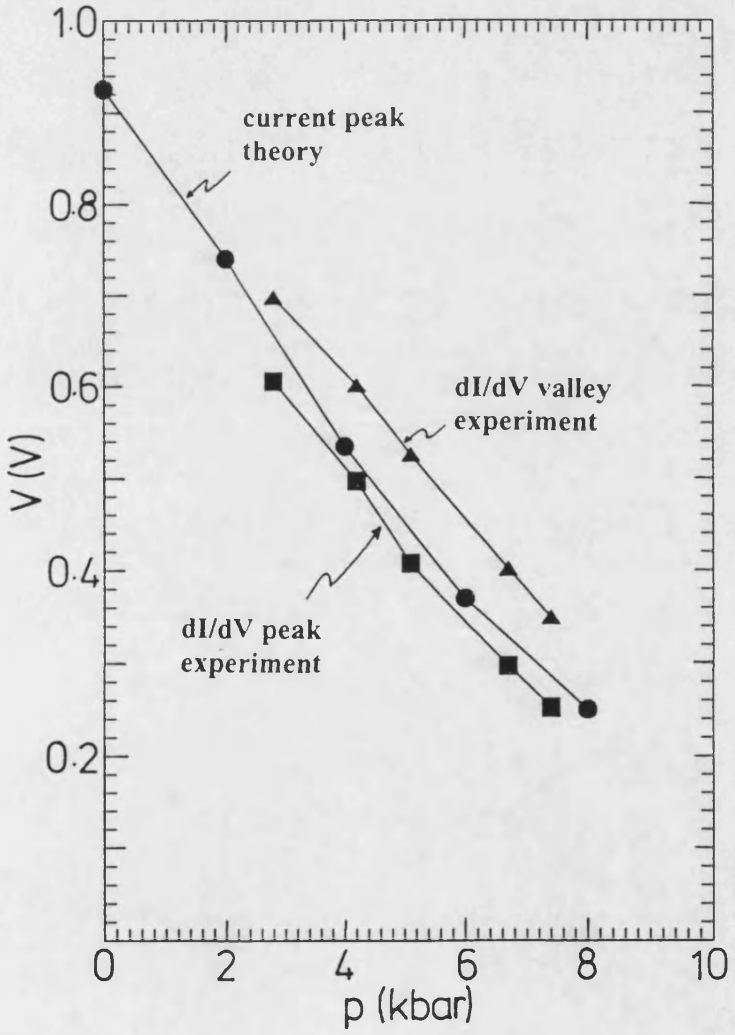

Figure 6.11 : Experimental and theoretical peak and valley position versus pressure of sample DB1220 at 77 K

6.1.2 MOCVD Sample EPI20291/5B

The designed conduction band profile for this structure is almost identical to sample DB1220 (see Fig. 6.1) except for the barrier thickness which lies in the range 1.25 – 1.75 nm. Therefore in forward bias almost all of the voltage drop is across the accumulation and depletion layers. Fig. 6.12 shows I-V characteristics at three different temperatures along with dI/dV-V plots at the bottom. As was the case for DB1220, this sample also shows an asymmetric I–V characteristic due to its asymmetrically doped electrodes. The dI/dV-V plot shows no peak in both bias directions.

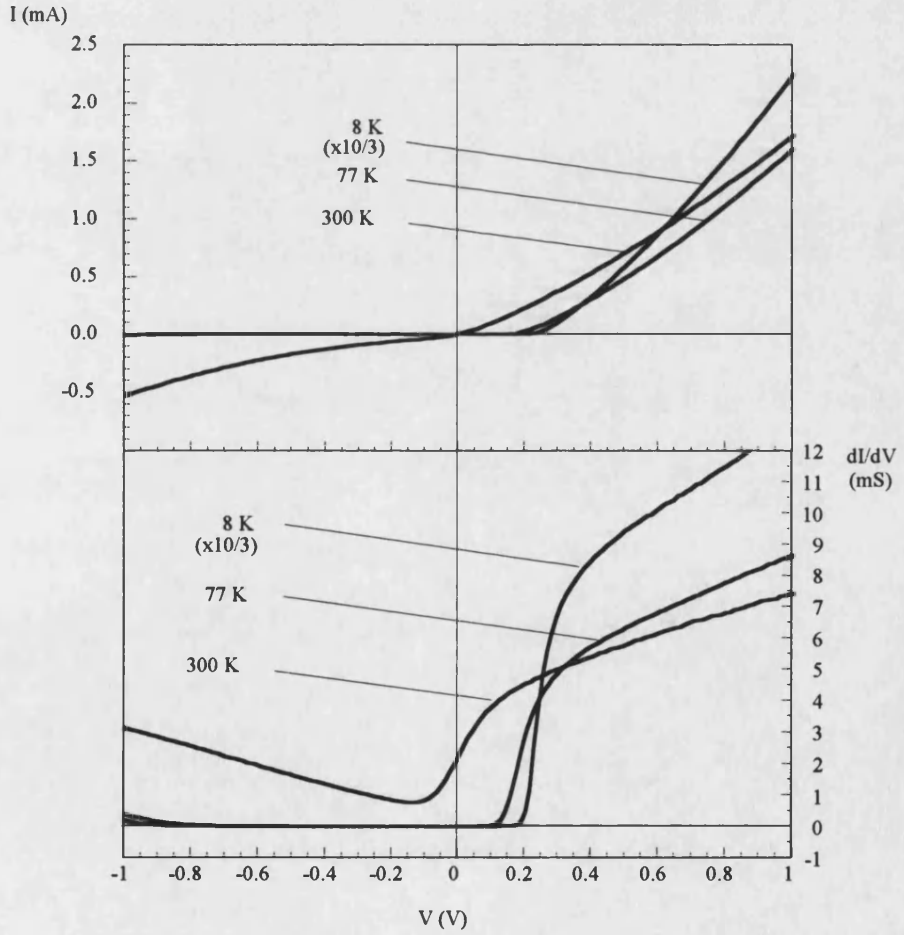

Figure 6.12 : I–V and dI/dV-V characteristics of sample EPI20291/5B at different temperatures.

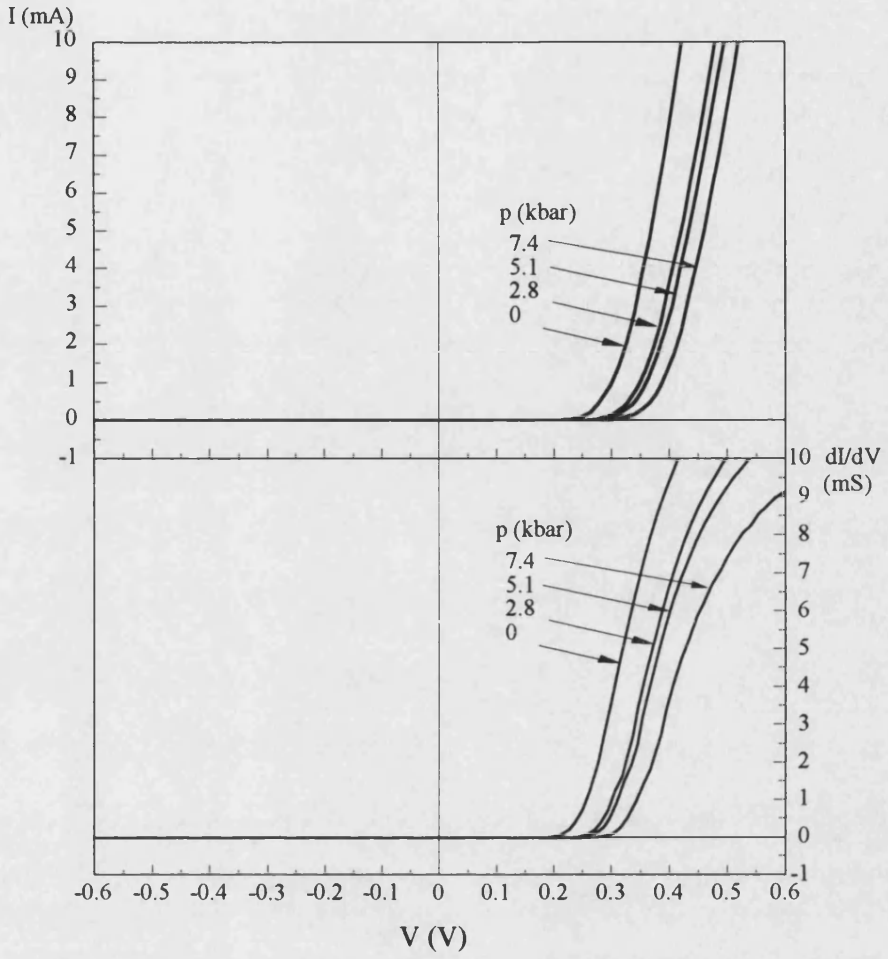

Figure 6.13 : I–V and dI/dV-V characteristics of sample EPI20291/5B at 77 K and different applied pressures.

Figure 6.13 shows I–V and dI/dV-V characteristics for this sample at 77 K under various applied pressures. At a given pressure the current rises rapidly with increasing forward bias voltage > 200 mV. Surprisingly, however, as the pressure increases the current at a given bias voltage falls in stark contrast to sample DB1220. In reverse bias, the current is almost zero over a wide range of voltages and at all pressures. This asymmetric relationship in forward and reverse bias can also be seen in the dI/dV-V plots. In contrast to the MBE sample this MOCVD sample does not show any peak in dI/dV under forward or reverse bias in the temperature range 77 – 300 K and at higher pressures. Oscillations at low forward

biases due to electrons occupying subbands in the accumulation layer are also not observable here.

6.2 Discussion

6.2.1 Sample DB1220

Tunnelling via X–point AlAs potential barriers has been established by Mendez *et al.* (1986,87,88 &89), Othaman *et al.*(1991), and Austing and co–workers (1989,90) in double barrier structures. A thermionic emission measurement by Pritchard *et al.* (1989,90) yields a barrier height of 0.15 eV which is about the same as the theoretical X(AlAs) – Γ(GaAs) band offset. In our measurement the increase in current with increasing pressure for sample DB1220 at 77 K also indicates that the X–minima play an important role in the transport. This effect can also be seen in the measurement at 300 K. Similar findings have been found on single barrier structures by many other workers such as Landheer *et al.* (1989), Rossmanith *et al.* (1993), Hase *et al.* (1986) and Rousseau *et al.* (1989). Landheer *et al.* (1989) have calculated the I–V characteristics of single barrier structures employing a simple effective mass model. Their results agree quite well with their measurements for MBE grown GaAs/AlAs structures at ambient pressure when the barrier thickness is greater than 4 nm. Rossmanith *et al.* (1993) also conclude that electrons tunnel via the X–point barrier in single barrier GaAs/$Al_xGa_{1-x}As$ structures when the aluminium content $x > 0.4$. A much thicker barrier 10 – 30 nm has been used by Hase *et al.* (1986) who arrived at the same conclusion. However, these measurements do not conclusively determine which X–minimum is the major contributor to the tunnelling current.

The quasi-bound states due to X–point minima in the AlAs barrier for this structure are calculated employing a simple finite well theory. Using values of $m^*_{Xl} = 1.1m_0$, $m^*_{Xt} = 0.19m_0$, X(GaAs)–X(AlAs) $\cong$ 0.35 eV, and an AlAs barrier width of 40 Å the first (E_0^{Xl}) and second (E_1^{Xl}) quasi–bound states of longitudinal X–minima in the AlAs are calculated to be about 15.9 meV and 63.3 meV from the AlAs X–point minima respectively. For the transverse X–minima the first quasi–bound states of (E_0^{Xt}) with the lower effective mass is at about 64 meV which is already slightly higher than (E_1^{Xl}). The positions of these energy levels are shown in Fig. 6.1.

If we assume that the peaks in the conductance arise due to quasi-resonances between the 2D subbands within the accumulation layer and the first X–point quasi-bound states in the barrier we should expect the peak voltage to shift linearly towards lower voltages as pressure increases as shown in Fig. 6.9 and 6.11. In order to be more specific about the assignment of these peaks in the conductance, the I–V characteristics of the structure were also calculated theoretically by R.T.Syme at the Cavendish Laboratory, Department of Physics, University of Cambridge. The potential profile in the region of the accumulation layer and barrier is obtained from self-consistent solutions of Poisson's and Schrödinger's equations. A detailed explanation of this self-consistent method is given in Appendix A. For all pressures the Γ–Γ conduction band offset (~1 eV) was used at the heterointerfaces to obtain the self-consistent potential profile. An example of the calculated X_l current along with the experimental current (scaled by a factor of 10^4) is shown in Fig. 6.10 for a pressure of around 6 kbar.

It is clear from Fig. 6.10 that the first peak (first resonance) in the calculated X_l current coincides with a weak feature in the experimental current (i.e. the peak/valley region in the conductance). The second and third peaks in the

theoretical curve corresponds to resonances associated with higher X-point subbands which are found at substantially higher voltages. The pressure dependence of the first peak or quasi–resonance in the calculated current is plotted in Fig. 6.11, along with the experimental positions of the peak and valley in the conductance. We can only observe quasi–resonances in this single barrier structure because the two subbands in the Γ–valley accumulation layer and in the X–point quantum well in the barrier have different effective masses and their regions of k–space do not truly nest. This situation is depicted in Fig. 6.13. Despite the total absence of fitting parameters, the theoretical quasi–resonance always falls between the peak and valley in the measured conductance, as expected. The experimental feature is much weaker than calculated because (i) the total current also contains contributions from tunnelling via Γ and X_t, and (ii) carrier scattering and spatial inhomogeneities tend to smear out the peak anyway. Note that quasi–resonances due to X_t states are very much weaker, occur at substantially higher biases and are much broader, because of the smaller X_t effective mass. The calculated value of $d(ln m^*)/dp$ from the measured slope of log(I) versus pressure above also supports tunnelling via longitudinal X–minimum in the barrier layer. In addition the calculation of the bias voltage required for quasi–resonant tunnelling between the 2D subbands in the accumulation layer and first quasi X_t–bound state in the well agrees excellently with the experimental value.

So far we have assumed a value of −12 meV/kbar for the rate of change of the Γ–X conduction band offset with pressure. We can also make this quantity a fitting parameter, and on doing this we obtain a value of (−11.3±1) meV/kbar, in agreement with the quoted value of Mendez *et al.* (1990) within experimental error. A calculation by Rousseau *et al.* (1989) shows that it is possible to see NDR in a single barrier structure via X–confined states. Beresford *et al.* (1989) observe

NDR in a GaAs/AlAs/GaAs structure with a 4 nm barrier width at atmospheric pressure. They also attribute this NDR due to quasi–bound states associated with the X–point profile.

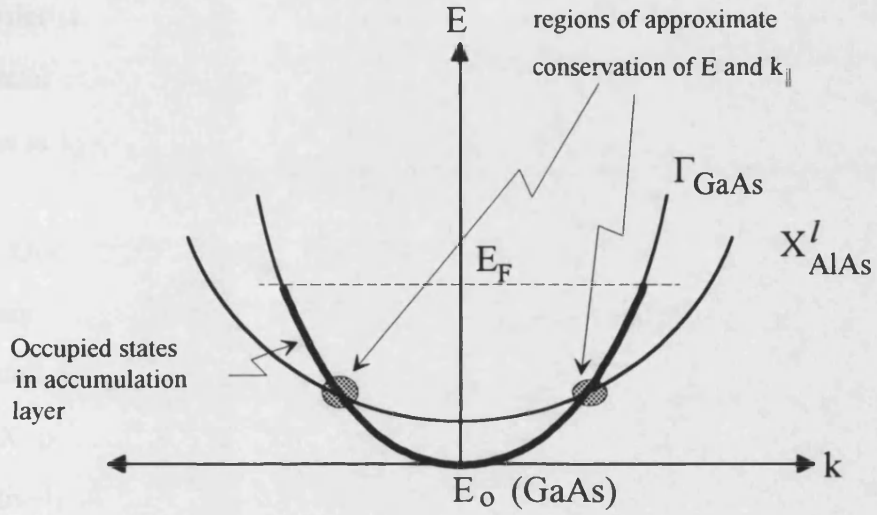

Figure 6.13 : Dispersion curves for Γ(GaAs) and X(AlAs)

6.2.2 Sample EPI20291/5B

In stark contrast to measurements on the MBE sample we observe a decrease in current with pressure in the MOCVD sample. This suggests that in this sample X–point minima do not play an important role in tunnelling. An increase in the resistance with pressure is an effect we have observed before in structures with direct AlGaAs barriers. The same effect has been observed by Austing *et al.* (1990) but on double barrier AlGaAs/GaAs/AlGaAs structures for pressures up to about 18 kbar. In these devices Γ–point tunnelling is the main contributor to the current. These authors attribute this anomaly to the presence of deep impurity levels within the AlGaAs barriers since it is known that the Γ–Γ barrier stays relatively constant upon increasing pressure. The changes may be due to a pressure–induced increase

in effective mass of the barrier or electrodes . We would normally expect X–point related effects to be important in these MOCVD AlAs barriers and speculate that their absence is due to the much thinner barrier (Γ tunnel currents dominate) and considerable inter–diffusion at the interfaces of MOCVD structures on a scale of the barrier thickness. We also cannot rule out the possibility of the existence of a substantial series resistance due to problems during fabrication of the sample. An increase in hydrostatic pressure might lead to an increase in this series resistance.

One of the major problems with this sample is the uncertainty in the barrier thickness. For a 17 Å barrier the subbands energies in the barrier layer are calculated to be at ~62 meV for E^X_0 and ~173 meV for E^X_0. with respect to the AlAs X–point minima. These energies are raised to ~98 meV and ~226 meV respectively if the barrier width is reduced to only ~12 Å. Therefore within this thin barrier range even a monolayer uncertainty in the barrier thickness makes a substantial difference in the subband energies as explained by Bonnefoi *et al.* (1988). High energy subbands usually require a quite substantial bias to bring them into resonance. Landheer *et al.* (1989) observe that for thin barrier structures (< 3 nm) the Γ–point barrier dominates in the tunnelling process. This is supported by Kyono *et al.* (1989). They observe tunnelling via the AlAs Γ–point for very thin (~14.2 Å) barrier MBE samples. For structures with barrier thickness greater than 40 Å they observe tunnelling via the AlAs X–point. However, their results are only for samples at atmospheric pressure.

The dominance of Γ currents in thin barrier structures can partly be explained by Fowler–Nordheim tunnelling where the barrier transparency is given by (Mendez *et al.* (1988))

$$D(E_x) = A \exp\left(-\frac{4}{3}\left(\frac{2m^*_\Gamma}{\hbar^2}\right)^{1/2} \frac{w.(E_\Gamma - E)^{3/2}}{eV}\right) + B \exp\left(-\frac{4}{3}\left(\frac{2m^*_X}{\hbar^2}\right)^{1/2} \frac{w.(E_x - E)^{3/2}}{eV}\right)$$

where the constant B which includes a coupling constant is a lot smaller than A. For an AlAs barrier, $m^*_\Gamma \sim m^*_{Xl}$ and $E_\Gamma >> E_X$. In this case when the barrier width $w \rightarrow 0$ the first term in above equation dominates and Γ–X tunnelling become less important in spite of its smaller barrier height (Mendez *et al.* (1988)).

6.3 Conclusion

In conclusion we have measured the forward and reverse bias characteristics of asymmetrically doped single barrier GaAs/AlAs/GaAs diodes grown by MBE and MOCVD. In the MBE structures the formation of a 2D accumulation layer at the emitter/barrier interface under forward bias is observed. An observed increase in current with hydrostatic pressure can be attributed to tunnelling involving the X–point minima. In the differential conductance measurements at pressures above 2 kbar at 77 K we observed a pronounced peak structure in forward bias. The voltage at the peak shifts linearly downwards in voltage with applied pressure and a comparison with self–consistent theoretical calculations indicates that the peak arises due to quasi–resonances between occupied Γ–point 2D subbands in the accumulation layer and unoccupied longitudinal X–point subbands in the barrier. At room temperature we find that the current density at a given voltage increases as soon as the pressure is raised above 1 bar. Hence we conclude that at ambient pressure and temperature the X–minima play an important role in the transport. Since the X–point current is certain to be thermally activated at room temperature this is likely to be the dominant

contribution to the temperature coefficient of devices (e.g. detectors and mixers) based on structures of this type. Hence device optimisation must involve minimising the role played by X–point channels by using thinner barriers, lower temperatures, or a different material system.

In contrast in an MOCVD sample we have observed a decrease of current with increasing pressure and there is no peak structure in the dI/dV. Although this suggests that the tunnelling current is dominated by the Γ–point barrier rather than the X–point, these phenomena are not fully understood. The reduction in current may be due to a pressure–induced increase in the effective mass of the barrier or the electrodes. We speculate that the difference is due to a much thinner barrier and considerable inter–diffusion at the interfaces of MOCVD structures on a scale of the barrier thickness allowing Γ–point tunnel currents to dominate. In addition we cannot rule out the possibility that a parasitic series resistance exists in these samples which increases with pressure.

CHAPTER 7

Double Barrier Resonant Tunnelling Structure

7.1 Experimental Results

The specifications of the double barrier AlAs/GaAs/AlAs structure studied here are explained in detail in Chapter 5. Figure 7.1 shows the conduction band profile of the structure at zero bias where the emitter is the nominally undoped electrode and the collector is the highly doped one. The measurement of the I-V characteristics of this sample has been performed at ambient and high pressures in both forward (emitter negative) and reverse (emitter positive) biases. In forward bias a 2D accumulation layer is known to form at the GaAs/AlAs interface (Hickmott (1985), Bockenhoff *et al.* (1988), Othaman *et al.* (1991,93)) (see Fig. 7.13 for example). In this case electrons are injected into the barrier structure from the 2D subbands. Upon the application of hydrostatic pressure this device shows distinctly different I-V characteristics in forward and reverse biases. A single resonance has been observed in forward bias at atmospheric pressure and two different resonances in forward and reverse biases at high pressures. It is therefore important to treat these measurement regimes separately in this chapter.

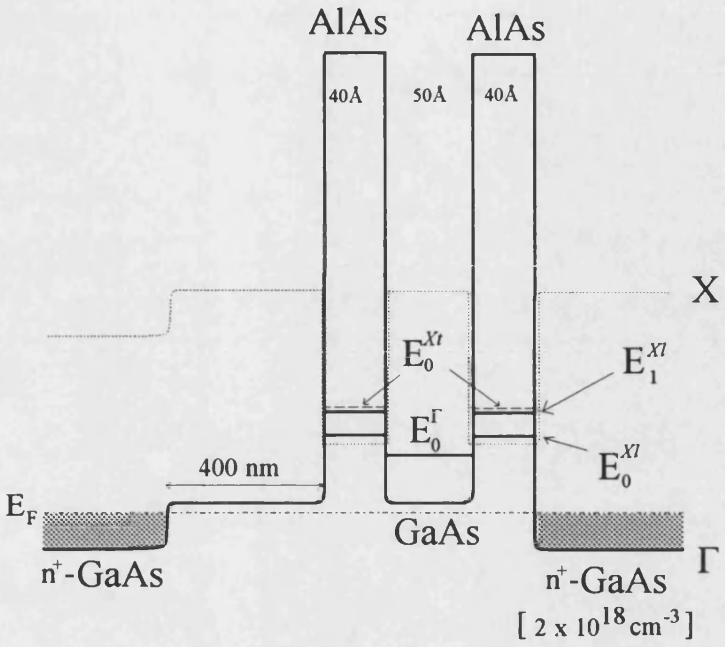

Figure 7.1 : Potential profile of the sample at zero bias

7.1.1 Measurement at Ambient Pressure

The rectifying nature of this asymmetrically doped double barrier diode is seen in its I-V characteristic at ambient pressure and temperatures between 10 - 77 K which are shown in Fig. 7.2. A closer look on an expanded scale (Fig. 7.3) shows a weak resonance occurring at a forward bias of +0.3 V at 10 K. The existence of this resonance is clearly shown by a rapid drop in the differential conductance (dI/dV) which is then followed by a strong increase in current at larger voltages. At this temperature the current does not show any true valley structure and therefore the peak-to-valley ratio is not measurable. Below 10 K this resonance develops into a region of negative differential resistance (NDR). Similar but larger resonances have also been observed by Pritchard *et al.* (1989) with measured PVR of 8.4 at 77 K (see also Mendez *et al.* (1988) and Bonnefoi *et al.* (1988)). In reverse bias very little current flows until a breakdown voltage of about

-2 V is reached because the majority of the potential drop falls across the 400 nm nominally undoped GaAs electrode. No resonance is observed in the reverse bias current at 1 bar.

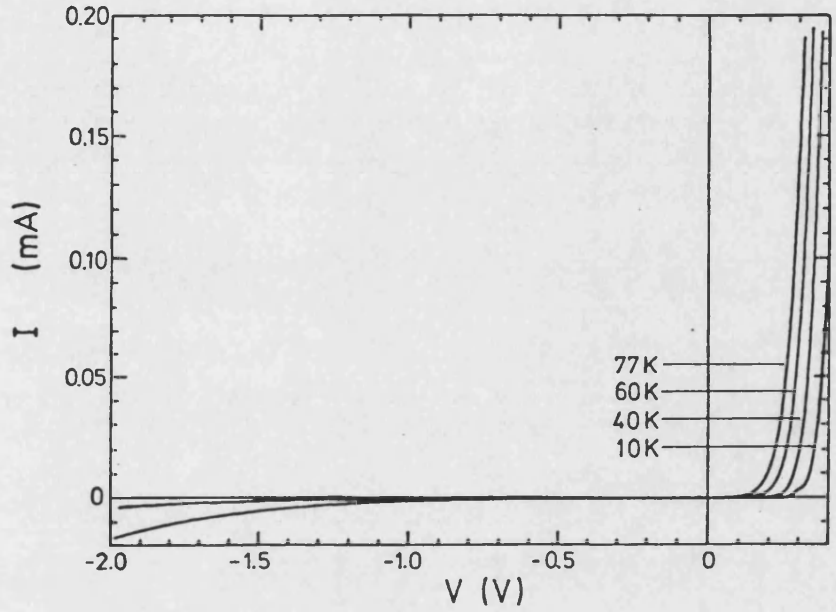

Figure 7.2 : I-V characteristics at ambient pressure and temperature in the range 10-77 K

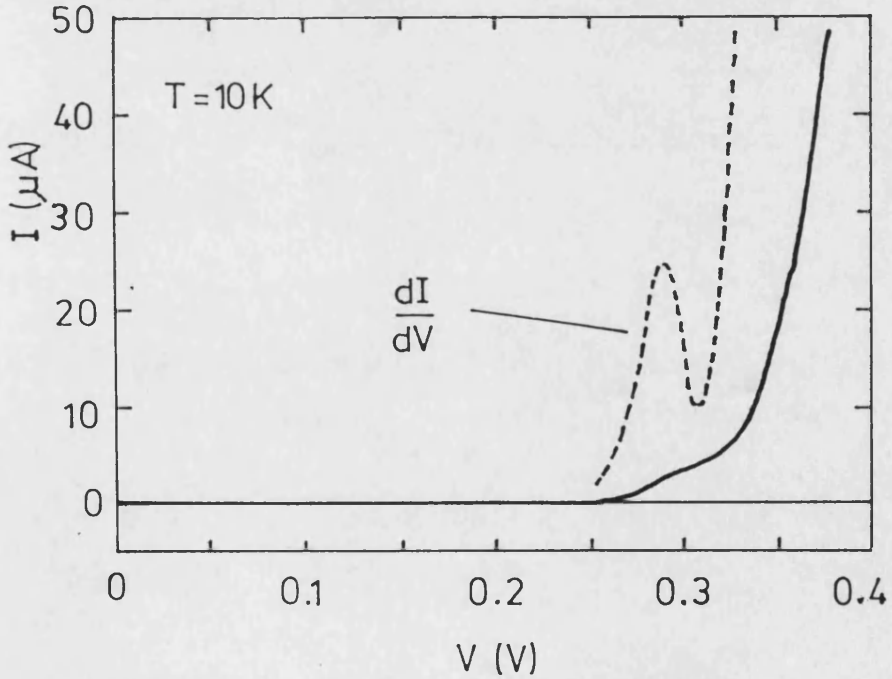

Figure 7.3 : I-V characteristic at 10 K on an expanded current scale

7.1.2 The Forward Bias Characteristic Under Pressure

The forward bias current density at 1 bar and 77 K is considerably larger than at 10 K and no trace remains of the resonance peak near +0.3 V. However, upon application of hydrostatic pressures in excess of 4 kbar a clear current peak appears in the voltage range 0.2 - 0.25 V as shown in Fig. 7.4. Figure 7.5 shows the dI/dV plot of the same measurement where a region of NDR is observable at pressures above ~5.5 - 7 kbar.

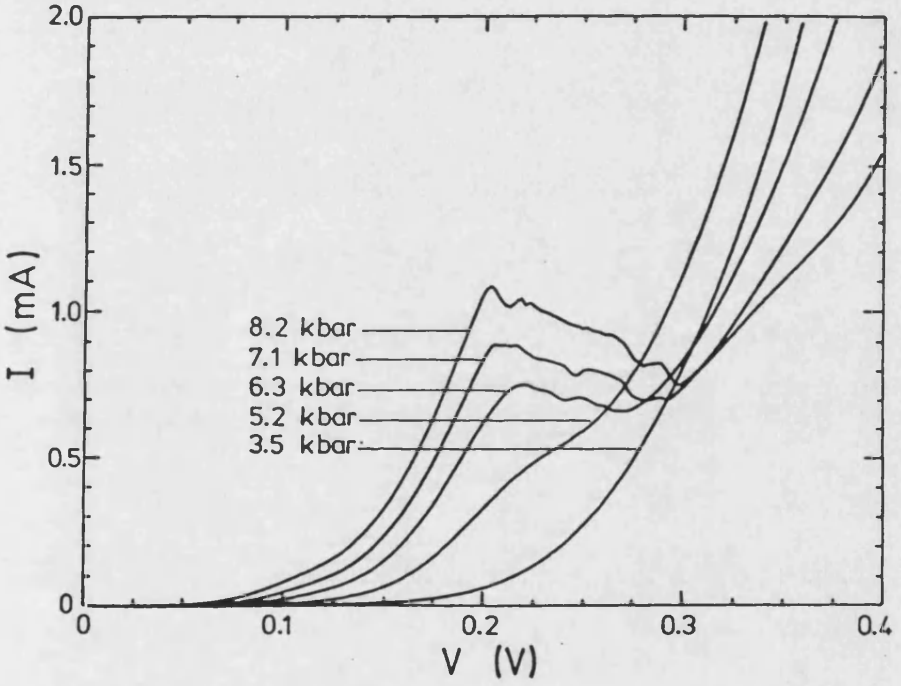

Figure 7.4 : Forward bias I-V plots for a range of applied pressures at 77 K

The plot of the logarithm of the current versus applied pressure for a range of voltages at 77 K is shown in Fig. 7.6. At voltages below the region of NDR we see an almost exponential dependence of current on the pressure as has been observed previously by Mendez *et al.* (1986). The position of the current peak remains almost fixed at around +0.2V as the pressure increases. At the same time the position of the valley shifts towards higher voltages thus increasing the width of the

NDR region. The approximately linear dependence of the current peak-to-valley ratio with pressure can be seen in Fig. 7.7 with a slope of ~ 0.13/kbar. Beyond the valley region for p > 4 kbar the current starts to decrease with pressure as shown in Fig. 7.4 and 7.6. The complex structure between the peak and valley probably relates to spontaneous oscillations of the measurement circuit due to stray inductances as observed by Pritchard *et al.* (1990) and is also clearly shown in the dI/dV plot in Fig. 7.5. A second shoulder appears in the current at a bias of ~ 0.35 V at p~8.2 kbar which is also observable in the conductance.

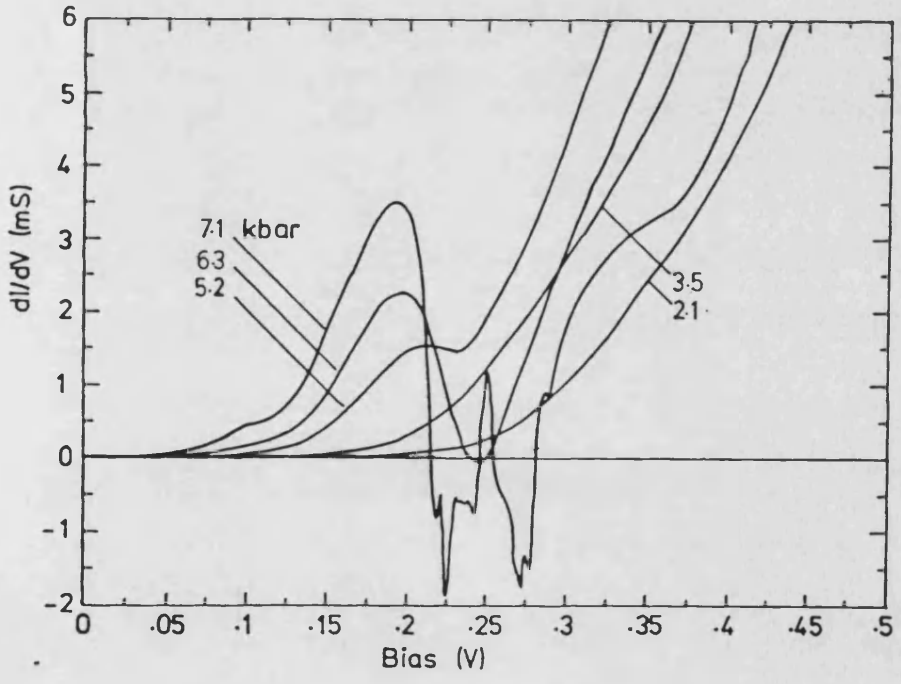

Figure 7.5 : Plot of first derivative dI/dV under forward bias at 77 K for a range of applied pressures.

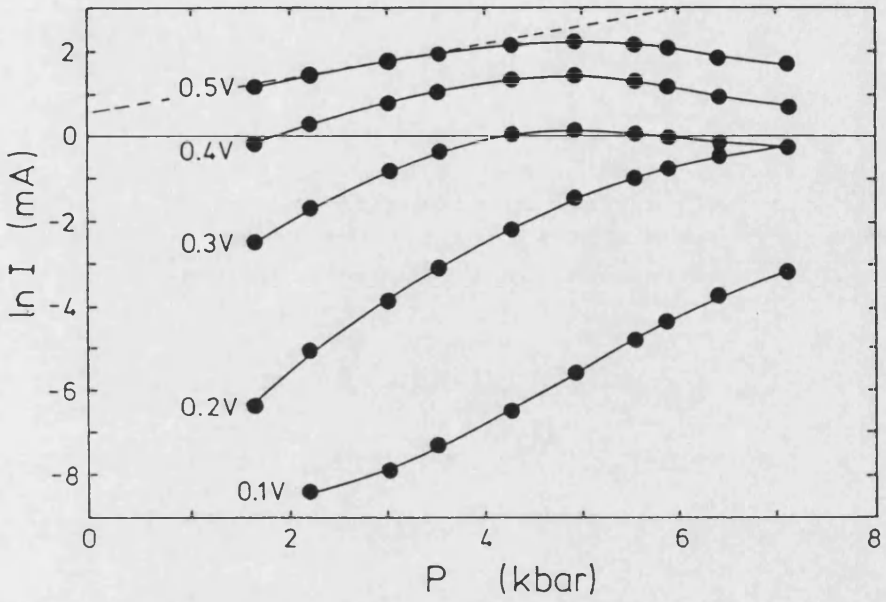

Figure 7.6 : Plot of log I versus applied pressure at 77 K for a range of forward bias voltages.

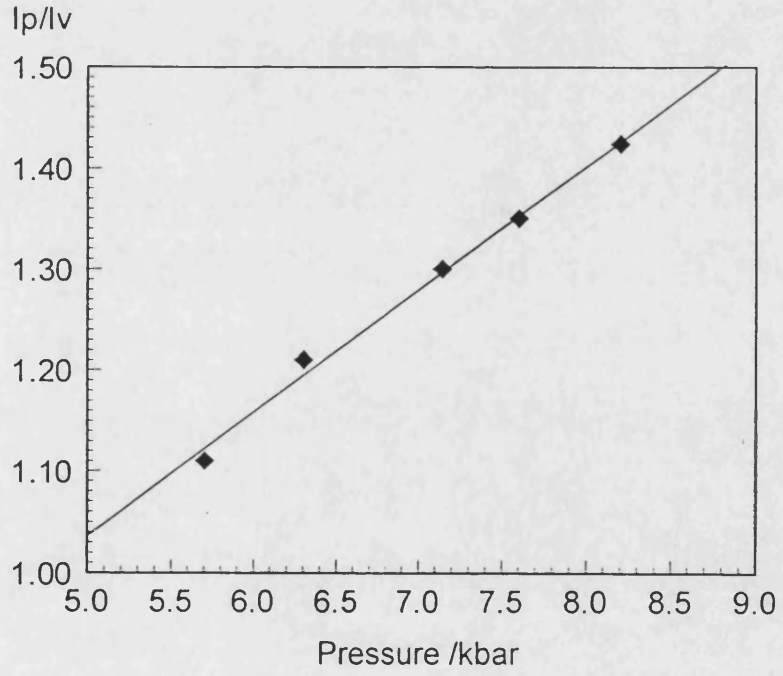

Figure 7.7 : Plot of peak to valley ratio versus applied pressure at 77 K

7.1.3 The Reverse Bias Characteristic Under Pressure

At 1 bar and 77 K almost no current flows in reverse bias until a voltage of about -2 V is exceeded where a clear breakdown becomes visible. This behaviour is broadly sustained on application of hydrostatic pressure until a pressure of about 5 kbar is exceeded. Beyond this pressure a very well defined current peak becomes observable in the voltage range -1 V to -0.6 V (Fig. 7.8) which develops into a region of NDR in dI/dV (Fig. 7.9). On application of pressure the peak current increases from about zero at $p < 5$ kbar to about 80 μA at 8.2 kbar while the position of the current peak shifts superlinearly towards more negative voltages (Fig. 7.10). Figure 7.11 shows explicitly how the peak current increases as a function of pressure for two different devices. The slight difference between the two devices is probably due to slightly different mesa sizes. It can be seen in this plot that the peak current also increases superlinearly with pressure at low pressures ($p < 7$ kbar) and almost linearly at higher pressures ($p > 7$ kbar).

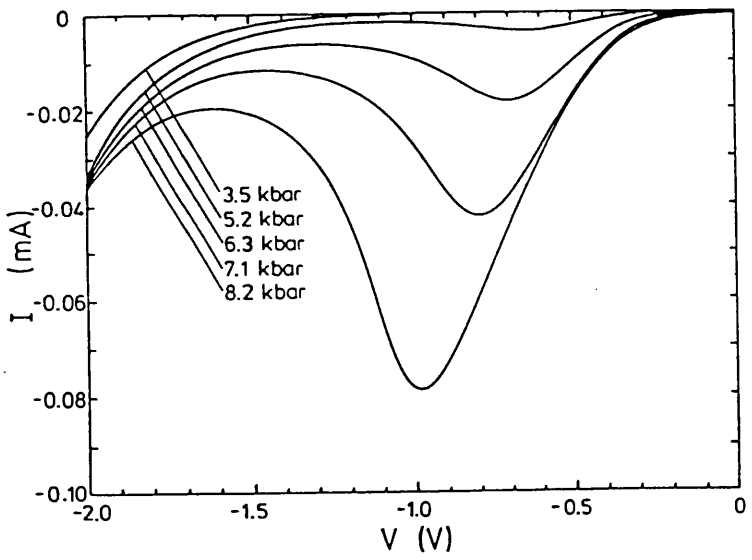

Figure 7.8: Plot of I-V characteristics reverse bias under various applied pressures at 77 K

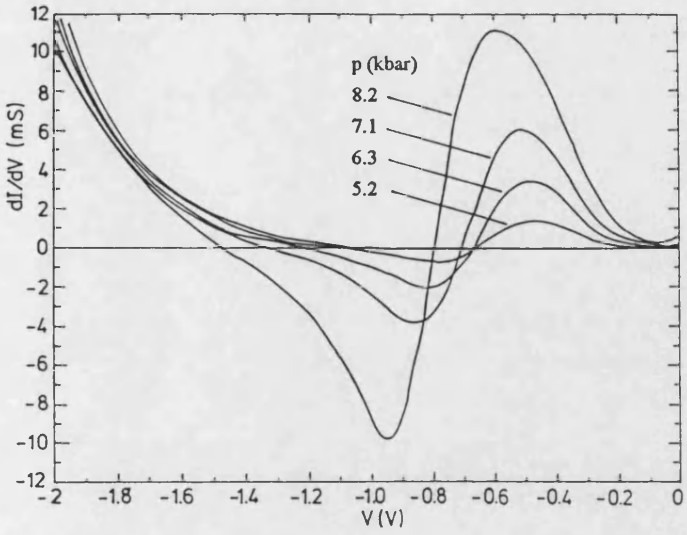

Figure 7.9: Plot of reverse bias conductance at various applied pressure at 77 K

Figure 7.12 records the reverse bias peak-to-valley ratio for the same diodes and shows a very clear threshold at 5 kbar near which the ratio falls steeply to unity while peak-to-valley ratios as large as four have been obtained at 8 kbar. This is in stark contrast to the Γ resonance where the current peak-to-valley ratio normally drops towards unity with increasing pressure.

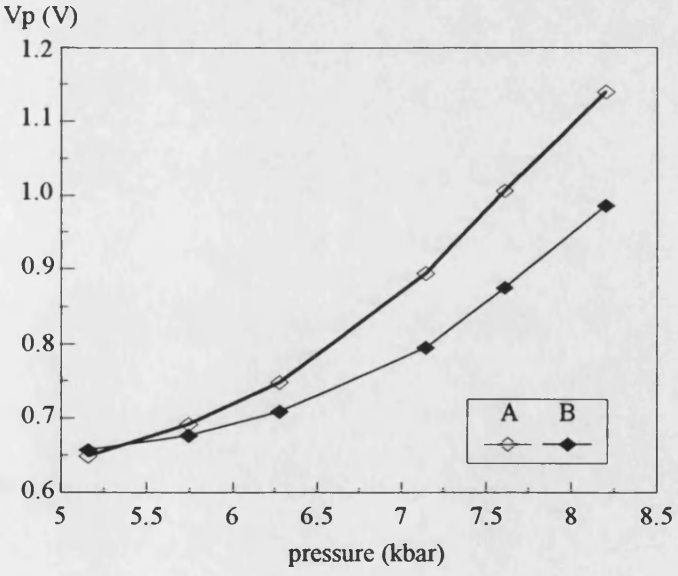

Figure 7.10: Plot of peak position versus applied pressure under reverse bias at 77 K

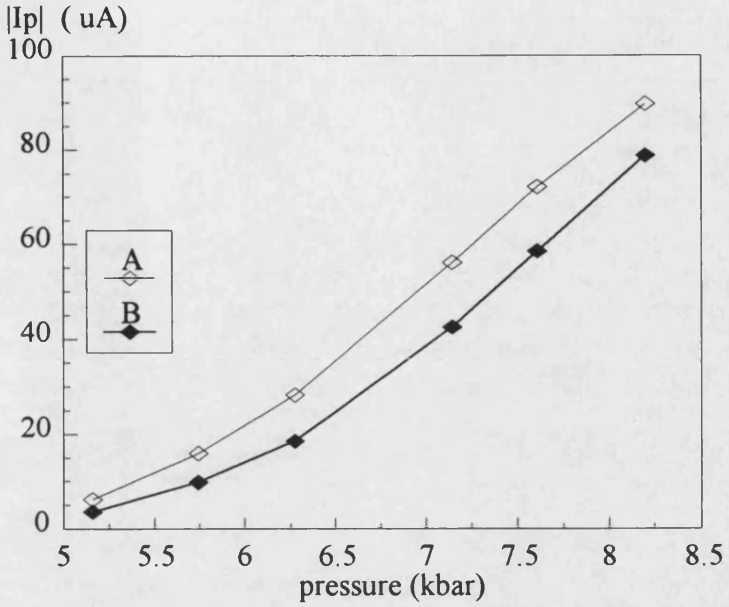

Figure 7.11 : Plot of peak current versus applied pressure at 77K under reverse bias.

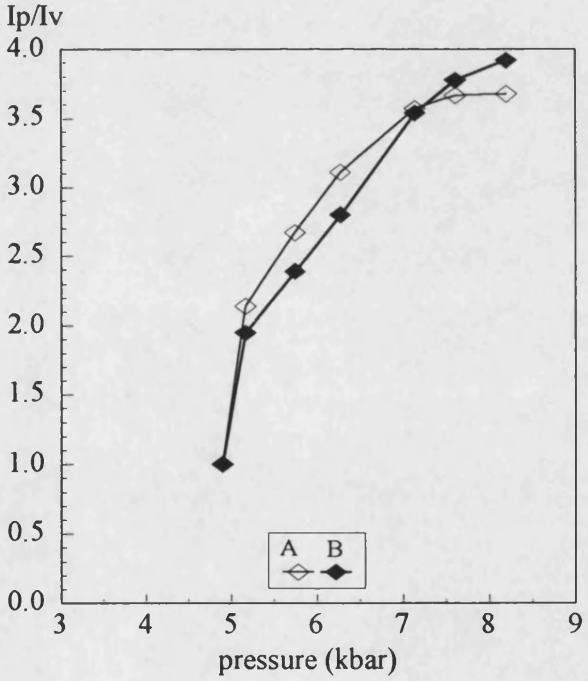

Figure 7.12 : Plot of peak to valley ratio versus applied pressure at 77 K under reverse bias.

7.2 Discussion

7.2.1 Ambient Pressure Tunnelling

In this sample at ambient pressure, the current flow below 10 K is largely dominated by the Γ-point profile of the diode, and the resonance can be attributed to that between the 2D subband forming the accumulation layer and the first Γ-point subband (E_0^{Γ}) in the GaAs quantum well. It is well known that I-V measurements of double barrier GaAs/AlAs structures at ambient pressure exhibit resonant tunnelling between Γ-point subbands in the accumulation layer and quasi-bound states in the GaAs quantum well (Mendez *et al.* (1986,88,90), Pritchard *et al.* (1989,90), Austing *et al.* (1990,93), Bonnefoi *et al.* (1988)). Since the position of the subband energies depend on the width of the well and the height of the confining barriers, the bias position of this resonance depends very much on the specific design parameters of the diode. As the temperature is raised from 10 K to 77 K the forward bias current increases by many orders of magnitude and all sign of the resonance disappears above 20 K. This indicates that at 77 K the current is dominated by a phonon-assisted component probably associated with the X-point conduction band minima in the AlAs barriers.

7.2.2 Tunnelling in Forward Bias at High Pressure

The increase in current with pressure as observed at voltages below 0.2 V in Figs. 7.4 and 7.6 is consistent with an increasing role of the X-point minima in tunnelling. The measured slope at +0.5 V between 1.5 - 4 kbar in Fig. 7.6 is ~0.42 /kbar. This value is a lot smaller than those quoted by Mendez *et al.* (1986) and Rossmanith *et al.* (1993). In order to identify the resonance the confinement energies in the barrier layer and in the quantum well have been estimated using the parameters indicated in Chapter 4. The estimated energies of the X-confined

subbands in the barrier layers at zero bias are at $E_0^{X_l} \cong 15.9$ meV and $E_1^{X_l} \cong 63.3$ meV due to the large longitudinal X-point electron mass and at $E_0^{X_t} \cong 64$ meV due to the smaller transverse X-point electron mass. These energies are measured from the X-point minima in the AlAs barrier. The first subband energy in the GaAs quantum well is calculated to be at $E_0^{\Gamma} \cong 130$ meV from the bottom of the well. Figure 7.1 shows the positions of these energies in the barriers and quantum well respectively. The pressure dependence of the tunnelling current can be attributed to that of tunnelling via longitudinal X-point conduction band minima.

The most surprising feature of Fig. 7.6 is that at voltages beyond the region of NDR the current actually begins to fall again as the pressure is increased above 4 kbar. This is not at all consistent with our conventional picture of a pressure-induced reduction in the energy of the X-minima which would lead to a monotonic enhancement of the current. The origin of this feature must lie elsewhere, more specifically in the distribution of space charge in the structure.

Figure 7.13 shows a sketch of the conduction band edge of the structure under a pressure of 5 kbar, at two different voltages. As described above the application of a forward bias to the diode causes the formation of an accumulation layer at the GaAs/AlAs interface. This layer comprises a 2D subband which is occupied up to the Fermi energy (E_F). The dominant contribution to the current from this 2D electron gas at 77 K will be due to phonon-assisted tunnelling through the small triangular shaped barrier defined by the X-minima in the adjacent AlAs layer as observed at low voltages. However, at higher biases the $E_0^{X_l}$ subband in the barrier falls below the Fermi level in the electrode, and it becomes possible for electrons to tunnel resonantly via this level. No true resonance can in fact occur since the effective masses of the two 2D systems differ by a factor of almost three

and the dispersion curves cannot nest (Othaman *et al.* (1991, 1993)). Nevertheless a small current enhancement would be expected over a fairly broad range of voltages as has been observed before in a rather different structure (Mendez *et al.* (1987)).

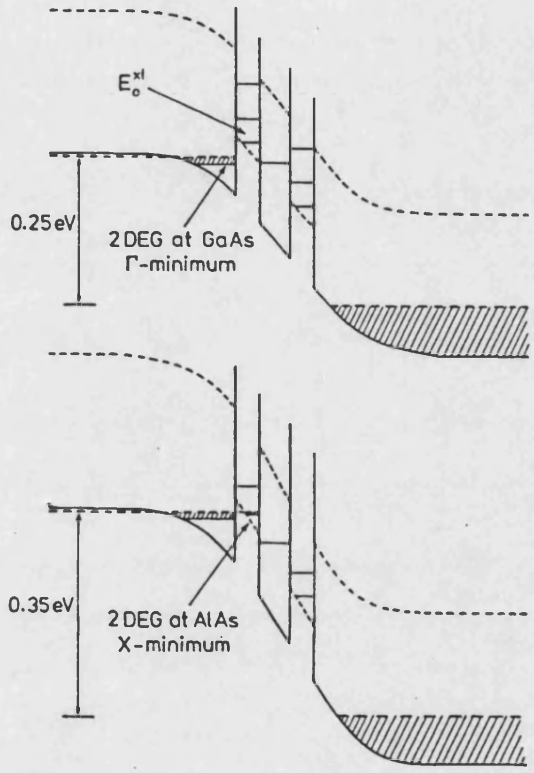

Figure 7.13 : Sketch of the potential profile through the diode under an applied pressure of 5 kbar at two different forward bias voltages.

More importantly, space charge can now start to build up at the E_0^{xl} level in the barrier since the probability of tunnelling into the state is a lot larger than of tunnelling out. As the pressure and voltage are increased a point will eventually be reached where there is no real-space barrier preventing the electrons at the interfacial accumulation layer from transfering to the 2D subband in the AlAs layer. The density of states at E_0^{xl} is about three times larger than at the interface due to the difference in effective masses, and one would expect that most of the additional

additional charge introduced by an increase in applied voltage will be stored in the AlAs barrier. It is even possible that the interfacial accumulation layer actually loses net charge to the E_0^{XJ} subband (sometimes referred to as a Fermi level pinning effect (Austing *et al* (1993)). Due to this charging effect most of the 2D electrons will now be confined at the longitudinal X-minimum in the AlAs barrier by the low-transparency barrier associated with the X-minima in the GaAs quantum well itself, and the current density actually falls. In addition, the field profile within the double barrier structure is now quite different leading to a qualitatively different I-V characteristic. Austing *et al.* (1993) have a similar explanation of this same phenomenon in terms of a reduction of the contribution of the Γ electrons due to the pinning of the Fermi level at an X-point subband in the barrier which subsequently lowers in energy with increasing pressure.

7.2.2 Tunnelling in Reverse Bias at High Pressure

As shown in Fig. 7.8 above, in reverse bias as the pressure is increased from 1 bar current peaks appear between -1 V and -0.6 V with a well developed NDR at pressures above 5 kbar. A calculation based on the subband energies in the barrier layer shows that this resonance can be attributed to the occupation of the E_0^{XJ} subband (~16 meV above the X-point conduction band minima) in the barrier adjacent to the n^+-electrode as was first observed by Mendez *et al.* (1990). These electrons are then able to tunnel resonantly into the E_1^{XJ} (~63 meV) subband in the second AlAs barrier and greatly enhance the tunnel current. Figure 7.14 shows a sketch of the potential profile of the structure under reverse bias at two different pressures. The calculated threshold pressure for the E^{XJ} subband to become occupied is then slightly larger than 5 kbar, in good agreement with the observation. Note that while the applied potential differences are relatively large,

the internal field strengths are very low since most of the voltage falls across the nominally undoped electrode. A similar resonance has been observed by Austing *et al.* (1990), although the observed resonance in this case is at a much lower hydrostatic pressure due to the very high doping level in the emitter electrode. This resonance cannot be attributed to the $E_0^{X_l}$ and $E_1^{X_l}$ since this would occur at a much higher bias ($E_1^{X_l} - E_0^{X_l} \cong$ 153 meV). However, since $E_0^{X_l} \cong E_1^{X_l}$ it is possible to have resonance between $E_0^{X_l}$ and $E_0^{X_l}$ with the scattering of electrons by zone boundary phonons as was observed by Austing *et al.* (1993). Experiments at temperatures down to 4.2 K would reduce this phonon assisted current and allow a conclusive identification of the resonance, but this was not possible with our set up.

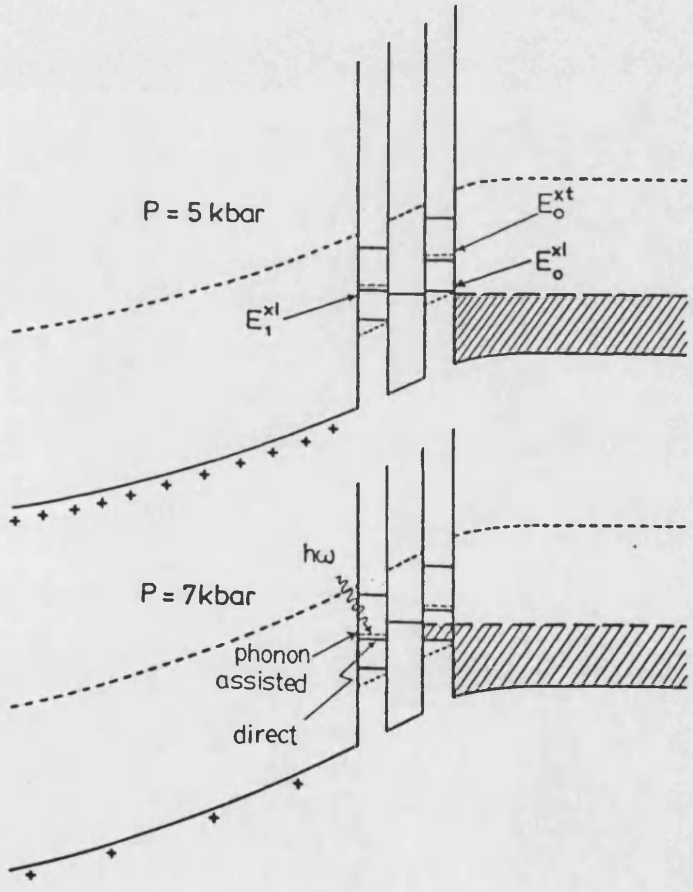

Figure 7.14 : Sketch of the potential profile through the diode near the reverse bias resonance voltage under two different values of applied pressure.

This model does not, however, explain why the resonance shifts to more negative voltages as the pressure increases. One would expect $E_0^{X_J}$ and $E_1^{X_J}$ to decrease in energy at the same rate as the pressure is increased. Therefore the observed shifts must be attributed to a pressure-induced reduction of the background concentration of ionized donors in the 400 nm (nominally undoped) GaAs electrode. Using calculated values of $E_0^{X_J}$ and $E_1^{X_J}$ to estimate the field strength at resonance in the double barrier structure it can be shown that an ionized donor concentration of about 1×10^{16} cm^{-3} and a depletion length of about 0.3 μm would be consistent with the peak voltage of around -1 V at 8 kbar. This represents a reasonable background impurity density which might be obtained during routine MBE growth. Using the Bohr model to calculate the ionization energy of a donor impurity in GaAs one would expect an increase when pressure is applied due to the associated increase in effective mass (Wasilewski *et al.* (1986)) and decrease in dielectric constant. A pressure-induced reduction in the concentration of ionized donors would lead to a complementary increase in the applied voltage to maintain the same electric field at the double barrier structure.

7.3 Conclusions

By deliberate asymmetrical doping of the electrodes of a resonant tunnelling diode it is possible to infer additional information about the effects of applying hydrostatic pressure. At 77 K pressure-induced regions of NDR are seen in both bias directions with clear evidence that they have different origins. A Γ-related resonance arising from the well has only been observed at ambient pressure below 10 K.

In forward bias a current peak is observed above a threshold pressure of 5 kbar. At voltages beyond the region of NDR the current actually begins to fall as

the pressure is increased further. The origin of this feature is believed to be an occupation of the E_0^{Xl} subband adjacent to the accumulation layer at the GaAs/AlAs interface. Most of the additional charge build-up arising from an increase in the applied voltage will accumulate here because of the higher density of states. It is also possible that the 2D electron gas at the interface simultaneously loses net charge to the barrier (Fermi level pinning). Accumulated charge at the E_0^{Xl} subband is now confined by the high barrier associated with the X-minima in the GaAs well leading to a fall in the current. Note: This argument hinges on the confined electrons having a lower probability of scattering down in energy and momentum space to the E_o^{Γ} subband in the GaAs quantum well than of phonon-assisted tunnelling through the X-point barrier at 77 K. The region of NDR in forward bias is, then, a consequence of real-space and k-space transfer of electrons between two 2D systems

In reverse bias a current peak due to a strong resonance occurs above a threshold pressure of 5 kbar. Our calculations of the relevant subband energies indicate that this is associated with an occupation of the E_0^{Xl} subband in the AlAs barrier adjacent to the n^+-GaAs injecting electrode. The subsequent resonance corresponds to a current enhancement upon alignment of this subband with the E_1^{Xl} subband in the opposing barrier (or a phonon assisted resonant process to the E_1^{Xt} subband which is very close in energy).

CHAPTER 8

Metal–Semiconductor Contacts

8.1 Introduction

In 1874 Braun reported the first rectifying nature of a metal whisker contact on a semiconductor (Rhoderick (1978)). Since then there have been many further developments aimed at producing a much better rectifying metal–semiconductor contact by depositing a thin layer of metal directly on top of a semiconductor. Well known as a Schottky diode this device can be fabricated either from an *n*– or a *p*–type semiconductor. Among these the *n*–Si and *n*–GaAs diodes are the most commonly used (Sharma (1984), Mönch (1990)). Due to the specific parameters of most metals and semiconductors a rectifying current-voltage characteristic is produced mostly by metals (such as Au, Al, Pt, Pd, Ag, Cu, W, etc.) in contact with *n*–type semiconductors (e.g. *n*–Si, *n*–Ge, *n*–GaAs) . Among these GaAs is more suitable for higher cut–off frequency applications due to its higher electron mobility (6 times that of Si) and peak drift velocity (Anand (1984)).

Early applications of the rectifying nature of point contact diodes were as frequency converters or low–level microwave detectors. Since then the applications have widened into other branches of modern semiconductor technology such as LEDs, photodiodes and photovoltaic devices in optoelectronics, mixer or detector diodes in microwaves, gate electrodes of MESFETs, electrodes for high–power IMPATT oscillators, charged–coupled devices (CCD), solar cells, thin film transistors and many more. One of the reasons for this wide range of applications is that Schottky contacts do not exhibit minority carrier effects such as long reverse recovery times, diffusion capacitances, etc. as is observed in *p-n* junction devices. In addition they are comparatively easy to fabricate and incorporate into integrated circuits.

In this chapter the discussion starts with the early theory of Schottky barrier formation which is derived from the work of Schottky and Mott (Section 8.2). The initial theory in this section is based on a contact between two clean surfaces ignoring any interface/surface states. In section 8.3 this theory is then modified to include interface states and the related effects due to pinning of the Fermi level at metal–semiconductor contacts. The current transport mechanism is then explained in Section 8.4 based on models of thermionic emission, thermionic field emission, and quantum tunnelling. The study of Schottky barrier formation enables us to investigate the electronic nature of semiconductor surfaces. In this study we use Pd/n^+–GaAs Schottky diodes to obtain information about the GaAs surface and the Schottky barrier height as well as the nature of donors in the depletion region. Section 8.5 discusses some effects of hydrogen passivation on semiconductor materials especially in passivating the surface states. Finally in Chapter 9 we discuss our experimental procedure of Schottky contact passivation, the results of current-voltage measurements and theoretical simulations.

8.2 Theory of the Schottky Barrier : Schottky–Mott Limit

8.2.1 The Schottky Barrier Formation

The mechanism leading to the rectifying I–V characteristic of a metal–semiconductor contact was first explained independently by Schottky and Mott in 1938 (Mönch (1990)). Their explanation is based on the difference between the work functions of the metal and semiconductor which leads to a built–in contact potential where the work function of a material is defined as the energy required to raise an electron from its Fermi level to the vacuum level. Figure 8.1(a) shows the situation for separated slabs of a metal and a degenerately doped n^+–semiconductor where the metal work function ϕ_m is greater than the semiconductor work function ϕ_s. Since the work function in a semiconductor depends on its doping density it is normally replaced with its electron affinity χ_s which is the energy difference between the bottom of the conduction band and the vacuum level. The discussion given in this section is based mostly on degenerately doped n^+–semiconductors because of their application in our experimental work, but the theory is equally valid for other types of semiconductor with some modifications.

When the metal is brought into intimate contact with an n^+–semiconductor (Fig. 8.1(b)) electrons from the conduction band of the semiconductor (which is at a higher energy if $\phi_m > \phi_s$) flow onto the metal surface aligning the two Fermi levels when a condition of equilibrium is reached. The transferred electrons then form a thin sheet of negative charge (within a Thomas–Fermi screening length ~0.5 Å) on the metal surface (labelled Q_m in Fig. 8.1(b)). In the n–type case an equal amount of positive charge due to the ionised donors is then left behind in the semiconductor region near the interface (labelled Q_s). The region where electrons are depleted in the semiconductor within the length w_o from its boundary with the

metal is called the *depletion region*. Since it is depleted of charge carriers this region becomes highly resistive. In equilibrium $Q_m = Q_s$ and the Fermi level is constant throughout the metal and semiconductor.

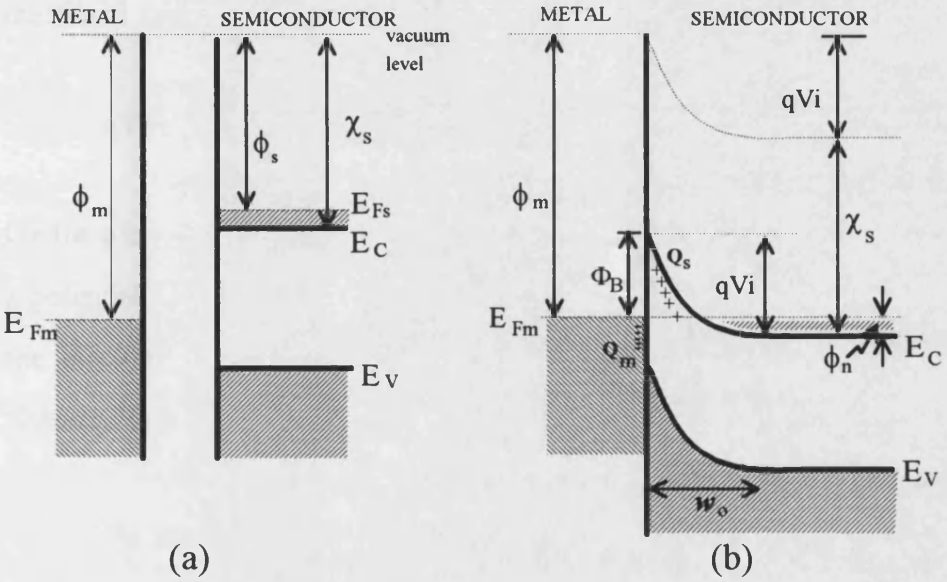

Figure 8.1 : Energy band diagrams of a metal contact on an n^+-semiconductor with $\phi_m > \phi_s$. (a) When the materials are separated; (b) When the materials are in contact and in thermal equilibrium.

The conduction band of the semiconductor has to bend upwards near the interface under the influence of the positive depletion charge there (see Fig. 8.1(b)). This is mirrored by a bending of the valence band edge because the energy gap remains constant throughout the semiconductor. It is also assumed that the electron affinity does not change throughout the semiconductor. The existence of negative charges on the metal surface and positive charges in the depletion region of the semiconductor creates a large electric field there. Schottky assumed that the density of space charge in the depletion region is uniform and therefore the electric

field strength increases linearly with distance from the edge of the depletion region. The linear increase in electric field then gives rise to a quadratic potential and forms the parabolic barrier. The band bending causes a built in potential barrier V_i which an electron moving from the semiconductor into the metal has to surmount. This built in potential is equal to the difference between the work functions of the metal and semiconductor, i.e.

$$qV_i = \phi_m - \phi_s \tag{8.1}$$

On the other hand the electrons that move from the metal to the semiconductor see a potential barrier Φ_B which is the difference between the metal work function and the electron affinity of the semiconductor. This potential barrier is known as *Schottky barrier height* and is given by

$$\Phi_B = \phi_m - \chi_s \tag{8.2}$$

This is known as the *Schottky–Mott limit* where in Fig. 8.1(b)

$$\phi_s = \chi_s - \phi_n$$

$$\Phi_B = qV_i - \phi_n \tag{8.3}$$

$$\phi_n = E_F - E_C$$

E_C and E_F are the conduction band edge and Fermi level of the semiconductor far from the interface respectively. At equilibrium (zero bias) the rate of electrons moving into the semiconductor must be equal to the rate of electrons moving in the opposite direction thus no net current flows.

8.2.2 Forward Bias

The thermionic emission current density in a Schottky diode can be given by (see Rhoderick (1979) and Sze (1981) for example)

$$J = j_s \exp\left(\frac{eV}{nkT}\right)\left(1 - \exp\left(-\frac{eV}{kT}\right)\right) \qquad (8.4)$$

where n is the ideality factor and the rest of the symbols have the usual definitions. The reverse bias saturation-current density is given by

$$j_s = A^* T^2 \exp\left(-\frac{(\Phi_B - \Delta\phi_{if})}{kT}\right)$$

where $\Delta\phi_{if}$ is the image force barrier lowering, k is Boltzmann's constant and A* is the Richardson constant.

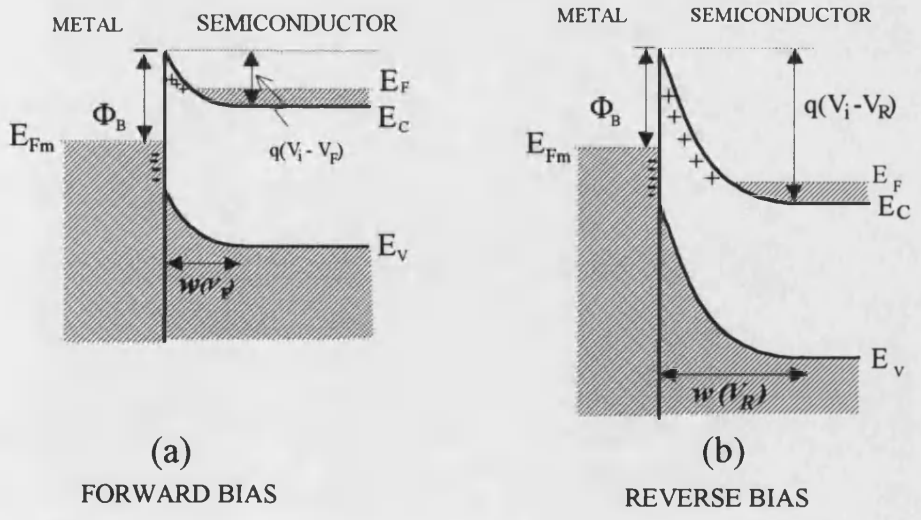

Figure 8.2 : Schottky contact for n^+-semiconductor under
(a) forward and (b) reverse bias conditions.

When the n^+–semiconductor is biased negatively with respect to the metal the bands and consequently the electron energies in the semiconductor are raised relative to those in the metal (Fig. 8.2(a)). Since the depletion region is highly resistive most of the applied voltage V_F appears across this region. As a consequence the width of the depletion region is reduced and the built–in potential is also reduced to $V_i - V_F$. The barrier height seen by electrons travelling from the semiconductor to the metal is reduced and more electrons are able to flow in this direction. On the other hand the barrier height Φ_B seen by electrons travelling from the metal remains constant. As a consequence there is a net electron flow from the semiconductor to the metal i.e. a net current flow from the metal to the semiconductor. For increasingly negative voltages at the semiconductor electron flow from the semiconductor to the metal increases exponentially hence this is termed forward bias.

8.2.3 Reverse Bias

When the semiconductor is biased positively with respect to the metal with a voltage V_R the built–in potential is increased to $V_i - V_R$ which leads to an increase of the depletion region width. The bands and consequently the electron energies in the semiconductor are lowered relative to those in the metal (Fig. 8.2(b)). The barrier height seen by electrons travelling from the semiconductor to the metal is increased and fewer electrons flow in this direction but the barrier height Φ_B seen by electrons travelling from the metal to the semiconductor remains constant. Therefore there is a small net flow of electrons from the metal to the semiconductor. At larger values of reverse bias there will be fewer electrons flowing from the semiconductor to the metal but the rate of electrons flowing in the opposite direction remains approximately the same. Eventually the number of electrons flow from the semiconductor to the metal approaches zero and the net

current reaches saturation. This is the condition for reverse bias. Since the current flowing in forward bias is many orders of magnitude larger than in reverse bias the diode produces a rectifying I–V characteristic (Fig. 8.3).

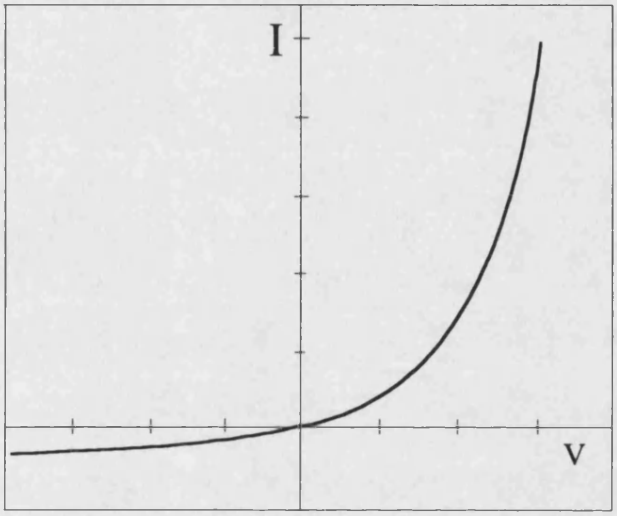

Figure 8.3 : A typical rectifying I–V characteristic of an ideal Schottky contact.

8.2.4 Metal Contacts on an *n*–type Semiconductor with $\phi_m < \phi_s$

The situation is quite different if $\phi_m < \phi_s$. Figure 8.4(a) shows the condition when both the metal and the semiconductor are well separated and the Fermi level in the metal is higher than that in the semiconductor. When the metal and the semiconductor are brought into contact electrons flow from the metal into the semiconductor causing an accumulation of electrons on the semiconductor side of the boundary (Fig. 8.4(b)). The positive charges that are left behind form a thin layer of surface charge on the metal. There is no depletion region formed in the semiconductor and no substantial potential barrier in either direction. This type of

metal–semiconductor contact where the flow of electrons faces no potential barrier in either direction is called an *ohmic contact*.

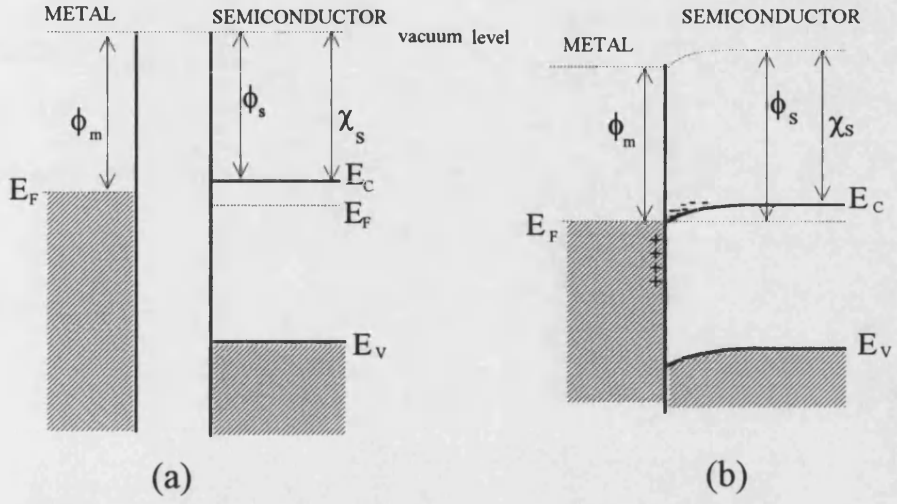

Figure 8.4 : A metal–semiconductor contact with $\phi_m < \phi_s$

8.2.5 Metal Contacts on *p*–type Semiconductors

For a *p*–type semiconductor with $\phi_m < \phi_s$, the bands bend downwards because of the negative charge on the ionised acceptors. A space charge layer of ionised acceptors is formed within a depletion length w_o. Since holes constitute the majority charge carrier they face a potential barrier with a barrier height

$$\Phi_{Bp}=E_g-\phi_m+\chi_s \qquad (8.5)$$

Therefore *p*–type semiconductors with $\phi_m < \phi_s$ also give rise to rectifying I–V characteristics. On the other hand if $\phi_m > \phi_s$, the bands bend upwards and the metal

and semiconductor form an ohmic type contact (Rhoderick, 1979). From Eqs. (8.2) and (8.5) it can be deduced that for a given semiconductor

$$\Phi_{Bn}+\Phi_{Bp} = E_g \qquad (8.6)$$

These barrier heights introduced above are also called flat-band barrier heights and do not include contributions from the effects of an applied bias, image force lowering and interface states. Experimentally barrier heights can be measured from I–V, C–V and photoelectric measurements and detailed explanations of these techniques have been given by Rhoderick (1979) and Tyagi (1984).

8.3 The Influence of Surface States : Bardeen Limit

Theoretically for a given metal–semiconductor contact the barrier height depends linearly on the metal work function as shown in Eq. (8.2). However, in practise the barrier height is less dependent or does not depend at all on the metal work function (Cowley *et al* (1965), Heine (1965), Rhoderick (1978), Sharma (1984), Mönch (1990)). Fig. 8.5 shows measured values of experimental barrier height versus metal work function for GaAs. In practise the barrier height is approximately *pinned* to a fixed level ϕ_0 (Rhoderick (1978), Mead *et al* (1964), Crowell *et al* (1964), Mönch (1990)) such that

$$\Phi_B = E_g - \phi_0 \qquad (8.7)$$

which is known as the *Bardeen limit*.

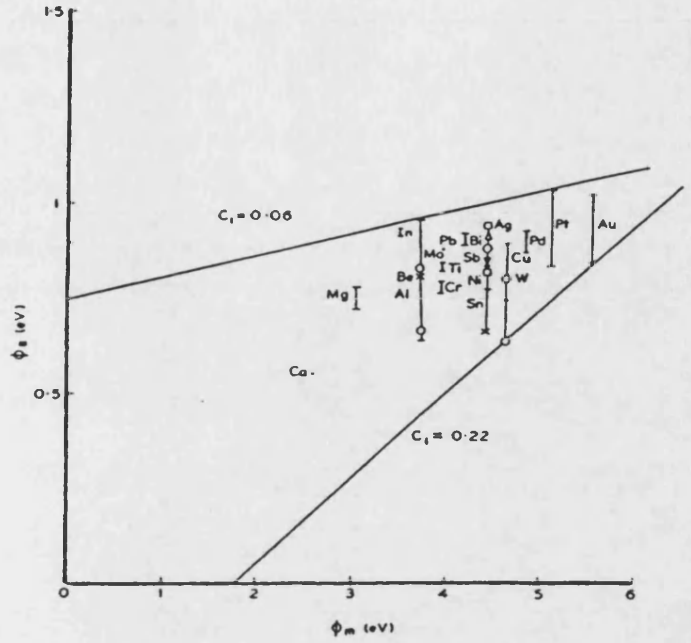

Figure 8.5 : Experimental values of Schottky barrier height (Φ_B) for various metals on *n*–GaAs.(After Sharma (1984)).

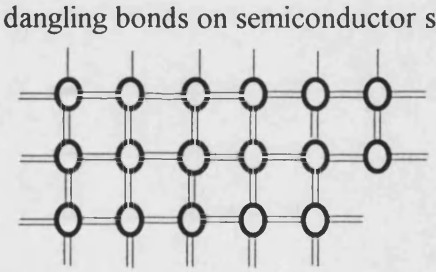

Figure 8.6 : Crystal structure showing dangling bonds on the surface.

In 1947 Bardeen proposed an explanation of this problem in terms of surface states. On the surface of a semiconductor there exist incomplete atomic bonds which are called dangling bonds (Fig. 8.6). These dangling bonds give rise to localised electronic states at the surface with energy levels lying within the energy

gap. Better known as surface states (or interface states when a semiconductor is in contact with a metal) these energy levels can be either discretely or continuously distributed in the band gap and are characterised by the neutral level ϕ_0. Figure 8.7 shows the position of this level within the band gap of a semiconductor where an insulating layer of thickness δ is included at the interface with the metal.

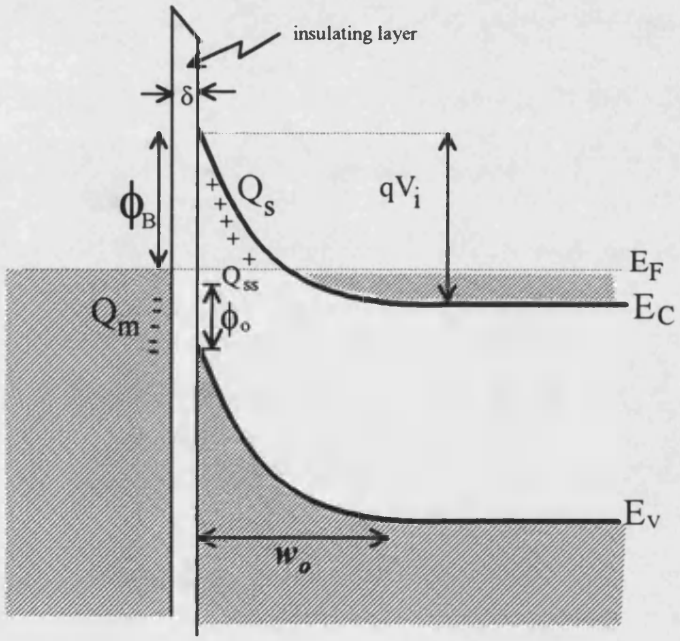

Figure 8.7 : Metal–semiconductor contact shows the position of neutral level ϕ_0 within the band gap of semiconductor.

In most metal–semiconductor contacts the semiconductor surface is prepared by chemical cleaning before metal deposition and a thin insulating oxide layer is invariably left on the surface of the semiconductor. The position of this neutral level is such that when there is no band bending in the semiconductor the states are occupied by electrons up to this level making the surface electrically neutral. If states below ϕ_0 are empty the surface has a net positive charge while, if

states above ϕ_0 are filled, the surface has a net negative charge. For a sufficiently high density of surface states ($D_s > 10^{12}$ cm^{-2}), there will be a double layer at the free surface of a semiconductor formed from a net charge from electrons on surface states and a space charge of opposite sign. This double layer tends to make the work function independent of the position of the Fermi level in the interior of semiconductor and the rectification characteristics of metal-semiconductor contacts are then practically independent of the metal. According to Bardeen this double layer extends to a depth of $10^{-6} - 10^{-4}$ cm into a semiconductor (Tyagi (1984)).

If Q_m is the negative charge density on the metal side of the interface, Q_s is the positive charge density in the depletion layer and Q_{ss} is the surface state charge density, then in equilibrium

$$Q_m + Q_s + Q_{ss} = 0 \qquad (8.8)$$

The limiting case is when ϕ_0 coincides with the Fermi level i.e. when there is very high density of surface states.

Based on the idea of surface states proposed by Bardeen, Cowley and Sze (1965) obtained a theoretical expression for the barrier height which is given by

$$\Phi_B = \gamma(\phi_m - \chi_s) + (1 - \gamma)(E_g - \phi_0) - \Delta\phi_n \qquad (8.9)$$

where $\Delta\phi_n$ is an image force barrier lowering and E_g is the energy band gap of the semiconductor. The weighting factor γ is given by

$$\gamma = \frac{\varepsilon_i}{\varepsilon_i + e\delta D_s}$$

Where D_s is the surface state density. For GaAs the neutral level is believed to be about a third of the way up the energy gap from the valence band edge (Mead & Spitzer (1964)) and Offsey *et al.* (1986) found that the Fermi level of GaAs is pinned at 0.8 eV below the conduction band at a surface state density of about 10^{12} states cm^{-2}. For a vacuum cleaved semiconductor $\delta \sim 4$–5 Å and the permittivity of the insulating layer, $\varepsilon_i \cong \varepsilon_0$ (Tyagi (1984)) where ε_0 is the permittivity of free space.

The limiting cases of Eq. (8.9) are:

(i) When $D_s \rightarrow \infty$ i.e. $\gamma \rightarrow 0$ $\Phi_B = E_g - \phi_0 - \Delta\phi_n$. In this case E_F is pinned at ϕ_0 and the barrier height is independent of metal work function. This is equivalent to the Bardeen limit (Eq. 8.8) with an additional contribution from the image force barrier lowering.

(ii) When $D_s \rightarrow 0$ i.e. $\gamma \rightarrow 1$ $\Phi_B = \phi_m - \chi_s - \Delta\phi_n$. There are no surface states and the barrier height approaches the Schottky–Mott limit (Eq. 8.2).

However, the real physical mechanisms which determine the barrier height in Schottky contacts have remained controversial. Its formation is affected by the type of interface which exists between the metal and the semiconductor. Tyagi (1984) and Bachrach (1984) have classified in detail the type of interface found between metals and semiconductors :–

(1) Chemically clean contacts such as semiconductor surfaces cleaved under ultrahigh vacuum. Metal is then deposited *in situ* immediately after cleaving and provided there is no interaction between the metal and the semiconductor this represents the ideal method of fabricating Schottky contacts. However, there

sometimes exists structural or compositional disorder due to defects such as steps, surface vacancies or antisite arrangements.

(2) Reactive interfaces resulting in an interfacial reaction between metal and semiconductor. Most of these interactions between metals and semiconductors are complex and result in one or more chemical compounds (Tyagi (1984)). In these situations abrupt and epitaxial interfaces as found in ideal cases are not observable. Metal deposits disrupt surface bonds on the substrate and lead to an exchange of atoms. Interdiffusion can result in interface layers with radically different characteristics from the supposed components (Tyagi (1984)). For example an aluminium Schottky contact on GaAs may form an interfacial layer of AlAs on AlGaAs resulting in the inclusion of a heterojunction interface in the barrier (Bachrach (1984)). Andrew and Phillips (1975) even found a linear correlation between the barrier height and heat of formation of chemical compounds (e.g. silicides) or alloys.

(3) Contacts with surface states and an insulating interfacial layer. Frequently a thin film of native oxide is left during the surface preparation of a semiconductor which prevents an intimate contact. For effective electron tunnelling this interfacial layer of oxide should be less than 20 Å in thickness (Tyagi (1984), Duke (1969)).

If there is some lattice mismatch at the interface the contact also strains the surface and modifies the barrier height. Normally the interface reaches a stable configuration within 3 – 10 monolayers for most metals on GaAs (Sharma (1984)).

The properties of the barrier can also be affected by the formation of donors or acceptors due to the incorporation of metal into the semiconductor lattice such as in the case of Au/GaAs Schottky contacts. In some extreme cases it

is possible that the type of semiconductor is reversed and a p–n junction is formed (Bachrach (1984)).

The Bardeen theory of surface/interface states is not accepted by Heine (1965) who questions the existence of surface states and the role they play in pinning the Fermi level. He suggested that in clean contacts between a semiconductor and a metal the conduction electrons in the metal can tunnel into the forbidden gap of the semiconductor. The wave functions of these electrons decays exponentially into the semiconductor with a decay length ~ 10 Å. The tail states as he called them are not localised but extend into the semiconductor. These can be thought of as replacing the surface states associated with dangling bonds and would be there in the absence of the contact. Louie & Cohen (1976) suggested that the pinning of the Fermi level is caused by metal–induced gap states (MIGS). This MIGS model is similar to Heine's tail state theory except the decay length is only of the order of a bond length.

8.4 Current Transport Mechanisms

A complete theory of various current transport mechanisms is given in great detail by Rhoderick (1978) and Tyagi (1984). There are four different ways carrier transport can take place in a metal-semiconductor contact namely:

a) thermionic emission of electrons over the barrier,

b) quantum-mechanical tunnelling,

c) recombination (or generation) in the space charge region, and

d) recombination in the neutral (bulk) region ('hole injection').

In a degenerately doped *n*-type semiconductor contributions due to carrier recombination as in (c) and (d) are very small and negligible. Therefore, of the four transport mechanisms mentioned above only thermionic emission and electron tunnelling are major contributors. Since the experiments in this work are performed at low temperatures our theoretical simulation is limited to current due to quantum mechanical tunnelling only.

8.4.1 Thermionic Emission Over the Barrier

In Bethe's thermionic-emission theory as described by Rhoderick (1978) the effects of drift and diffusion in the depletion region are assumed to be negligible. Current is then limited to the actual transfer of electrons across the interface and the current-voltage characteristic is described by

$$I = I_0\left(\exp\left(\frac{eV}{kT}\right) - 1\right) \qquad (8.11)$$

where

$$I_0 = SA^*T^2 \exp\left(-\frac{\Phi_B}{kT}\right)$$

$$A^* = \frac{4\pi m^* ek^2}{h^3}$$

where A^* is the Richardson constant for thermionic emission from the metal into the semiconductor, S is the interface area and the other symbols have the usual definitions. For a spherical constant-energy surface such as GaAs, A^* has the value $1.2 \times 10^6 (m^*/m_0)$ $Am^{-2}K^{-2}$.

8.4.2 Quantum Mechanical Tunnelling

(i) Padovani and Stratton Model (Padovani & Stratton (1966, 1967))

In a metal-semiconductor contact the tunnel current dominates when the barrier is sufficiently thin and the temperature is sufficiently low. This is especially true for a degenerately doped n^+-semiconductor whose Fermi energy lies above the conduction band edge (Fig. 8.8). Since the experiments in this work are performed at low temperatures our discussion will concentrate on the quantum mechanical tunnel current. According to the Padovani and Stratton model the current in forward bias and at low temperatures arises due to field emission (FE) and thermionic field emission (TFE)(see fig. 8.8). At very low temperature, when there is not enough thermal energy to excite electrons, field emission due to the tunnelling of electrons with energies close to the Fermi energy of the semiconductor dominates. When the temperature is raised so that the electrons have a reasonable probability of being excited above the semiconductor Fermi energy but still below the potential barrier, electrons can tunnel through a thinner

barrier (TFE). According to the Padovani & Stratton Model the tunnelling current is given by:

$$I = I_S \exp\left(\frac{eV}{E_0}\right) \qquad (8.13)$$

where

$$E_0 = E_{00} \coth\left(\frac{E_{00}}{kT}\right)$$

and

$$E_{00} = \frac{eh}{4\pi}\left(\frac{N_d}{m^* \varepsilon_s}\right)^{1/2}$$

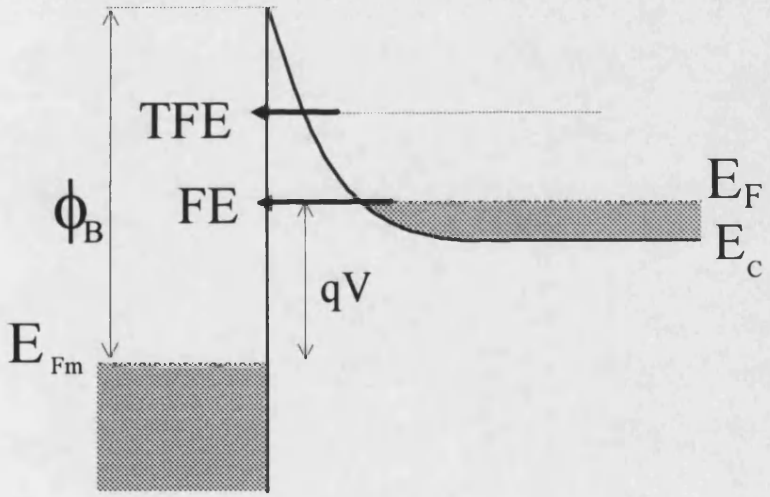

Figure 8.8 : Field emission (FE) and thermionic field emission (TFE) through a Schottky barrier.

I_s in Eq. (8.13) above is only weakly dependent on bias voltage and is a complicated function of barrier height, semiconductor parameters, and temperature. At low temperatures E_{00} may become large compared to kT and we have $E_0 \cong E_{00}$ and the slope of ln I versus V is a temperature independent constant.

This is the case for FE. At high temperatures where $E_{00} << kT$, we get $E_0 \cong kT$ and the slope of ln I versus V is q/kT, which corresponds to TE.

(ii) Two Parameter Model

The tunnelling of electrons in a metal-semiconductor contact has been carefully described by Duke (1969) and also in Chapter 2 of this thesis. Following Duke's derivation which is based on a free electron model the current density is given by

$$J = \frac{(2s+1)e}{(2\pi)^3 \hbar} \int dk_x d^2k_{\parallel} (f_R(E) - f_L(E+eV)) D(E_x) \left(\frac{\partial E}{\partial k_x} \right) \qquad (8.14)$$

where s is the electron spin, $D(E_x)$ is the barrier transparency in the WKB approximation, f(E) is the Fermi function and the rest of the symbols have the usual definitions. Following the same procedure as in Chapter 2 we derive

$$J = e \int_0^{\infty} D(E_x) S(E_x) dE_x \qquad (8.15)$$

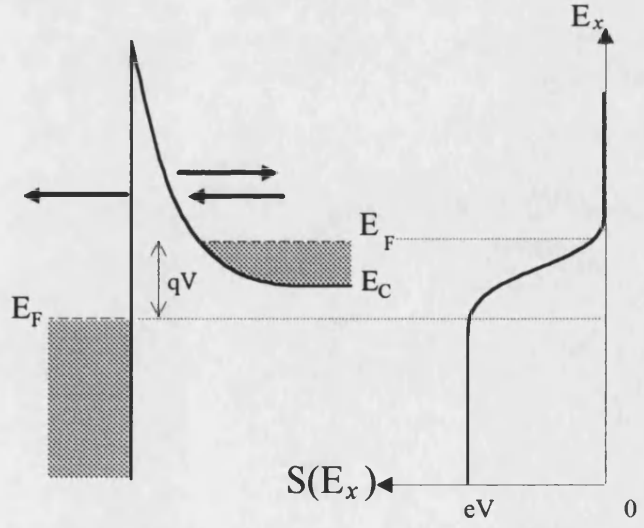

Figure 8.9 : Schottky barrier and its supply function.

where $S(E_x)$ is the supply function as given by Eq. (2.31) in Chapter 2. At T = 0 K, $S(E_x) = 4\pi m^* e^2 V / \hbar^3$ for electrons with energy below the Fermi energy of the positively biased electrode and linearly decreases to zero at higher energies (Fig. 8.9). The computer program we used to model the Schottky diode I-V characteristics in the next Chapter is based on Eq. (8.15) assuming T = 0 and a self-consistent analysis of the electrostatic potential in the depletion region. A full program listing is given in Appendix B.

8.5 Self-Consistent Model of the Potential in the Depletion Region

The equation for the current density in Eq. (8.15) requires solutions of the supply function S(E) and the barrier transparency D(E). The solution of D(E) requires in turn finding the electrostatic potential $\Phi(x)$ in Eq. (2.31). Padovani and Stratton (1966) employ a parabolic barrier approximation to obtain theoretical I-V characteristics in their work. In this work a self-consistent analysis is used to obtain the potential $\Phi(x)$. A complete derivation of the model has been given by Kotel'nikov et al (1985). They conclude that a comparison of the results of the self-consistent model with experimental results for Au/GaAs Schottky diodes yields a better fit than the parabolic barrier model.

Figure 8.10 shows a Schottky barrier Φ_B formed by a degenerately doped n^+-semiconductor and a metal where the interface is defined to be at $x = 0$. Within the depletion region, the electric field, $\mathbf{E}(x)$ and potential $\Phi(x)$ depend upon the barrier height, the applied voltage, and the semiconductor parameters. For a degenerately doped n^+-semiconductor the hole concentration is negligible

compared with the electron concentration and the potential can be obtained by solving the following 1-D Poisson's equation :-.

$$\frac{d^2\Phi}{dx^2} = \frac{e^2}{\varepsilon_s \varepsilon_0}[N_d - n(x)] \qquad (8.16)$$

where

ε_s is the relative permittivity of semiconductor

N_d is the donor concentration

$n(x)$ is the electron concentration at position x.

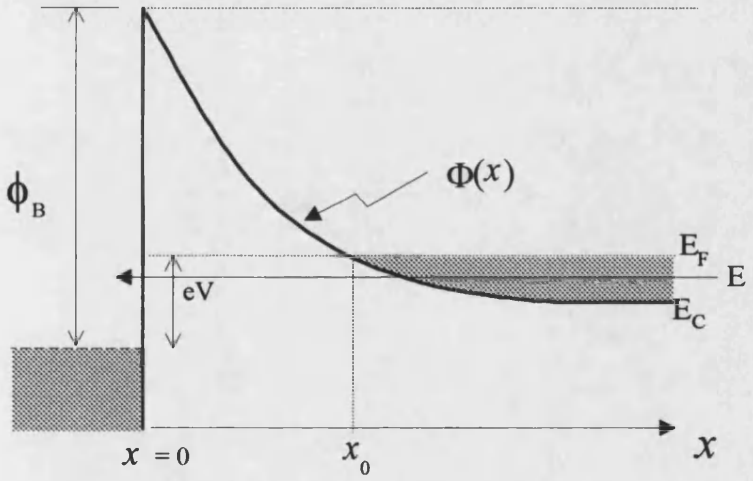

Figure 8.10 : Schottky barrier ϕ_B formed by a degenerately doped n^+-semiconductor and a metal.

The first integral of Eq. (8.16) is given by

$$\frac{d\Phi}{dx} = -\frac{\mu}{l_s}\left(\frac{1}{\mu}\int_0^{\Phi} d\Phi[1 - n(\Phi)/N_d]\right)^{1/2} \qquad (8.17)$$

where

$$l_s = (\sqrt{3}/2) l_{T\text{-}F}$$

$$l_{T\text{-}F} = \left(\frac{x\mu}{6\pi e^2 N_d}\right)^{1/2}$$

Using Fermi-Dirac integrals to obtain n(Φ) and assuming a one-band limit at T = 0 K it can be shown (Kotel'nikov et al (1985)) that

$$\frac{d\Phi}{dx} = -\frac{\mu}{l_s}\left(\frac{\Phi}{\mu} + \frac{2}{5}\left(\left(1 - \frac{\Phi}{\mu}\right)^{5/2} - 1\right)\right)^{1/2} \qquad \Phi < \mu \qquad (8.18)$$

and

$$\frac{d\Phi}{dx} = -\frac{\mu}{l_s}\left(\frac{\Phi}{\mu} - \frac{2}{5}\right)^{1/2} \qquad \Phi \geq \mu \qquad (8.19)$$

The solution for Φ can be divided into two parts according to Fig. 8.10

$$\Phi(x) = \mu\left(\left(\frac{x_0 - x}{2l_s} + \sqrt{\frac{3}{5}}\right)^2 + \frac{2}{5}\right) \qquad 0 \leq x \leq x_0 \quad (\Phi \geq \mu) \qquad (8.20)$$

and

$$\Phi(x) = \frac{6\mu}{\cosh^2((x - x'_0)/2l_{T\text{-}F})} \qquad x \geq x_0 \quad (\Phi < \mu) \qquad (8.21)$$

where x_0 is the point at which $\Phi(x_0) = \mu$ and is given by

$$x_0 = 2l_s\left(\left(\frac{\Phi_0}{\mu} - \frac{2}{5}\right)^{1/2} - \sqrt{\frac{3}{5}}\right) \qquad (8.22)$$

and

$$x'_0 = x_0 - 2l_{T\text{-}F}\ln(\sqrt{5} + \sqrt{6}) \qquad (8.23)$$

Results of this self-consistent calculation are then used to calculate R(dV/dI)-V curves. The experimental barrier height and doping density is then obtained by fitting data to theory. Figure 8.11 shows an example of an R-V plot for an Au/*n*-GaAs junction (Kotel'nikov *et al.* (1987)) at different temperatures. The dashed curves represent calculations based on the self-consistent Schottky barrier with doping density $N_D = 3.2 \times 10^{18} cm^{-3}$ and barrier height Φ_{so}= 1.01 eV at 300 K, 1.04 eV at 4.2 and 77 K. The points are the experimental results.

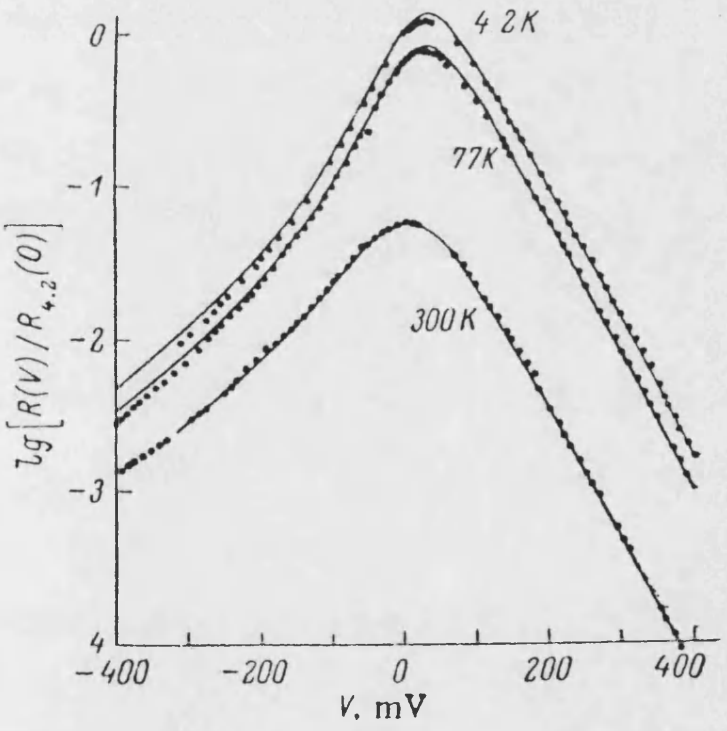

Figure 8.11 : Plot of R(V)/R(0) of a Au/*n*-GaAs junction at temperatures 1) 300 K; 2) 77 K and 3) 4.2 K. The dashed curves represents theoretical calculations and the points are the experimental results. (After Kotel'nikov *et al.* (1985)).

8.6 Hydrogen Passivation in Semiconductor Materials

8.6.1 Introduction

Hydrogen is the smallest, lightest and simplest of all of the elements in the periodic table. It consists of only a single proton and an orbiting electron. Atomic hydrogen is unstable, and the element exists only as a diatomic molecule or in a complex with other elements. Chemically it reacts with most elements and tends to form covalent bonds and due to its large polarisation, it can form bonds as both the H^+ and H^- species.

The role of hydrogen in semiconductors such as Si, Ge, GaAs and AlGaAs has been actively studied by many researchers (see Ashok *et al.* (1990), Cho *et al.* (1991) and Pearton *et al.* (1987) for example). Along with its ability to react with both negative and positive charge centres its size and mass make it ideal for introduction into a host semiconductor lattice where it may react with ionised donors and traps, electrically passivating them without disturbing or damaging the periodicity of the lattice.

8.6.2 How Hydrogen is Introduced into Semiconductor Materials

Hydrogen can be introduced into semiconductors either during crystal growth, by direct implantation, exposure to a hydrogen plasma, or by chemical reaction at the surface. In some cases atomic hydrogen may be unintentionally incorporated into the near-surface region ($\leq$ 1μm) of samples during simple cleaning or fabrication processes. The controllable introduction of atomic hydrogen can be achieved using a hydrogen plasma system. This generally consists of a quartz tube through which molecular hydrogen is drawn at a reduced pressure

(0.1–0.3 torr). The plasma is excited either by inductively coupling radio–frequency (13.56 MHz) radiation (see Pearton *et al.*, Paccagnella *et al.* (1989) & Cho *et al.* (1991) for example) or by a dc discharge (see Conibear *et al.* (1993) for example). The sample is normally held at temperatures between 100 - 400 °C and exposed to the plasma for 2–5 hours. Pearton *et al.* (1987) reported that the passivation of electrical activity in semiconductor materials depends very weakly on the plasma power.

8.6.2 The States of Hydrogen in Semiconductor Materials

There are many investigations which identify the state of hydrogen in *p*-type and *n*-type semiconductor materials. Hydrogen can exist in a semiconductor in a variety of states such as H^+, H^-, or H^0. In Si for example the hydrogen ion has a positive charge H^+ (a donor state) in *p*-type (Tavendale *et al.* (1985)) and a negative charge H^- (an acceptor state) in *n*-type (Liu *et al.* (1991)). While Pearton *et al.* (1985) have observed the neutral state of hydrogen (H^0) in Si. In GaAs it has been observed that the hydrogen ion can be either neutral (H^0) or negatively charged (H^-) in *n*-type material (Yuan *et al.* (1991), Leitch *et al.* (1991)) and as positively charged (H^+) in *p*-type material (Tavendale *et al.* (1990), Cho *et al.* (1991)).

8.6.4 Deep & Shallow Level Passivation

As mentioned earlier, the incorporation of atomic hydrogen into semiconductors causes significant changes in their electrical and optical properties due to passivation of the electrical activity of dangling or defective bonds, deep defects and impurity states as well as dangling bonds at unreconstructed surfaces (Pearton *et al.* (1987)). Changes in the electrically active dopant profile in the near-

surface region by hydrogen passivation have been reported by Pankove *et al.* (1985), Pearton *et al.* (1986,1987), Leitch *et al.* (1991), Paccagnella *et al.* (1989), Cho *et al.* (1991), Yuan *et al.* (1991), and Liu *et al.* (1991). In Si for example, many of the electrical levels introduced by contaminating metal-related centres can be neutralised by reaction with atomic hydrogen including deep & shallow donor and acceptor levels (Pearton *et al.* (1987)).

Deactivation of deep level donors or defects is also being investigated by many researchers (see Kim *et al.* (1992) and Pavesi *et al.* (1991) for example). In GaAs atomic hydrogen is known to be able to passivate many types of deep and shallow levels. For example in undoped Liquid Encapsulated Czochralski (LEC) grown bulk GaAs the main defect is the EL2 centre which is also known as the As antisite (As_{Ga}) related defect. This defect has energy level at E_C–0.83 eV and concentration ~10^{16} cm^{-3} and can compensate shallow level impurities turning GaAs into a semi-insulating material (Pearton *et al.* (1987)). EL2 can be passivated by atomic hydrogen. However, annealing it at ~400 °C restores its activity. Table 9.1 shows some common levels in bulk, polycrystalline or liquid phase epitaxy GaAs that can be passivated by atomic hydrogen (Pearton *et al.* (1987)).

Beside its ability to passivate deep levels in semiconductor materials the ability of atomic hydrogen to suppress the electrical activity of shallow impurity levels (acceptors or donors) in Si, GaAs and AlGaAs is also well established (Pearton *et al.*(1987), Cho *et al.* (1991)). This passivation is induced by the bonding of the H atom to the dopant, with the formation of a neutral hydrogen-impurity complex.

Impurity/levels	E_a [eV]
EL2, E(0.83)	2.5
LPE, E(0.13, 0.38, 0.54, 0.73)	2.2
LEC, E(0.16, 0.24, 0.36)	2.2
Poly, E(0.36)	1.9
Grain boundaries	2.1
Sputtering etching	2.0
MBE, E(0.17, 0.28, 0.45)	2.9
Si, S, Se, Te, Sn, Ge	2.1
Zn, Cd, Mg, Be	1.6

Table 8.1 : Impurities or defects in GaAs susceptible to hydrogenation, and the corresponding energy levels. E_a denotes the activation energy for reactivation of the electron trap. E refers to the depth of the electron trap. (After Pearton *et al.* (1987)).

In *p*-type GaAs the hydrogen will be in an ionised state

$$H^0 + h^+ \rightarrow H^+ \qquad (8.26)$$

The acceptor passivation then takes the form

$$H^+ + A^- \rightarrow (AH)^0 \qquad (8.27)$$

While the donor passivation is due to the formation of H–donor bond which utilises the extra electron from the donor :

$$D^+ + e^- + H^0 \rightarrow (DH)^0 \qquad (8.28)$$

For example in Si doped *n*-GaAs donor passivation will then occur by a reaction of the type (Pearton *et al.* (1987), Cho *et al.* (1991))

$$H^0 + Si^+ + e^- \rightarrow (SiH)^0 \qquad (8.29)$$

Pearton *et al.* (1987) observed an increase in the electron mobility in *n*-type samples upon hydrogenation which is attributed to the transformation of ionised donors into neutral complexes. Figure 8.12 shows some possible bonding models for the neutralisation of three different dopants in GaAs. In cases (a) and (b) the donor-hydrogen bond utilises the extra electron from the donor. For the case of acceptors, neutralisation could only occur by bond rearrangements (Figure 8.12(d)).

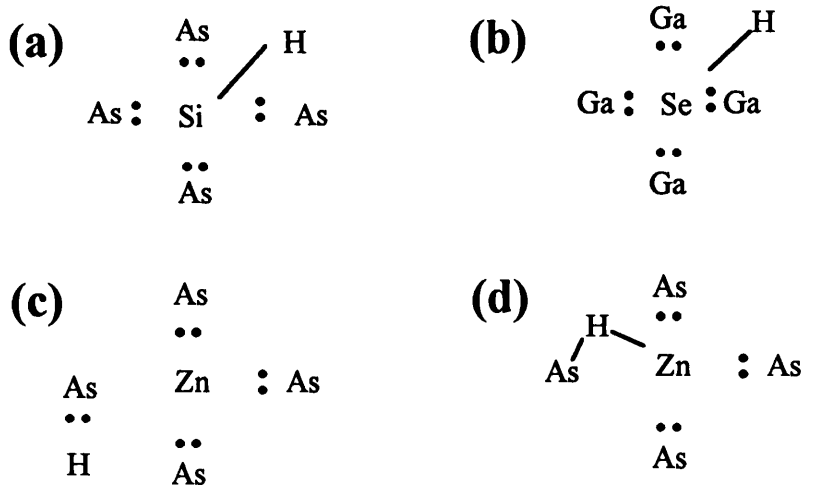

Figure 8.12: Possible microscopic bonding models for donor neutralisation in (a) Si-doped, (b) Se-doped, (c) & (d) Zn-doped GaAs. (After Pearton *et al.*(1986)).

It has been reported that a consequence of hydrogen passivation is that the carrier concentration in the near-surface region is strongly reduced, with the depth

of this modification being inversely proportional to the initial doping level and the square root of the plasma exposure time (Pearton *et al.* (1987)). The passivation depth is dependent on the densities of sites to which the hydrogen can bond, and the sample temperature, but depends only weakly on the plasma power and pressure under normal conditions. Cho *et al.* (1991) have reported that donor impurities were passivated to a depth of 0.35 μm in Si-doped *n*-type GaAs. This is supported by Yuan *et al.* (1991) who also observed a passivation depth around 0.3μm for Te-doped *n*-type GaAs.

8.6.5 Surface Passivation and Unpinning of Fermi Level

Fermi level pinning in GaAs which was mentioned in the last chapter is mainly due to the high density of surface states in the gap. Lee *et al.* (1988) suggested that these surface states are mainly formed by segregated atoms via oxidation reactions. (The true mechanism behind the formation of the surface states is still under discussion). The presence of oxygen causes the oxidation of GaAs to arsenic oxide and gallium oxide. Subsequently gallium atoms in the vicinity of the arsenic oxide gradually extract oxygen from it forming gallium oxide and leading to the segregation of arsenic atoms. Therefore according to this theory if free As at the GaAs surface could be passivated by atomic hydrogen the surface Fermi level might be unpinned, leading to the modification of the Schottky barrier height. Pre treatment of the GaAs surface before metalisation should remove this excess As which is present either in elemental form or as As_2O_3 by the reactions

$$As + 3H \rightarrow AsH_3 \uparrow \qquad (8.24)$$

$$As_2O_3 + 12H \rightarrow 3H_2O + 2AsH_3 \uparrow \qquad (8.25)$$

The unpinning of the Fermi level by hydrogen passivation has been reported by Pearton *et al.* (1984).

8.6.6 Types of Measurement on the Effect of Hydrogenation

The passivation profiles can be estimated by a large number of methods. Among those commonly used are C-V carrier profiling, Secondary Ion Mass Spectroscopy (SIMS) or photoluminescence spectroscopy and Deep Level Transient Spectroscopy (DLTS). Pearton *et al.* (1982) demonstrate in DLTS measurements that the capacitance of Au-diffused n-type Si sample is lowered with hydrogenation. For the same sample they also measured the variation in concentration profile with depth from the sample surface with hydrogenation. Tavendale *et al.* (1985) have made a similar measurement for B-doped Si samples at temperatures between 80 - 150 °C and various exposure times. Pankove *et al.*(1985) demonstrated that the effect of hydrogenation can also be investigated using SIMS profiles on B-doped Si. I-V and C-V measurement on Schottky diodes have also been used by Ashok *et al.* (1990) to investigate the effect of hydrogenation on the barrier height.

Surface passivation of semiconductors has also been achieved using different atomic species other than hydrogen (Chambers *et al.* (1991) and Lee *et al.* (1988)). Chambers *et al.* (1991) used X-ray photoelectron spectroscopy (XPS) and low-energy electron diffraction (LEED) to study the chemical, structural, and electronic properties of surfaces of GaAs due to passivation by group VI atoms (Se and Te). Lee *et al.* (1988) have also successfully passivated the surface of *n*-type GaAs by treating it with P_2S_5 /NH_4OH. This technique avoids the formation of Ga_2O_3 which leads to As segregation due to the higher heat of formation of phosphorus oxide compared to Ga_2O_3.

Electric fields established in reverse biased Schottky diodes either after or during hydrogenation lead to dramatic changes in passivated acceptor profiles. However, one thing should be remember as reported by Cho *et al.* (1988) and Jalil *et al.* (1989) that apart from the passivation of unwanted electrically active defects a hydrogen plasma can also create deep levels.

CHAPTER 9

Passivation of Schottky Contacts: Experimental Procedures and Results

---

9.1 Introduction

The unique aspect of this work is the fact that Pd contacts were deposited on the sample surface prior to the hydrogenation process. This is feasible because Pd is known to be highly transparent to atomic hydrogen (Dembovsky (1984)). In this method the sample surface is not exposed to air and no new oxide is produced at the interface. In all other works (Sharda *et al.* (1991), Kim *et al.* (1992), Ashok *et al.* (1990) and Pacagnella *et al.* (1989) for example) GaAs is passivated first then exposed to the air before a Schottky contact is deposited on the top.

9.2 Sample Fabrication

9.2.1 Sample Cleaning

The GaAs wafers used for the Schottky diode fabrication in this work were supplied by Mining & Chemical Products (MCP) Wafer Technology Ltd. They were grown by the Bridgman method with the substrate oriented 3° off (100) towards [011]. The crystal was degenerately doped with Si with doping density, N_d in the range 1.6 – 5.3x10^{18}cm^{-3}. The wafer was first degreased by soaking it in trichloroethylene or toluene for 5 minutes. It was then ultrasonically cleaned in acetone for 5 minutes followed by isopropyl alcohol for 5 minutes. Finally it was rinsed for 5 minutes in boiling isopropyl alcohol. The samples were then blown dry with a stream of nitrogen gas and inspected under a microscope for cleanliness. If it was necessary, this procedure was repeated to make sure the samples were thoroughly clean. Prior to metallisation an ohmic contact was made on the back of the wafer with a AuGeNi eutectic alloy. Thermal evaporation of Ge (445 Å), Au (1350 Å), and Ni (200 Å) was performed sequentially using W boats and the completed contact was annealed in a N_2:(5%)H_2 reducing gas environment at a temperature of 430 °C for 40 seconds. The 2 in. wafer was then cleaved into 4 mm x 4 mm chips for diode fabrication.

9.2.2 Metal Deposition

Each chip was cleaned using the same procedure as above, glued onto a microscope slide with a thin layer of photoresist and baked at 95 °C for 5 minutes. Diodes of radii between 20 μm - 100 μm were then patterned using conventional photolithography and electron beam evaporation. A thin layer of photoresist (~ 1 μm thick) was spun onto the chip at 4000 r.p.m for 2 minutes. This was then baked

at 95 °C for 30 minutes, exposed in a mask aligner, developed and rinsed in de-ionised water. Just before loading into the evaporation chamber each sample was etched with the following etchants for 60 seconds :

a) samples A - D with 1:1 $HCl:H_2O$

b) sample E with H_2SO_4

This was designed to remove native oxide just prior to loading into the vacuum system. The two different etch solutions were compared to see if they yielded a different surface preparation. Each sample was then rinsed with de-ionised distilled water for 60 seconds and blown dry with N_2 gas. Pd metal was evaporated at a background pressure ~ 10^{-5} mbar and substrate temperature ~80°C. Due to its high melting point (1552 °C) the Pd contacts were deposited using electron beam evaporation which normally produces a better quality thin film layer. Prior to loading into the vacuum system, the metal was thoroughly cleaned with organic solvents. During evaporation the deposition thickness was monitored with an oscillating crystal thin film thickness monitor. A more accurate measurement was made later on with a Tallystep surface profiler. The Pd-coated samples were then exposed to a hydrogen plasma for 5 hours at the required temperature. To facilitate wire bonding the Pd layer was subsequently coated with a Ti-Au overlayer. This metal overlayer was made by successive thermal evaporations from separate W boats in one pump-down cycle without breaking vacuum. A Ti layer of about 500 Å was evaporated first to act as a wetting agent and a thicker gold bonding layer of about 1500-2000 Å followed.

9.2.3 Hydrogen Passivation

Figure 9.1 shows the capacitively coupled hydrogen plasma passivation system which was constructed to perform these experiments. It comprises two semihemispherical aluminium H.T. electrodes, 5 cm in diameter, enclosed in a horizontal quartz tube. A temperature controlled sample holder was positioned about 10 cm downstream of the electrodes. The quartz tube was first evacuated to a pressure of about 0.05 torr to remove all traces of oxygen in the tube. It was then flushed with nitrogen gas for about 15 minutes before hydrogen was fed in. A small constant flow of hydrogen was controlled by a needle valve to achieve a hydrogen pressure of about 0.3 – 0.4 torr at the pumped end of the system. When a ~ 400 V DC voltage was applied across the electrodes a hydrogen plasma was struck emitting a purplish glow (Pearton *et al.* (1986)).

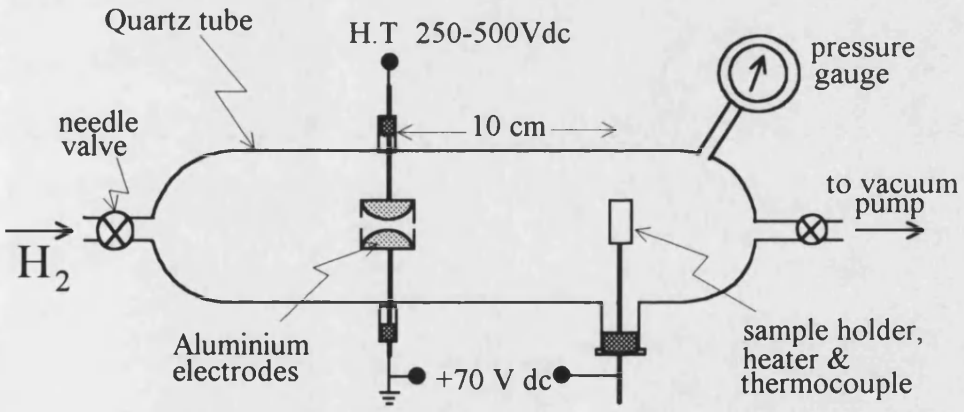

Figure 9.1 : Schematic diagram of DC plasma system used for hydrogen passivation of Schottky diodes.

At the same time a +70 V DC bias was also applied to the sample holder. This voltage draws charged radicals from the plasma which impinge on the sample and diffuse into the bulk of the material as well as preventing a plasma being struck between sample holder and electrode. In this way any surface barriers to the penetration of hydrogen can be lowered. In our experiments the samples were exposed to the plasma for 5 hours while maintaining the temperature fixed in the range 20 - 200 °C.

9.3 I–V Measurements

I–V curves were measured on each sample at atmospheric pressure and temperatures of 8 K and 77 K using a cryogenic closed-cycle refrigerator. Measurements at large hydrostatic pressures were only performed at 77 K using the pressure cell described in Chapter 4. Details of the I-V measurement apparatus have been given in Chapter 5. Plots of I-V and $\ln(R/R_o)$-V (where R = dV/dI) were then made for each measurement. Barrier heights and mean doping densities were obtained by fitting the self-consistent theoretical plots of $\ln(R/R_o)$-V to the experiment. In this thesis the following results are presented; (a) Hydrogen Passivation of Electron Beam Evaporated Pd Diode Samples, (b) The influence of Hydrostatic Pressure on the Schottky Diode Characteristics.

9.4 Experimental Results and Discussion of Electron Beam Evaporated Diodes

Figure 9.2 shows the rectifying I–V characteristics of four different samples (A - D) for Schottky diodes of diameter 300 μm at ambient pressure and 8 K.

Sample A is a control which was put in the chamber at 20 °C for 5 hours without a hydrogen plasma. Samples B - D were exposed to the hydrogen plasma for 5 hours at 20 °C, 100 °C and 200 °C respectively. From Fig. 9.2 it can be seen that the current density decreases when the sample is exposed to the hydrogen plasma for 5 hours at 20 °C compared to the unhydrogenated control. A further reduction is observed when the hydrogenation temperature is increased to 100 °C. However, as the temperature is raised to 200 °C the current density increases dramatically to a higher value than the untreated sample A.

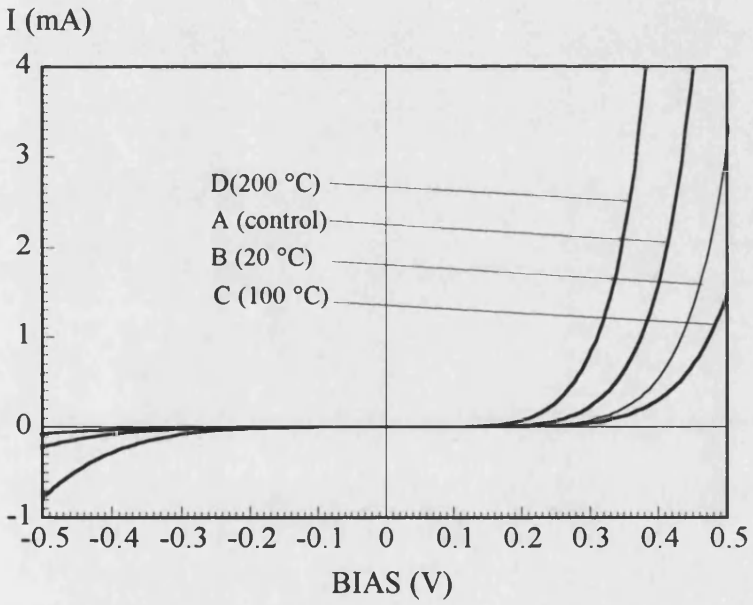

Figure 9.2 : Typical I-V characteristics of samples A, B, C, and D.

Figures 9.3 (a) – (d) show log plots of the normalised resistances ($^{dV}/_{dI}\big|_V$ divided by $^{dV}/_{dI}\big|_{V=0}$) versus bias voltage of the same data shown in Fig.9.2. The best fit calculated from the self–consistent model is superimposed in each plot. For our theoretical model we find that the forward bias region of plots of this type is nearly linear and its gradient is almost independent of the barrier height. The shape of the

curve in the reverse bias region and the gradients in both bias directions are, however, very sensitive to the doping density. We find that the shape of the forward bias curves for the experimental data show a consistent sublinear deviation from the theory. The origin of this forward bias non-ideality probably lies in the formation of oxide layer at the interface.

In order to fit the theoretical calculation to the experimental data, we employ two methods. The first involves measuring the gradient of the steepest slope under forward bias which can be converted to an approximate doping density using equation 8.13. Assuming this doping density we obtained the best fit for the barrier height in the reverse bias region. The reason for the strong non-ideality of our measured I-V's is not fully understood. As explained above the theoretical model yields forward bias resistances which depend strictly exponentially on V and are almost independent of the barrier height. In contrast plots of ln(R/Ro) for our samples show pronounced non-linearity in the forward bias region. It was difficult to describe experimental plots with the theoretical model. It was, however, possible to get good agreement in reverse bias for both fitting methods. When the fits are optimised different barrier heights and mean doping densities are obtained for each set of experimental parameters (Fig. 9.3).

In the second procedure we have fixed the value of barrier height for all samples to 0.8 eV (the value for unpassivated Pd/*n*-GaAs (Costa *et al.* (1991))) and fitted the value of the doping density in the reverse bias region. These are shown in Fig. 9.4. Table 9.1 summarises the results of the fitting procedure. R_0 is the experimental resistance of the sample at zero bias which is used to calculate values of ln (R/R_0) in Figs. 9.3 and 9.4.

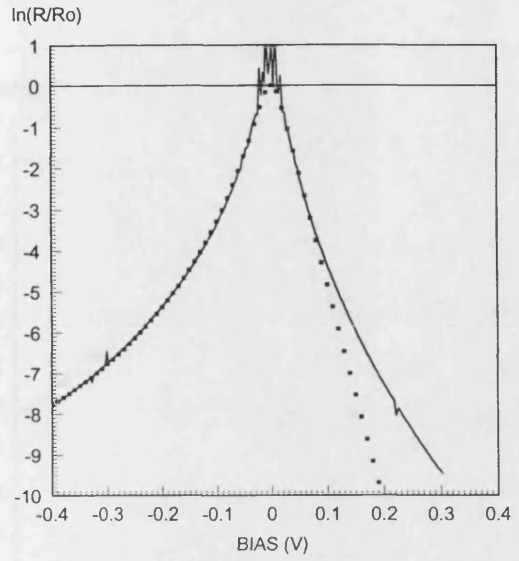

SAMPLE A

Φ_B = 0.44 eV; N = $8.0 \times 10^{17} cm^{-3}$

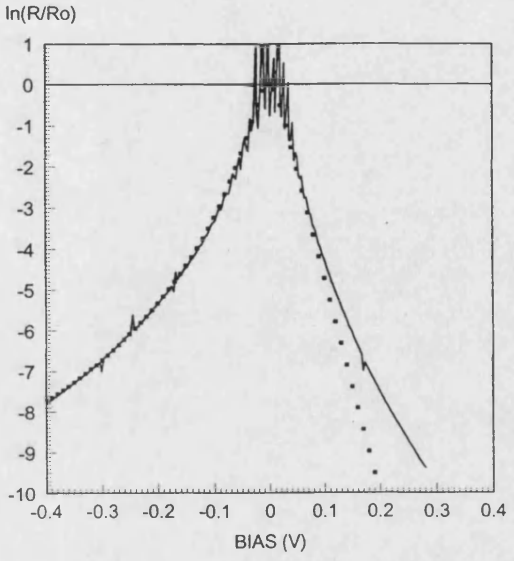

SAMPLE B

Φ_B = 0.45 eV; N = $8.3 \times 10^{17} cm^{-3}$

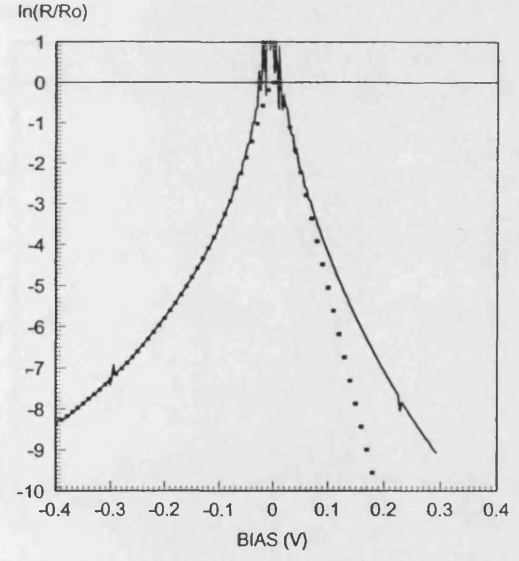

SAMPLE C

Φ_B = 0.46 eV; N = $7.4 \times 10^{17} cm^{-3}$

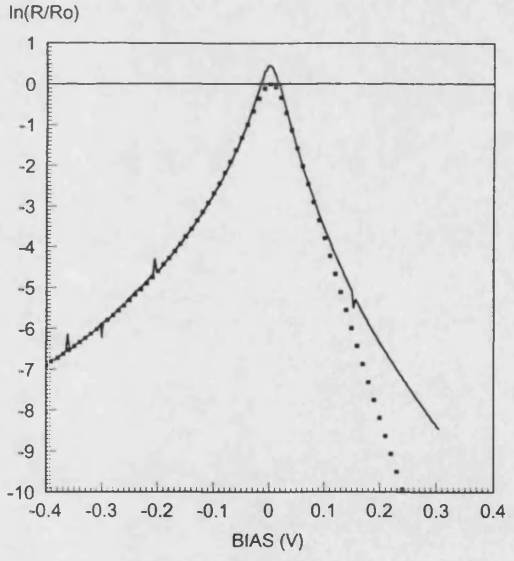

SAMPLE D

Φ_B = 0.53 eV; N = $1.2 \times 10^{18} cm^{-3}$

Figure 9.3 : Plot of ln (R/R_o) of samples A - D under different hydrogenation conditions superimposed upon the self-consistent model using method 1.

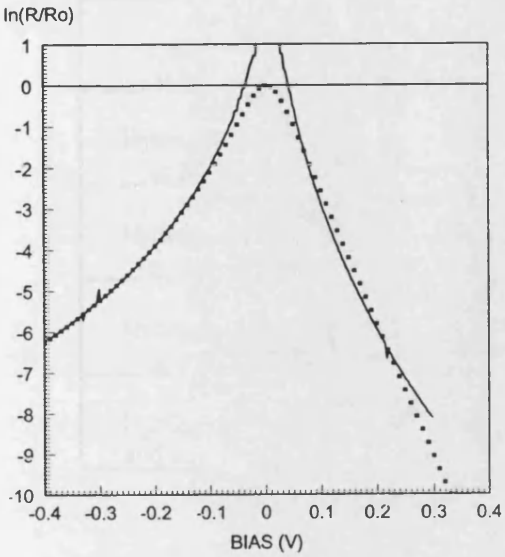

SAMPLE A

Φ_B = 0.8 eV; N = 2.21x10^{18}cm^{-3}

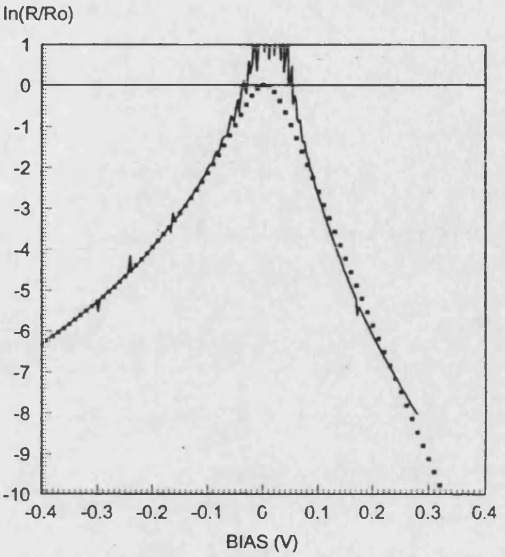

SAMPLE B

Φ_B = 0.8 eV; N = 2.18x10^{18}cm^{-3}

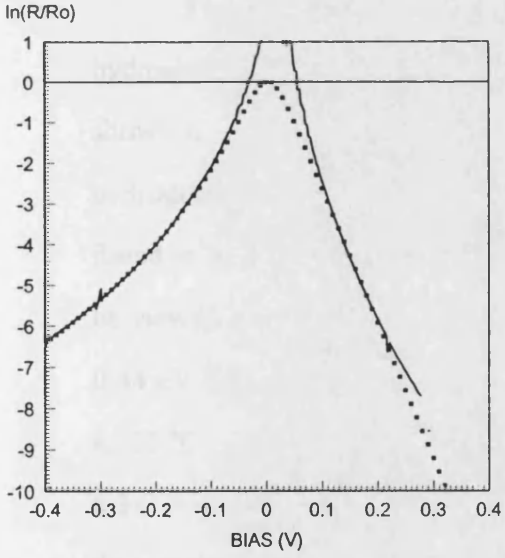

SAMPLE C

Φ_B = 0.8 eV; N = 2.14x10^{18}cm^{-3}

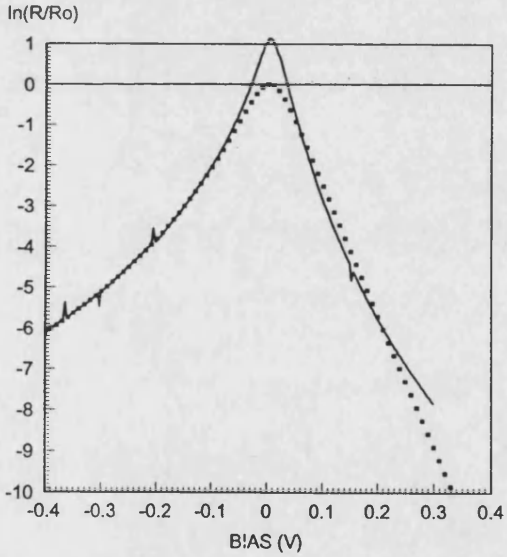

SAMPLE D

Φ_B = 0.8 eV; N = 2.28x10^{18}cm^{-3}

Figure 9.4 : Plot of ln (R/R_o) of samples A - D under different hydrogenation condition superimposed upon self-consistent model using the second method. The barrier heights are fixed to 0.8 eV for all samples.

	R_0 (±0.1) kohms	Φ_B (±0.005) eV	N (±0.01x10^{17}) cm^{-3}	N (Φ_B= 0.8eV) (±0.01x10^{17}) cm^{-3}
A untreated at 20 °C	65.8	0.44	8.00	22.10
B Hydrogenated at 20 °C	100.8	0.45	8.30	21.80
C Hydrogenated at 100 °C	21.1	0.46	7.40	21.40
D Hydrogenated at 200 °C	10.7	0.53	12.00	22.80
E H_2SO_4 etched and untreated	48.2	0.49	9.70	23.0

Table 9.1 Results of data fitting of barrier height and impurity density for all samples at 8 K.

Four different parameters are summarised in Table 9.1 as a function of the hydrogenation conditions. The barrier height that we obtained using method 1 shows a monotonic increase in the Schottky barrier height as the sample is hydrogenated at progressively higher temperatures. Note that due to the difficulty found in fitting these non-ideal I-V characteristics these barrier heights should only be viewed as a measure of the true barrier height. This is found to increase from 0.44 eV for the unpassivated sample to 0.45 eV when the sample is hydrogenated at 20 °C while the mean doping density increases a little from $8.0x10^{17}cm^{-3}$ to $8.3x10^{17}cm^{-3}$. The barrier height then increases further to 0.46 eV and the doping density reduces to $7.4x10^{17}cm^{-3}$ at 100 °C . The highest barrier height is observed for the sample which was passivated at 200 °C which is 0.52 eV but the doping density also increases sharply to $1.2x10^{18}cm^{-3}$. At the same time we see that R_0 initially increases from 65.8 kohms to 100.8 kohms when the sample is hydrogenated at 20 °C but drops dramatically at higher passivation temperatures. In Fig. 9.4 in the second method of fitting, when the barrier height is fixed to 0.8

eV we see a drop in the doping density from $2.21 \times 10^{18} cm^{-3}$ to $2.14 \times 10^{18} cm^{-3}$ when the samples are hydrogenated up to 100 °C. This is in agreement with the decrease in the current density as shown in Fig 9.2. However, the doping density suddenly increased to $2.28 \times 10^{18} cm^{-3}$ when it was hydrogenated at 200 °C yielding the highest current density in Fig. 9.2.

The reduction in current density with passivation in Fig. 9.2 appears to arise from an increase in the Schottky barrier height from 0.44 eV to 0.46 eV. This may come about as hydrogen ions bond to surface/defect states at the metal-semiconductor interface reducing the state density and partially unpinning the Fermi level. Note that pinning in GaAs normally fixes the Schottky barrier heights at around 0.8 eV for Pd/*n*-type GaAs (Costa *et al.* (1991)). Assuming no surface states and setting χ(GaAs) = 4.07 eV, ϕ_m(Pd) = 4.97 (Blakemore (1987)) the Schottky barrier height in the Schottky-Mott limit is about 0.9 eV.This would be in line with increased barrier height we measure upon passivation.

As the temperature is raised it is plausible that more hydrogen ions bond to the surface/defect states causing a further unpinning of the Fermi level. Although there is an increase in the barrier height of sample D the simultaneous increase in mean impurity density (see Table 9.1) leads to a net increase of the current density in Fig.9.2. The dramatic changes for this sample are probably due to reactions at the interface or the diffusion of Pd into the GaAs surface as it was heated at 200 °C for 5 hours. Kahen (1991) noted that Pd has the unique property of promoting As expulsion to the top of the Pd overlayer. Sharda *et al.* (1991) reported a barrier height reduction for untreated Pd/*n*-GaAs Schottky diodes when they were annealed at temperatures > 160 °C which they attributed to this effect, but was not observed in this work.

Kim *et al.* (1992) have reported an increase in the barrier height from 0.83 eV (untreated) to a value > 0.9 eV (passivated before the contact was deposited) for Au/*n*-GaAs Schottky contacts at about 150 °C. However, the barrier height dropped again at higher temperatures. They attributed the increase in the barrier height to the neutralisation of Si donors near the surface. When this happens the Fermi level at the surface falls below the Fermi level of the bulk material. The neutralisation depth was found to increase with increasing temperature which in turn further increased the barrier height.

On the other hand Ashok *et al.* (1990) have reported a reduction in barrier height from 0.8 eV for untreated samples to 0.59 eV for hydrogenated Au/*n*-GaAs Schottky contacts and an increase from 0.35 eV to 0.84 eV for Au/p–GaAs. The samples in this case were again passivated before the Schottky contacts were made. They attributed both of these changes in the barrier height to the creation of donor–like defect levels at the surface. In *n*-type GaAs the resulting positive surface charge in a shallow surface layer then causes an effective reduction of the Schottky barrier height. Paccagnella *et al.* (1989) also reported an increase in the passivation depth and barrier height of Ti/Pt –*n*-GaAs Schottky contacts with hydrogenation temperature from ~0.52 at ~60 °C to ~0.72 eV at ~200 °C. As in the case of Ashok *et al.* (1990) and Kim *et al.* (1992) these samples were passivated before contact deposition process.

The general trend for the mean impurity density to decrease up to 100 °C is consistent with a passivation mechanism whereby neutral H-donor complexes are formed (Eq. 8.23) as also reported by Chung *et al.* (1983) for Si doped GaAs. The increase in the 200 °C sample is almost certainly due to additional reaction or diffusion at the Pd/GaAs interface.

Table 9.1 also shows results obtained for the unhydrogenated sample E which was etched with H_2SO_4 immediately before loading into the evaporation chamber while Fig. 9.5 shows the experimental curves and fits to the self-consistent model superimposed. Its barrier height and impurity density are higher than sample A and R_0 is somewhat lower. This may be due to a reduction of the surface state density caused by atomic segregation during oxidation reactions on the surface as explained in Chapter 8.

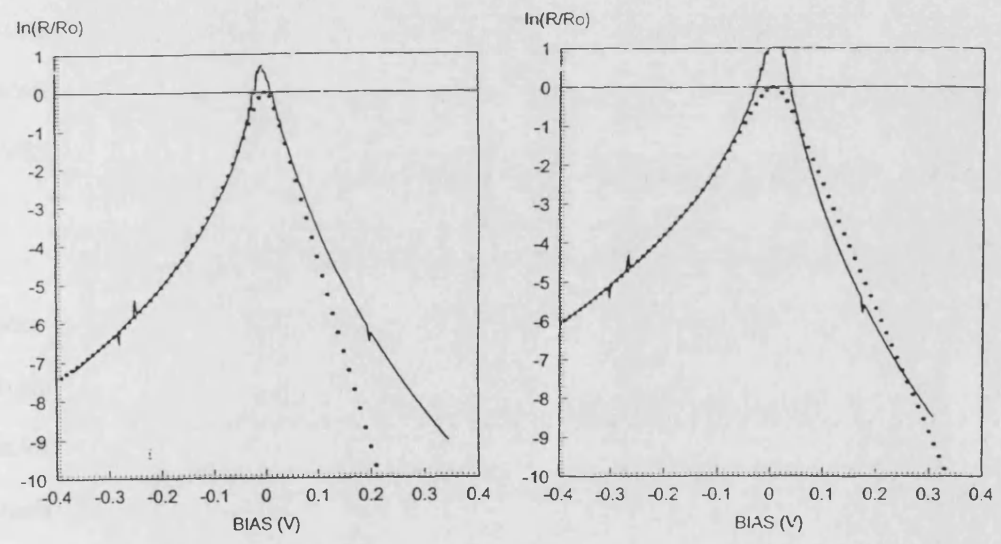

Figure 9.5 : Plot of ln (R/R_o) of sample E which was etched with H_2S0_4 superimposed with self-consistent model (a) with first method, and (b) with the second method.

9.5 The Influence of Hydrostatic Pressure on Schottky Diode Characteristics

9.5.1 Introduction

Little is known about the pressure dependence of the Schottky barriers. Ping *et al.* (1993) made a theoretical calculation of the effect of uniaxial stress on the band-structure of the (001) GaAs surface. The theory was discussed in terms of ideal and 2x1 reconstructed surfaces. The bulk energy band gaps can be seen to increase, while the surface-energy band gap decreases as the pressure is raised. From Table 3.3 we see that there is an increase in the bulk energy band gap of about 11.5 meVkbar^{-1} when hydrostatic pressure is applied to GaAs (Adachi (1985)).

Theoretical and experimental work which relates more closely to ours has been undertaken by Schilfgaarde *et al.* (1994). They see a change in the barrier height of Pt/GaAs which depends on the condition of the GaAs surface. For *p*-GaAs which contains antisite disorder they found that $d\Phi_B/dp$ =1.7 meV/kbar which reverses to -0.6 meV/kbar without antisite disorder. They also find the pressure coefficient of the GaAs energy band gap to be 9.8 meVkbar^{-1}. Shan *et al.*(1988) showed experimentally that $d\Phi_B/dp$ = 11 meV/kbar for Pt/n-GaAs. Due to a change in the band gap energy we should expect to see a change in the effective masses (m*) of carriers. This change is small and often ignored (Mendez *et al.* (1986), Austing *et al.* (1990), Bonnefoi *et al.* (1987), Othaman *et al.* (1991)). In addition Si-donor binding energies, H-Si complex binding energies, and the surface state can also change on application of pressure.

9.5.2 Result and Discussion

Figure 9.6 shows the 77K I–V characteristics of sample A (untreated) at different applied pressures. There is a monotonic decrease in current with applied pressure. However, this change can be normalised out in the $\log(R/R_o)$ plot of Fig. 9.7 implying there is no measurable change in the barrier height or the mean impurity density of the sample under hydrostatic pressure. This same behaviour is also seen for sample C (hydrogenated at 100 °C) in Fig. 9.8 & Fig. 9.9 and sample D (hydrogenated at 200 °C) in Fig. 9.10 & Fig 9.11.

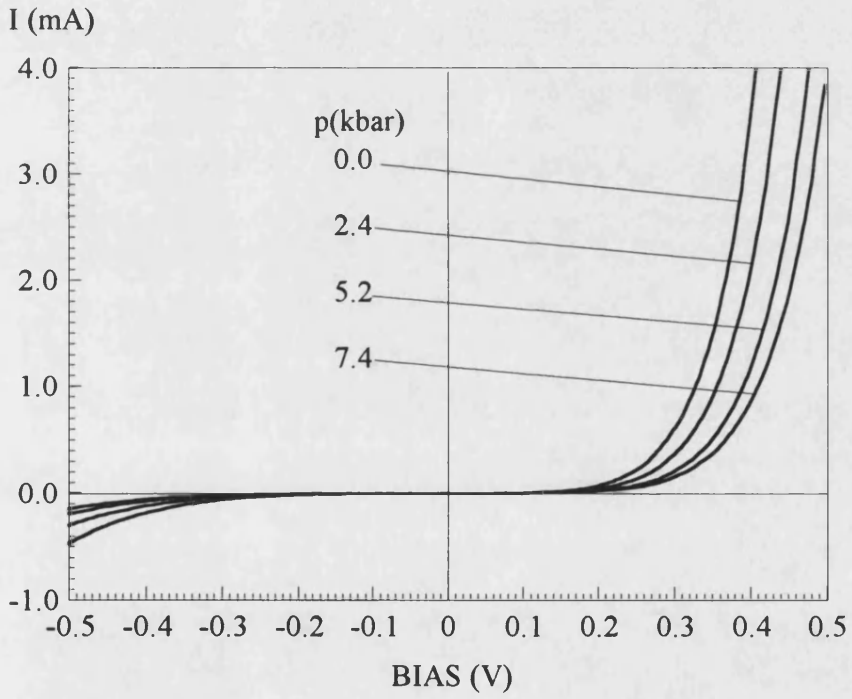

Figure 9.6 : I-V characteristics of sample A (untreated) at 77 K and different applied pressures.

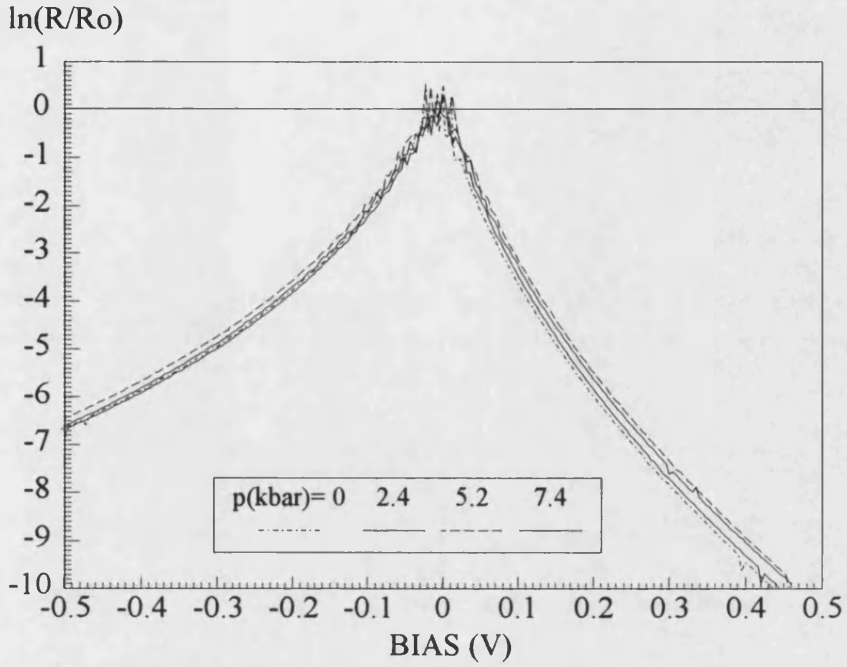

Figure 9.7 : Log of normalised resistance of sample A (untreated) at 77 K and different applied pressures.

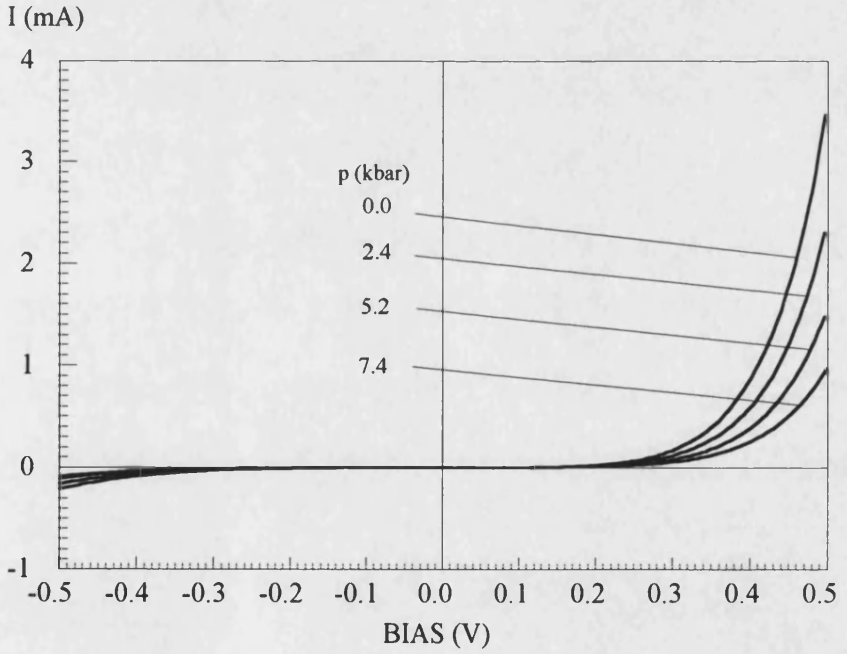

Figure 9.8 : I-V characteristics of sample C (hydrogenated at 100°C) at 77 K and different pressures.

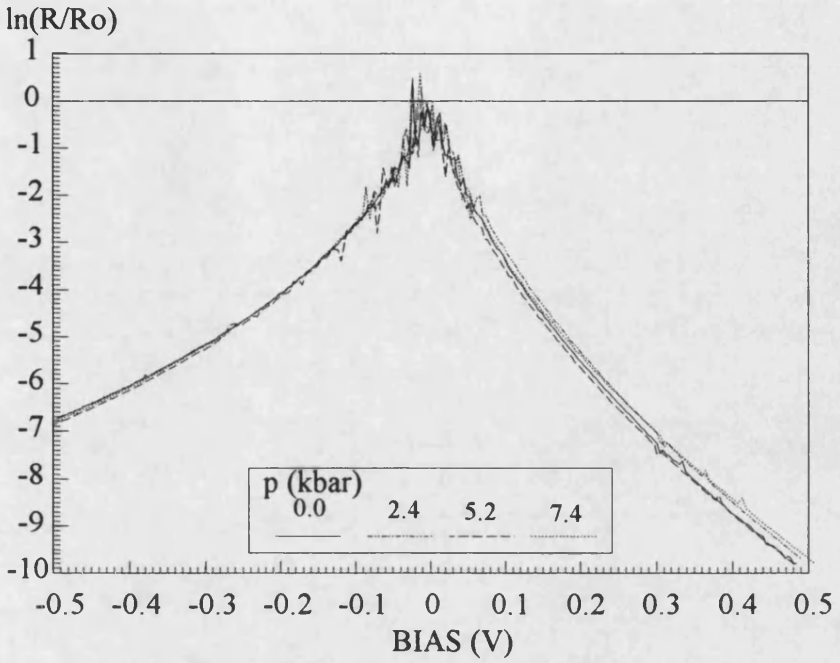

Figure 9.9: Log of normalised resistance of sample C (hydrogenated at 100°C) at 77 K and different pressures.

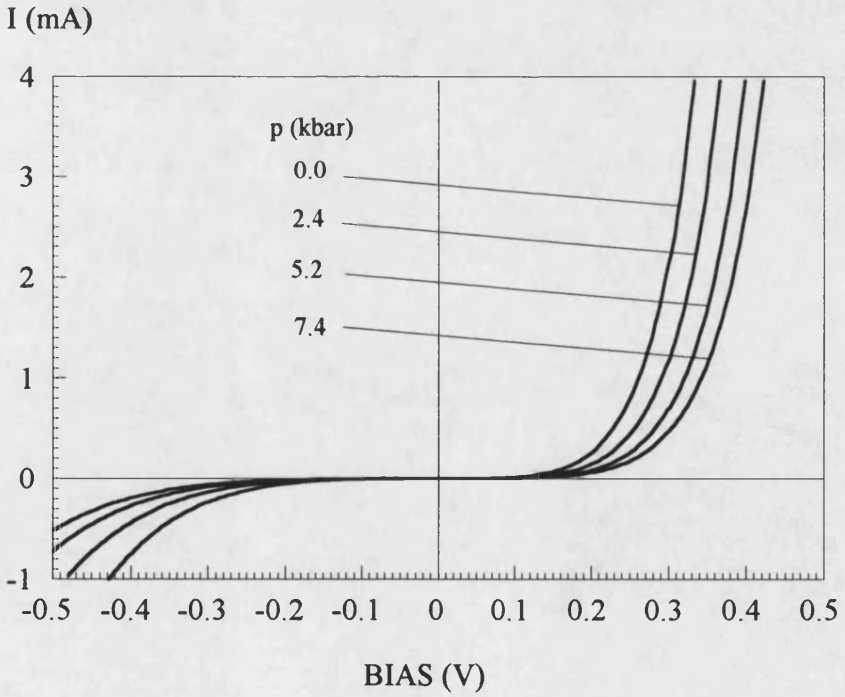

Figure 9.10: I-V characteristics of sample D (hydrogenated at 200°C) at 77 K and different pressures.

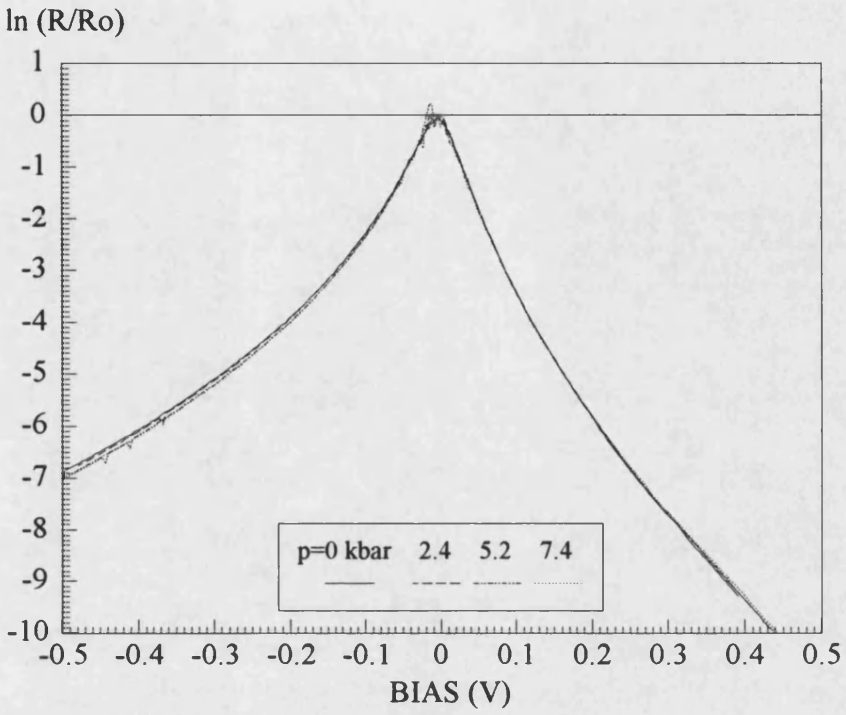

Figure 9.11: Log of normalised resistance of sample D (hydrogenated at 200°C) at 77 K and different pressures.

As mentioned above Schilfgaarde *et al.* (1994) calculate a very small change in barrier height i.e. between -0.6 meV/kbar (no antiside disorder) to 1.7meV/kbar (with antisite disorder) for Pt/p-GaAs. Their calculation using local density approximation (LDA) also yields the pressure dependence of the band gap and As antisite defect levels. For our maximum attainable pressure which is about 7.4 kbar, the change in our barrier height is only 12.58 meV. This is below the measurement sensitivity of our experiment. Clearly a better way of measuring changes in the barrier height is needed in order to clarify the experimental situation.

9.5 Conclusion & Future Suggestion

We have shown that treatment with a hydrogen plasma causes changes in the I–V characteristics of the Pd/n^+-GaAs Schottky diodes. An increase in the Schottky barrier height from 0.44 eV for untreated samples to 0.45 eV for a sample hydrogenated at 20 °C is observed. This barrier height is further increased to 0.46 eV when the hydrogenation temperature is increased to 100 °C. The highest barrier height (0.53 eV) is observed for a sample hydrogenated at 200 °C. However, the doping density has also increased quite sharply in this particular sample. The increase in the barrier height when the sample is exposed to the hydrogen plasma is attributed to the unpinning of the Fermi level as the surface or defect state density is reduced. Increasing the temperature increases the H mobility and causes a further reduction in the surface/defect state density and a coupled increase the barrier height. A decrease in the impurity density with passivation up to 100 °C is consistent with the formation of neutral H-donor complexes. At high pressure changes in the Schottky barrier height lie below the experimental measurement sensitivity. It is possible to supplement this work with other measurements such as thermionic emission, I-V and capacitance-voltage profiling. Due to the limited time available for this piece of work it only represents a preliminary survey of effects due to hydrogenation. A much more systematic investigation is now required to clarify a number of important questions which have been raised in this chapter.

APPENDIX A

Theory on Self-Consistent Calculation of a Single Barrier Structure

---

In Chapter 6 a comparison was made between experimental and theoretical peak and valley positions of the I-V characteristics. This self-consistent theoretical calculation was only performed for a single barrier GaAs/AlAs diode i.e. MBE sample DB1220. Figure A1(a) shows a typical doping profile of the sample. The conduction band profile of the sample for a small forward bias is illustrated in Fig. A1(b) with the zero energy taken as the bottom of the conduction band in the left electrode. Self-consistent solutions of the Poisson equation was then performed using

$$\frac{d^2\phi(x)}{dx^2} = \frac{e}{\varepsilon_r \varepsilon_0}\left[N_D^+ - n(x)\right] \qquad \text{A1}$$

where $\phi(x)$ is the electrostatic potential in the x-direction (perpendicular to the interface), N_D^+ is the density of ionised donors, $n(x)$ is the electron density, ε_1 is the dielectric constant of the semiconductor and ε_o is the permittivity of free space. The electronic charge is assumed positive to avoid a multiplicity of minus signs. An

initial solution of Poisson's equation is obtained using the Thomas-Fermi approximation i.e. $E(\mathbf{k}) = \hbar^2 k^2 / 2m^* - e\phi(\mathbf{r})$ so that

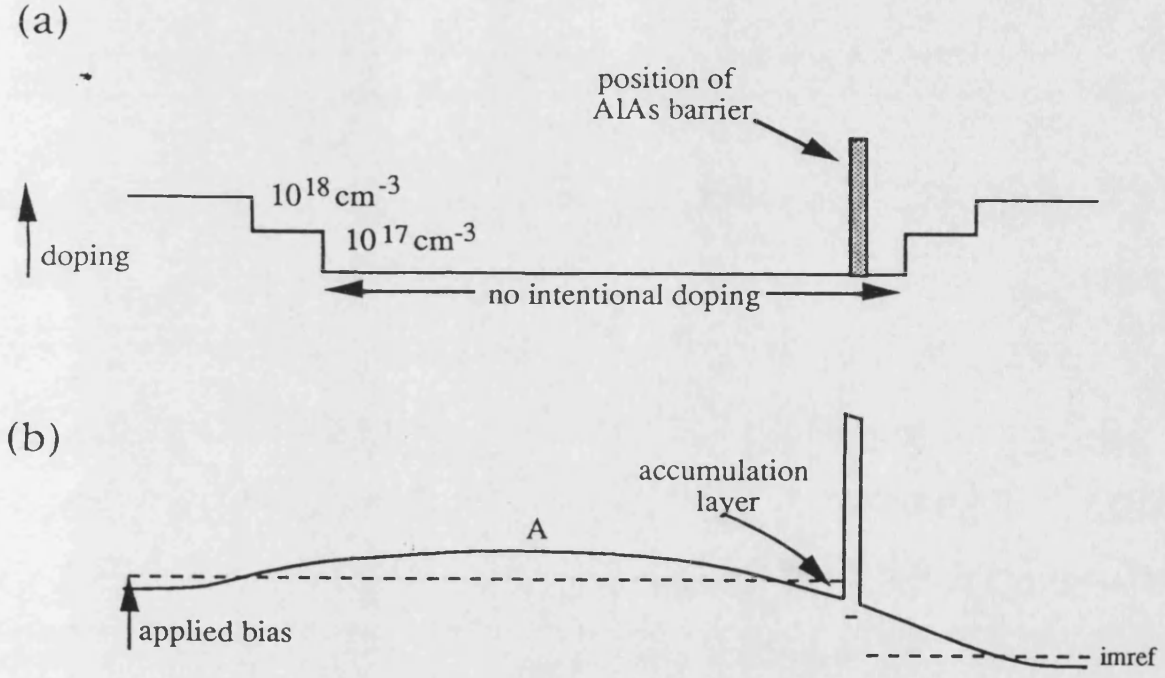

Fig A1 : (a) Typical doping profile; (b) Variation of conduction band edge under bias.

$$n(x) = \int_0^\infty g(E_x) f(E_x, E_F, \phi) dE_x \qquad \text{A2}$$

where

$$f(E, E_F, \phi) = \frac{1}{\exp\left(\left[E_x - (E_F - \phi)\right] / kT\right) + 1} \qquad \text{A3}$$

$$E_x = \frac{\hbar^2 k_x^2}{2m^*}$$

and $g(E_x)$ is the density of states. Equations A1 - A3 are solved using a finite difference method to get the initial potential profile.

The quasi-bound states in the accumulation layer are then found by calculating the transfer matrix connecting the wave function at point A in Fig A1(b) to the wave function in the AlAs barrier. A component of this transfer matrix goes to zero when the state is 'bound'. Therefore, if there is a sign change in this component of the transfer matrix between successive energies, there must be a bound state in that energy interval. The zero (and hence the bound state) is then determined by finding the zero point more accurately. The energy range searched is from the bottom of the accumulation layer to the maximum reached in the undoped region (i.e. the potential at point A in Fig. A1(b), denoted by ϕ_{max}). If there are many bound states, then the Thomas-Fermi approximation will not be a good one, and so the Poisson's equation needs to be solved again between point A and the barrier using the wave functions of the bound states to find n(z) in that region:

$$\left(-\frac{h^2}{8\pi}\frac{d}{dx}\frac{1}{m^*(x)}\frac{d}{dx} + \phi(E) \right)\Psi(x) = E_x\Psi(x) \qquad \text{A4}$$

The electron density is given by :-

$$n(x) = \sum_{E_x} \frac{|\Psi(E_x,x)|^2 f(E_x,E_F)}{\int |\Psi(E_x,x)|^2 dx} \qquad \text{A5}$$

$$f(E_x,E_F) = \frac{1}{\exp\left(\left[E_x - E_F\right]/kT\right)+1} \qquad \text{A6}$$

This process is repeated until the change between successive calculated values of ϕ is below some specified tolerance throughout the sample (e.g. 0.5 mV).

Once this quantum mechanically self-consistent potential profile has been obtained, the transmission coefficient through the structure for each bound level (from the accumulation layer to the collector contact) is calculated (again using a transfer matrix method), and the current density is obtained in the usual way by adding together the contributions from each bound state and the contribution from the continuum states (i.e. those electrons with energies greater than ϕ_{max}). Figure A2 and A3 show examples of reults of the program for a bias of 0.133 V, at 77 K and zero pressure.

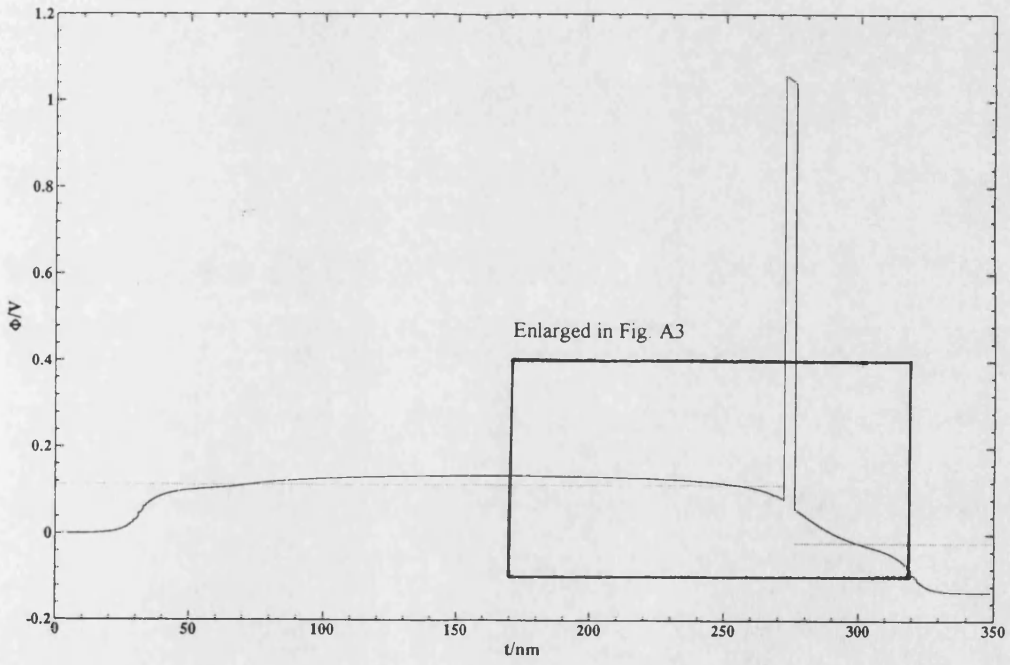

Fig A2 : Potential profile of sample DB1220 at forward bias 0.133V as simulated by Thomas Fermi method.

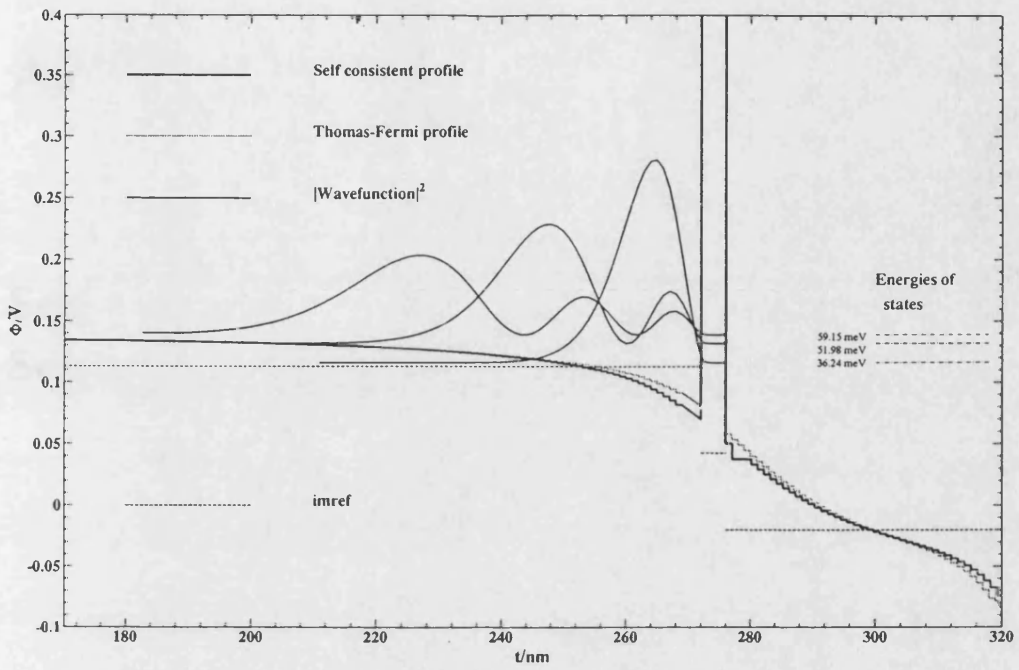

Fig A3 : Computer simulation of the potential profile of sample DB1220 near the barrier (outlined in Fig A2 above) at forward bias 0.133V and temperature 77 K.

APPENDIX B

Self-Consistent Simulation of I-V Characteristics Schottky Contact

---

```
      double precision phi,N,e,EN,ep,h,hcr,mu
      double precision fact,a,d
      double precision pi,ls,ltf,xo,xi,m,pfac,pho,q
      integer res
      integer choice,nev

      common /block1/ pi,h,hcr,ep
      common /block2/ mu,m,e,a
      common /block3/ phi,EN,fact,ls,ltf,xo,xi,pfac

c     physical constants.
c     ~~~~~~~~~~~~~~~~~~~
      pi = 3.14159265d0
      e = 1.6d-19
      h = 6.6d-34
      hcr = h/(2.0*pi)
      ep = 12.5*8.854d-12
```

```
      m = 0.067d0*9.1d-31
      pfac = 2.0d0*m*e/(hcr**2)
c     default parameters
      d = 2.5d-4
      a = pi*(d/2)**2
      pho = 0.8
      N = 4.0d24
      q = 2.0/3.0
      mu = ((3.0*pi*pi*N)**q)/pfac
      nev = 1000
      ltf = dsqrt(2.0*ep*mu/(3.0*e*N))
      ls = (dsqrt(3.0d0)/2.0)*ltf

      print *,'Tunneling probability as a function of electron energy'
      print *,'This subprog calculates values of D(E,k) and stores them'
      print *

c     input new contact parameters
      print *
      print *
3     print *,'          *** MENU ***'
      print *,'[1] change default semiconductor parameters'
      print *
      print *,'[2] produce an IV data'
      print *
      print *,'[3] produce an RV data'
      print *
```

```
print *,'[4] produce S(E), T(E) data'
print *
print *,'[5] produce R/Ro or log(R/Ro)'
print *
print *,'[6] display parameters'
print *
print *,'[7] exit'

print *
print *,'[option?]'
read *, choice
if (choice.eq.1) then
call edit(pho,N,nev)
end if
if (choice.eq.2) then
call sub4(res,N,pho,nev)
end if
if (choice.eq.3) then
call resis(res,N,pho,nev)
end if
if (choice.eq.4) then
call const(N,pho,nev)
end if
if (choice.eq.5) then
call sub6(res)
end if
if (choice.eq.6) then
```

```
      call sub2(e,v,pho,N,mu,nev,phi,fer,ltf,ls,xo,xi)
      end if
      if (choice.eq.7) then
      goto 27
      end if
      close (12)
      goto 3
27    end
c     ~~~~~~~~~~~~~

      subroutine const(N,pho,nev)
c     ~~~~~~~~~~~~~~~~~~
      double precision v,N,pho,ans
      integer nev

      print *,'voltage considered /V'
      read *,v
      call sub1(v,N,pho,nev,ans)
      print *,'I = ',ans
      return
      end

c     ***** calculate tunneling current and  produce IV data file ****
      subroutine sub4(res,N,pho,nev)
c     ~~~~~~~~~~~~~~~~
      double precision v,vmi,vma,step,N,pho,ans
      integer res,nev
```

```
      open (3,file='current.d')
      print *,'voltage start (/V)'
      read *,vmi
      print *,'voltage stop (/V)'
      read *,vma
      print *,'voltage step (/V)'
      read *,step
      res=int((vma-vmi)/step)
      print *,(vma-vmi)/step,res
      do 10 i = 1, res + 1
      v=vmi + (i-1)*step
      call sub1(v,N,pho,nev,ans)
      write (3,200) v,ans
10    continue
200   format(e10.4,t15,e10.4)
      close (3)
      return
      end

      subroutine resis(res,N,pho,nev)
c     ~~~~~~~~~~~~~~~~~~~~~~~~~
      double precision v,vmi,vma,step,N,pho,ans,dummy,ant
      integer res,nev

      open (3,file='resist.d')
      print *,'voltage start (/V)'
      read *,vmi
```

```
      print *,'voltage stop (/V)'
      read *,vma
      print *,'voltage step (/V)'
      read *,step
      res=int((vma-vmi)/step)
      print *,(vma-vmi)/step,res
      do 10 i=1,res+1
      v=vmi+(i-1)*step
      call sub1(v,N,pho,nev,ans)
      dummy=v+1e-4
      call sub1(dummy,N,pho,nev,ant)
      write (3,100) v,(1e-4/(ans-ant))
10    continue
100   format(e10.4,t15,e10.4)
      close (3)
      return
      end

c     ******* Edit Parameters ********
      subroutine edit(pho,N,nev)
      double precision N,a,pho,mu,e,pi,q,m,ltf,ls,ep,d
      double precision EN,phi,fact,xo,xi,pfac,h,hcr
      integer nev
      common /block1/ pi,h,hcr,ep
      common /block2/ mu,m,e,a
      common /block3/ phi,EN,fact,ls,ltf,xo,xi,pfac
```

```
c       standard or inputed params
c       variables.
        print *,'required variables'
        print *,
        print *,'diameter [',d,' m]'
        read *,d
        print *
        print *
        print *,'Barrier height [',pho,' /eV]'
        read *, pho
        print *
        print *
        print *,'Doping level in m^3 [',N,' /m-3]'
        read *,N
        print *
        print *
        print *, 'Nr. of levels to be considered [',nev,']'
        read *,nev
        q = 2.0/3.0
        pho = pho
        a = pi*(d/2.0)**2
        mu = ((3.0*pi*pi*N)**q)/pfac
        ltf = dsqrt(2.0*ep*mu/(3.0*e*N))
        ls = (dsqrt(3.0d0)/2.0)*ltf
        return
        end
```

```
      subroutine sub2(e,v,pho,N,mu,nev,phi,fer,ltf,ls,xo,xi)
c     ~~~~~~~~~~~~~~~~~
      double precision e,v,pho,N,mu,phi,fer,ltf,ls,xo,xi
      integer nev

      print *, 'inputed variables'
      print *,'barrier ht.',pho,'[/eV]'
      print *,'doping level',N,'[/m3]'
      print *,'degeneracy',mu,'[/eV]'
      print *,'nr. of energy levels ',nev
c     print *,'bias',v,'[V]'
      print *,'biased barrier height',phi,'[/eV]'
c     print *,'fermi level',fer,'[/eV]'
      print *
      print *,'calculated variables'
      print *
      print *,'ltf',ltf,'[m]'
      print *,'ls',ls,'[m]'
      print *,'xo',xo,'[m]'
      print *,'xi',xi,'[m]'
      print *
      print *
      print *,'enter 0 to continue'
      read *,i
      return
      end
```

```
      subroutine sub1(v,N,pho,nev,ans)
c     ~~~~~~~~~~~~~~~~
      double precision s(1000),xy(1000),y(1000)
      double precision phi,N,v,EN,start,stop,mu
      integer nev,count,no
      integer ifail,nlimit

      double precision epsr,relerr,d01ahf,d01gaf,fer,fact
      double precision ans,pi,ls,ltf,xo,xi,step,pfac,pho
      double precision base,m,e,h,hcr,ep,a

      common /block1/ pi,h,hcr,ep
      common /block2/ mu,m,e,a
      common /block3/ phi,EN,fact,ls,ltf,xo,xi,pfac
      external fun
      external fun2
      open (4,file='tunn.d')
      open (8,file='source.d')
      open (9,file='res.d')
      phi=pho+mu-v
      fer=mu-v

c     required parameters.
c     ~~~~~~~~~~~~~~~~~~~~
      xo=2.0*ls*(dsqrt(phi/mu-0.4d0)-dsqrt(0.6d0))
      xi=xo-2.0*ltf*dlog(dsqrt(5.0d0)+dsqrt(6.0d0))
```

```
c       integration to find D(E) and S(E).
c       ~~~
```

```
      stop=xo
      ans=d01ahf(start,stop,epsr,no,relerr,fun,nlimit,ifail)
      start=dsqrt(6.0d0*mu/EN)
      stop=xi+2.0*ltf*abs(dlog(start+dsqrt(start**2-1.0d0)))
      start=xo
      ans=ans+d01ahf(start,stop,epsr,no,relerr,fun2,nlimit,ifail)
      else
c     evaluate integral, over first function only
c     ~~~~~~~~~~~~~~~~~~~~~~~~~~~~~~~~~~~~~~~~~~~~~~~~~~~~~~~~~~~
      start=0.0d0
      stop=xo-2.0*ls*(dsqrt(EN/mu-0.4d0)-dsqrt(0.6d0))
      ans=d01ahf(start,stop,epsr,no,relerr,fun,nlimit,ifail)
      end if

c     calculation of S(E)
      if (v.lt.0) then
      if (EN.lt.mu) then
      s(count)= 1
      else
      s(count)= (1+(EN-mu)/v)
      end if
      end if
      if (v.ge.0) then
      if (EN.lt.fer) then
      s(count) = 1
      else
      s(count) = 1-(EN-fer)/v
```

```
      end if
      end if
      fact = (e/hcr)**2
      fact = (v*m*fact)/(2.0*pi*pi*hcr)
      s(count) = s(count)*fact

c     printing of values into files
      y(count) = exp(-2.0*ans)*s(count)
      write (9,200) xy(count),y(count)
      write (8,200) xy(count),s(count)
      write (4,200) xy(count),exp(-2.0*ans)
10    continue
      call d01gaf(xy,y,nev,ans,relerr,ifail)
      ans=ans*e*a
      close(4)
      close(8)
      close(9)
      return
200   format(e10.4,t15,e10.4)
      end

      function fun(x)
c     ~~~~~~~~~~~~~~~~
      double precision pi,h,hcr,ep
      double precision mu,m,e,a
      double precision phi,EN,fact,ls,ltf,xo,xi,pfac
      double precision fun,x
```

```
      common /block1/ pi,h,hcr,ep
      common /block2/ mu,m,e,a
      common /block3/ phi,EN,fact,ls,ltf,xo,xi,pfac
      fun=dsqrt(abs(pfac*(EN-mu*(((xo-x)/(2.0*ls)+0.7746)**2+0.4))))
      return
      end

      Function fun2(x)
c     ~~~~~~~~~~~~~~~~~
      double precision fun2,x
      double precision pi,h,hcr,ep
      double precision mu,m,e,a
      double precision phi,EN,fact,ls,ltf,xo,xi,pfac
      common /block1/ pi,h,hcr,ep
      common /block2/ mu,m,e,a
      common /block3/ phi,EN,fact,ls,ltf,xo,xi,pfac
      fun2 = dsqrt(abs(pfac*(EN-6.0*mu/(cosh((x-xi)/(2.0*ltf)))**2)))
      return
      end

      subroutine sub6(res)
c     ~~~~~~~~~~~~~~~~~~~
      double precision v(500),c(500),vmi,r(500),p,out(500),norm
      integer res
      character *7 name
      print *,'output filename'
      read *,name
```

```
c       prog to evaluate resistance=(dV/dI)
c       ~~~~~~~~~~~~~~~~~~~~~~~~~~~~~~~~~~
        open (3,file='current.d')
        open (8,file=name)
        do 10 j=1,res
        read (3,200) v(j),c(j)
10      continue
        vmi = 100
c       /****** find Ro at V min ***********/
        do 20 j = 1,res-1
        p = ((c(j+1)-c(j))/(v(j+1)-v(j)))
        r(j) = 1/p
        if (v(j)**2.lt.vmi**2) then
        vmi = v(j)
        norm = r(j)
        end if
20      continue
        print *,'Vmin = ',vmi,'Ro = ',norm
        print *,'log[R(Vo)] = ',v(1),log(r(1))
c       print *,'experimental point '
c       read *,data
c       print *,'factor',10**(log(r(1))-data)
        print *,
        print *,'normal [0] or log [1] plot.'
        read *,j
        if (j.eq.1) then
        print *,'manual normalisation [1] or auto [0]'
```

```
      read *,j
      if (j.eq.1) then
      print *,'constant = '
      read  *,norm
      end if
      do 30  j = 1,res-1
      print *,log(r(j)/norm)
      out(j) = log(r(j)/norm)
      write (8,200) v(j),out(j)
30    continue
      else
      do 31 j = 1,res-1
      print *,r(j)
      out(j) = r(j)
      write (8,200) v(j),out(j)
31    continue
      end if
      close (3)
      close(8)
      return
200   format(e10.4,t15,e10.4)
      end
```

References

Adachi S., J. Appl. Phys. **58**, R1 (1985).

Alexander M.G.W., Nido M., Reimann K., Rühle W. W., Köhler K., Appl. Phys. Lett., **55** (24), 2517 (1989).

Ando T., Wakahara S., and Akera H., Phys. Rev. B **40**, 11 609 (1989); **40**, 11 619 (1989).

Andrews J. M. and Phillips J. C., Phys. Rev. Lett. **35**, 56 (1975).

Ashok S., Wang Y.G., Nakagawa O. S., Appl. Phys. Lett., **57**(15), 1560, (1990).

Austing D. G., Klipstein P. C., Roberts J. S., & Hill G., Semicond. Sci. Technol., **10** 616 (1995).

Austing D. G., Klipstein P. C., Roberts J. S., Button C. B. & Hill G., Phys. Rev. B, **48**(16), 11905 (1993).

Austing D. G., Klipstein P. C., Higgs A. W., Hutchinson H. J., Smith G. W., Roberts J. S., & Hill G, Phys. Rev. B, **47**(3), 1419 (1993).

Austing D. G., Kliplstein P. C., Roberts J. S., Hill J. S., Sol. St. Comm., **75** (9), 697, (1990).

Austing D.G., Klipstein P.C., Higgs A.W., Smith G.W., Roberts J.S., and Hill G., Proceedings of NATO workshop, El Escorial, May 1990 (unpublished).

Babb S. E.; Giardini & Lloyds Eds.,"High Pressure Measurement", Washington Butterworths (1962).

Bandyopadhyay A. K., Nalini A. V., Gopal S. R., Subramanyam S. V., Rev.Sci.Instrum., **51**(1), 136 (1980)

Barraclough K.G. in "Semiconductor Si" in "The Chemistry of the Semiconductor Industry", Moss S.J. & Ledwith A. eds., Blackie & Son Ltd., Glasgow & London (1987).

Batey J., Wright S. L., and DiMaria D. J., J. Appl. Phys., **57** (2), 484 (1985).

Beavitt A. R., Brit.J.Appl.Phys.(J.Phys.D), **2** (2), 1675 (1969).

Becker W. M., Hoo K., Winchell P. G., Rev.Sci.Instrum, **47** (5), 587 (1976).

Bending S. J., Ph.D. Thesis, Stanford University, California, 1985.

Beresford R, Luo L. F., Wang W. I., Mendez E. E., Appl. Phys. Lett., **55** (15), 1555 (1989).

Blakemore, "Semiconductor Statistics", Pergamon Press (1962).

Blakemore J.S. ed.,"Gallium Arsenide", American Institute of Physics Pub., (1987)

Bockenhoff E., Klitzing K. von, and Ploog K., Phys. Rev. B **38**, 10120 (1988).

Bonapasta A. A., Phys. Rev. B, **48**, 8771 (1993)

Bonnefoi A. R., McGill TC, Burnham R. D., and Anderson G. B., Appl. Phys. Lett. **50** (6), 344 (1987).

Bonnefoi A. R., Chow D. H., McGill T. C., J. Appl. Phys. **62** (9), 3836 (1987).

Bonnefoi A. R., McGill T. C., Burnham R. D., Phys. Rev. B, **37** (15), 8754 (1988).

Boren M. O., Babb S. E., Scott G. J., Rev.Sci.Instrum., **36**(10), (1965).

Boykin T. B., and Harris Jr. J. S., J. Appl. Phys., **72** (3), 988 (1992).

Bradley C. C., "High Pressure Methods in Solid State Research", Butterworths & Co.(Pub.) Ltd.,(1969)

Brennan K. F., Park D. H., Hess K., and Littlejohn M. A., J. Appl. Phys. **63**, 5004 (1988).

Bridgman, "Physics of High Pressure", G.Bells & Sons,(1958).

Brown E. R., Sollner T. C. L. G., Parker C. D., Goodhue W. D., and Chen C. L., Appl. Phys. Lett., **55**, 1777 (1989).

Bundy F. P., J. Appl. Phys. **32**, 483 (1961).

Capasso F., Mohammed K., and Cho A. Y., Appl. Phys. Lett., **48** (7), 478 (1986).

Capizzi M., Emiliani V., Frova A. & Sarto F., Phys. Rev. B, **47**(8), 4301 (1993).

Casey Jr. H. C. and Panish M. B., "Heterostructure Lasers", Academic Press, New York (1978).

Cassels J.M., "Basic Quantum Mechanics", 2nd Ed., Macmillan, London (1982).

Chambers S. A. and Sundaram S., J. Vac. Sci. Technol. B 9(4), 2256,(1991).

Chang L. L., Esaki L., and Tsu R., Appl. Phys. Lett., **24**(12), 593 (1974)

Chang S., Brillson L. J., Kime Y. J., Rioux D. F., Kirchner P. D., Pettit G. D., and Woodall, Phys. Rev. Lett. **64**, 2551 (1990).

Chen J., Chen J. G., Yang C. H., and Wilson R. A., J.Appl. Phys. **70**(6),

Chevallier J., Machayekhi B., Grattepain C. M., Rahbi R., Tehys B., Phys. Rev. B, **45**, 8803 (1992).

Cho H. Y., Min S. K., Chang K. J., Lee C., Phys, Rev. B **44**, 13779 (1991).

Cho H. Y., Kim E. K., Min S. K., Lee C., Phys. Rev. B **43**, 14498 (1991).

Cho J. & Nemanich R. J., Phys. Rev. B, **46**(23), 15212, (1992).

Chung Y, Chen C. Y., Langer D. W., & Park Y. S., J. Vac. Sci. Technol., **B1** 799 (1983).

Conibear A. B., Leitch A.W. R., & Ball C. A. B., Phys. Rev. B, **47**(4), 1846 (1993).

Costa J. C., Miller T. J., Williamson F., and Nathan M. I., J. Appl. Phys. **70** (4), 2173 (1991).

Cowley A. M. and Sze S. M., J. Appl. Phys., **36**(10), (1965).

Delagebeaudeuf D., Delescluse P., Etienne P., Massies J., Laviron M., Chaplart J., and Linh T., Electron. Lett., **18** (2), 85 (1982).

Dembovsky V., "Plasma Metallurgy, The Principles", Elsevier Science Pub. B. V., Amsterdam (1984).

Drickamer H. G. and Frank C. W., "Electronic transitions and the high pressure chemistry and physics of solids", Chapman & Hall, London , (1973).

Duke C. B., "Tunneling in Solids", Academic Press, New York (1969).

Duke C. B., in "Tunneling Phenomena in Solids', Burstein E. & Lundqvist eds., Plenum Press, New York (1969).

Eaves L., Toombs G. A., Sheard F. W., Payling C. A., Leadbeater M. L., Alves E. S., Foster T. J., Simmonds P. E., Henini M., Hughes O. H., Portal J. C., Hill G., & Pate M. A., Appl. Phys. Lett. **52** (3), 212 (1988).

Esaki L., Tsu R., IBM J. Res. Devel. **14**, 61 (1970).

Esaki L, "Electronic Properties of Multilayers & Low-Dimensional Semiconductor Structures", Chamberlain J. M. *et al* eds., Plenum Press, New York (1990).

Fiig T. and Jauho A. P., Appl. Phys. Lett. **59** (18), 2245 (1991).

Freeouf J. L. & Woodall J. M., Appl. Phys. Lett. **39**, 727 (1981).

Fujiwara H., Kadomatsu H., Tohma K., Rev. Sci. Instrum. **51**(10), Oct 1980.

Grant I.R. in "Semiconductor Si" in "The Chemistry of the Semiconductor Industry", Moss S.J. & Ledwith A. eds., Blackie & Son Ltd., Glasgow & London (1987).

Guéret P., Kaufmann U., Marclay E., Electron. Lett. Vol. 21, No. 8, (1985)

Harris C. I., PhD thesis, University of Bath (1991).

Hase I., Kawai H., Kaneko K., Watanabe N., J. Appl. Phys., **59** (11), 3792 (1986).

Heine V., Phys. Rev., **138**(6A), A1689, (1965).

Hickmott T. W., Phys. Rev. B **32**, 6531 (1985).

Homan C., MacCrone R. K., Whalley E., "High Pressure in Science & Technology, Part I- Collective Phenomena & Transport Properties", Elsevier Sci. Pub.Co.Inc.,(1984).

Jalil A., Heurtel A., Marfaing Y., and Chevallier J., J. Appl. Phys. **66**(12), 5854,(1989).

Jaros M., "Physics and Applications of Semiconductor and Microstructures", Clarendon Press, Oxford (1989).

Jayaraman A., Hutson A. R., McFee, Coriell, Maines; Rev. Sci. Instrum. **38**(1) 44 1967.

Kahen K. B., Phys. Rev. B, **43**(14), 11745 (1991).

Kane E.O. in "Basic Concept of Tunneling" in "Tunnelling Phenomena in Solids", Burstein E. & Lundqvist eds., Plenum Press, New York (1969)

Khoo G. S. and Ong C. K., Phys. Rev. B, **47**(24), 16369,(1993).

Kim E. K., Cho H. Y., Kim H. S., Min S. K., Kim T., Semicond. Sci. Technol., **7**, 695, (1992).

Kotel'nikov I. N., Chepikov D. K., Chirkova E. G., and Shul'man A. Y., Sov. Phys. Semicond., **21**(10), 1123 (1987).

Kotel'nikov I. N., Belnikhes I. L., and Shul'man A. Y., Sov. Phys. Semicond., **27**(2), 246 (1985).

Kyono C. S., Kesan V. P., Neikirk D. P., Maziar C. M., and Streetman B. G. , Appl. Phys. Lett., **54** (6), 549 (1989).

Landheer D., Liu H.C., Buchanan M., and Stoner R., Appl. Phys. Lett. **54** (18), 1784 (1989).

Leadbeater M. L., Alves E. S., Eaves L., Henini M., Hughes O. H., Sheard F. W., and Toombs G. A., Semicond. Sci. Technol., **3**, 1060 (1988).

Leadbeater M. L., Ph.D. Thesis, University of Nottingham, (1990).

Leadbeater M. L., Alves E. S., Eaves L., Henini M., Hughes O. H., Celeste A., Portal J. C., Hill G., and Pate M. A., Phys. Rev. B, **39** (5), 3438 (1989).

Lebens J. A., Silsbee R. H., Wright S. L., Appl. Phys. Lett. **51** (11), 840 (1987).

Lee H. H., Racicot R. J., and Lee S. H., Appl. Phys. Lett. **54**(8), 724, (1989).

Leitch A. W. R., Prescha T., Weber J., Phys. Rev. B, **44**(3), 1375, (1991).

Liboff R. L., "Introductory Quantum Mechanics", Holden-Day Inc. (1980).

Liliental-Weber Z, Weber E. R., Newman N., Spicer W. E., Gonsky R., & Washburn J., in "Defects in Semiconductors", Mater. Sci. Forum Vol. 10-12, edited by Bardeleben, Trans. Tech. Pub. Switzerland, (1986).

Liu J., Ortiz C. R., Zhang Y., Bakhru H., and Corbett J. W., Phys. Rev. B **44**(16), 8918, (1991).

Louie S. G. and Cohen M. L., Phys. Rev. B **13**, 2461 (1976).

Lu S. S., Nathan M. I. and Meng C. C., J.Appl.Phys. **69**(1), 525(1991).

Luryi S., Appl. Phys. Lett., **47** (5), 490,(1993).

Mead C. A. and Spitzer W. G., Phys. Rev. **134**, A713 (1964)

Mendez E. E., Calleja E.,and Wang W. I., Appl. Phys. Lett. **53** 977(1988).

Mendez E. E., Esaki L., and Wang W. I., Phys. Rev. B **33**, 2893 (1986)

Mendez E. E., Calleja E., and Wang W. I., Phys. Rev. B **34**, 6026 (1986)

Mendez E. E., Wang W. I., Calleja E., and Goncalves da Silva C. E. T., Appl. Phys. Lett. **50** 1263 (1987).

Mendez E. E., "Physics of Resonant Tunneling in Semiconductors" in "Physics and the Applications of Quantum Wells and Superlattices", E.E.Mendez and K. von Klitzing, Eds, Plenum, New York (1987).

Mendez E. E. and Chang L. L., Surf. Sci. **229**, 173 (1990).

Missous M., Rhoderick E. H., Woolf D., & Wilkes S. P., Semicond. Sci. Technol. 7, 218-221 (1992).

Mönch W. ed., "Electronic Structure of Metal-Semiconductor Contacts", Kluwer Academic Pub., Milan, (1990)

Nomura M., Yamamoto Y., Ochiai Y., Fujiwara H., Jap. Jour. of App. Phys. **20**(2) 363 (1981).

Noreldin O. and Scaife W.G., J.Phys.E:Sci. Instrum. **20** 1212 (1987).

Offsey S. D., Woodall J. M., Warren A. C., Kirchner P. D., and Chappell T. I., Appl. Phys. Lett., **48**(7), 475 (1986).

Othaman Z., Peck A. J., Bending S. J., Saunders G. A., Rossmanith M., and Klitzing K. von , J. Appl. Phys. **70** (3), 1548 (1991).

Othaman Z., Geim A. K., Bending S. J., Saunders G. A., Syme R. T., and Smith R. S., Semicon. Sci. Technol. **8** 1483 (1993).

Pacagnella A., Callegari A., Latta E., Gasser M., Appl. Phys. Lett. **55**(3), 259 (1989).

Padovani F. A. and Stratton R., Solid-St. Electron., **9**, 695 (1966).

Padovani F. A. and Stratton R., Solid-St. Electron., **10**, 813 (1967).

Pan N., Bose S. S., Kim M. H., Stillman G. E., Chambers F., Devane G., Ito C. R., & Feng M., Appl. Phys. Lett. **51**(8), 596 (1987).

Pankove J. I., Lampert M. G. , and Tang M. L., Appl. Phys. Lett. **32**, 439 (1978)

Pankove J. I., Zanzucchi P. J., Magee C. W., Lucovsky G., Appl. Phys. Lett. **46**(4), 421 (1985).

Pankove J. I. and Carlson D.E., Annu. Rev. Mater. Sci. **10** 43 (1980)

Pavesi L. & Giannozzi P., Phys. Rev. B, **43**, 2446 (1991).

Pearton S. J., Wu C. S., Stavola M., Ren F., Lopata J., Dautremont-Smith W. C., Vernon S. M., and Haven V. E., Appl. Phys. Lett. **51** (7), 496 (1987).

Pearton S. J., J. Appl. Phys., **53**(6), 4509 (1982).

Pearton S. J., Tavendale A. J., J. Appl. Phys., **54**(2), 1154 (1983).

Pearton S. J., Dautremont-Smith W. C., Lopata J., Tu C. W., Abernathy C. R., Phys. Rev. B, **36**(8), 4260 (1987).

Pearton S. J., Dautremont-Smith W. C., Chevallier J., Tu C. W., Cummings K. D., J. Appl. Phys., **59**(8), 2821 (1986).

Pearton S. J., Wu C. S., Stavola M., Ren F., Lopata J., Dautremont-Smith W. C., Vernon S. M., Haven V. E., Appl. Phys. Lett., **51**(7), 496 (1987).

Pearton S. J. and Tavendale T. J., J. Appl. Phys **54** (2) 1154 (1983)

Peggs G. N.,"High Pressure Measurement Techniques", Applied Science Pub.Ltd.(1983).

Ping J. G.& Ruda H. E., Phys. Rev. B, **47** 1412 (1993).

Price P. J., IEEE Transactions on Electron Devices, **36** (10), 2340 (1989).

Pritchard R., Klipstein P. C., Couch N. R., Kerr T. M., Roberts J. S., Mistry P., Soylu B., and Stobbs W. M., Semicond. Sci. Technol. **4** 754 (1989).

Pritchard R., Austing D. G., Klipstein P. C., Roberts J. S., Higgs A. W., and Smith G. W., J. Appl. Phys. **68** 205 (1990).

Pulsford N. J., Nicholas R. J., Dawson P., Moore K. J., Duggan G., Foxon C. T. B, Physical Review Letters, **63** (20), 2284 (1989).

Rhoderick E. H., "Metal-Semiconductor Contacts", Clarendon Press, Oxford (1978).

Rossmanith M., Leo J., and Klitzing K. von, J. Appl. Phys. **69**, 3641 (1991)

Rossmanith M., Syassen K., Böckenhoff E., Ploog K., Klitizing K. von, Appl. Phys. Lett, **63** (7), 937 (1993).

Rousseau K. V., Wang K. L., Schulman J. N., Appl. Phys. Lett., **54** (14), 1341 (1989).

Sakaki H., Noda T., Hirakawa K., Tanaka M., Matsusue T., Appl. Phys. Lett., **51** (23), 1934 (1987).

Samara G. A. & Giardini A. A., The Review of Sc. Inst. **35**(8), 989 (1964)

Schilfgaarde M, Weber E. R., & Newman N, Phys. Rev. Lett., **73** 581 (1994).

Shan W., Li M. F., Yu P. Y., Hanku W. L., & Walukiewiczw, Appl. Phys. Lett. **53** 974 (1988).

Sharda H., Prasad K., Faraone L., & Nassibian A., Semicond. Sci. Technol., **6**, 765 (1991).

Sharma B. L. (ed.), "Metal-Semiconductor Schottky Barrier Junctions and Their Applications", Plenum Press, (1984).

Shen T. H. & Matthai C. C., J. Phys.: Condens. Matter, **3**, 613 (1991).

Shen Y. T. & Myles C. W., Appl. Phys. Lett. **51**(24), 2034 (1987)

Sherman W. F. & Stadtmuller A. A., "Experimental Techniques in High-Pressure Research", John Wiley & Sons Ltd., (1987).

Skromme B. J., Sandroff C. J., Yablonovitch & Gmitter T., Appl. Phys. Lett. **51**(24), 2022 (1987).

Sollner T. C. L. G, Tannenwald P. E., Peck D. D., & Goodhue W. D., Appl. Phys. Lett. **45** (12), 1319 (1984).

Sollner T. C. L. G., Le H. Q., Correa C. A., & Goodhue W. D., Appl. Phys. Lett. **47**(1), 36 (1985).

Sollner T. C. L. G., Goodhue W. D., Tannerwald P. E., Parker C. D., & Peck D. D., App. Phys. Lett. **43** (6), 588 (1983).

Solomon P. M., Wright S. L., and Lanza C., Superlattices and Microstructures, **2**, 521 (1986).

Stratton R. in "Tunneling Phenomena in Solids', Burstein E. & Lundqvist eds., Plenum Press, New York (1969).

Stratton R. and Padovani F. A., Solid-St. Electron., **10**, 813 (1967).

Syme R. T., Kelly M. J., Smith R. S., Dale I., and Condie A., Electron. Lett. **27** 2192 (1991).

Tavendale A.J., Alexiev D., Williams A. A., Appl. Phys. Lett., **47**, 317, (1985).

Tejedor, Phys. Rev. B, **32** 6968 (1985)

Tejedor, Phys. Rev. Lett. **52** 465 (1984)

Thompson J. D., Rev. Sci. Instrum. **55**(2), 231 (1984).

Ting D. Z.Y., Jackson M. K., Chow D. H., Soderstrom J. R., Collins D. A., and McGill T. C.,

Toombs G.A. and Sheard F. W. in "Electronic Properties of Multilayers and Low Dimensional Semiconductor Structures", Chamberlain J. M. and Eaves L. and Portal J. C. (Eds.), Plenum Press, London (1989).

Tsu R. and Esaki L., Appl. Phys. Lett., **22** (11), 562 (1973).

Wang Chi-Yuen, Rev. Sci. Instrum., **38**(1), 24 (1967).

Wang W. I., Calleja E., and Mendez E. E., J.Vac.Sci. Technol. B, **5** 775 (1987).

Wang Y. G. and Ashok S., J. Appl. Phys. **65**(6), 2371 (1989).

Wang Z.M., Zhang Y. X., Wu K., Yuan M. H., Chen W. X., and Qin G. G., Phys. Rev. B **51** (12), 7878 (1995).

Wasilewski Z. and Stradling R. A., Semicond. Sci. Technol. **1**, 264 (1986).

Weiss J. D., Decker D. L. & Vanfleet H. B., J. Appl. Phys. **47**(9), 331 (1976).

Yuan M. H., Wang L. P., Jin S. X., Chen J. J., and Qin G. G., Appl. Phys. Lett., **58**(9), 925 (1991).